IPP-Report

Max-Planck-Institut für Plasmaphysik

Nikita Nikulsin

Models and methods for nonlinear magnetohydrodynamic simulations of stellarators

IPP 2021-20
Dezember 2021

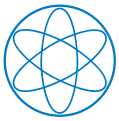

Technische Universität München

Max-Planck-Institut für Plasmaphysik

Models and methods for nonlinear magnetohydrodynamic simulations of stellarators

Nikita Nikulsin

Vollständiger Abdruck der von der Fakultät für Physik der Technischen Universität München zur Erlangung der akademischen Grades eines

Doktors der Naturwissenschaften

genehmigten Dissertation.

Vorsitzender:	Prof. Dr. Katharina Krischer
Prüfer der Dissertation:	
	1. Prof. Dr. Sibylle Günter
	2. Prof. Dr. Howard Wilson

Die Dissertation wurde am 30.09.2021 bei der Technischen Universität München eingereicht und durch die Fakultät für Physik am 29.11.2021 angenommen.

DEPARTMENT OF PHYSICS

TECHNISCHE UNIVERSITÄT MÜNCHEN

Models and methods for nonlinear magnetohydrodynamic simulations of stellarators

Author:	Nikita Nikulsin
Supervisor:	Prof. Dr. Sibylle Günter
Advisors:	Dr. Matthias Hoelzl
Submission Date:	30.09.2021

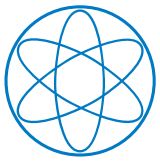

HELMHOLTZ
RESEARCH FOR GRAND CHALLENGES

EUROfusion

Abstract

Although the basic concept of a stellarator was known since the early days of fusion research, advances in computational technology have allowed to model increasingly complicated devices, leading up to the construction of Wendelstein 7-X, which has recently shown promising results. However, there has been surprisingly little activity in 3D magnetohydrodynamic (MHD) modelling of stellarators. The purpose of this work is to extend the JOREK nonlinear MHD code to stellarators. This requires first to generalize the reduced MHD model to be compatible with three-dimensional geometries. Such a model is derived and studied analytically in this dissertation. The model eliminates fast magnetosonic waves from the system, as a reduced MHD model should, and also guarantees that $\nabla \cdot \vec{B} = 0$, unlike several older reduced MHD models for stellarators. It is shown that the model conserves energy, but introduces an error into momentum conservation. An alternate model, which does not guarantee energy conservation, but has a smaller momentum conservation error is also derived. It is also shown that the main model introduces an error into equilibrium force balance, but the error is negligible. The energy and momentum conservation properties of the main and alternate models are then studied numerically in the tokamak limit. The momentum conservation error of the main model is shown to be small, and the energy conservation error of the alternate model is generally also small, unless one uses a less numerically stable version of the magnetic stream function evolution equation.

Once implemented, the main model was tested on a set of $l = 2$ stellarator equilibria, based on the classic Wendelstein 7-A stellarator, which used to be operated in Garching. The GVEC code was used to calculate the equilibria, which were then used as initial conditions for the JOREK runs. The simulations demonstrate that stable full MHD equilibria are preserved in the reduced model: the flux surfaces do not move throughout the simulation, and closely match the flux surfaces calculated in GVEC. Further, tearing modes were simulated, and the linear growth rates measured in JOREK are in good agreement with the growth rates calculated by the CASTOR3D linear MHD code. Future work includes optimization, a ballooning mode benchmark with CASTOR3D, a nonlinear benchmark with the MIPS code, and further analytical exploration of potential improvements to the reduced MHD model.

Zusammenfassung

Obwohl das Grundkonzept eines Stellarators seit den frühen Tagen der Fusionsforschung bekannt war, erlaubten Fortschritte in der Computertechnologie immer kompliziertere Geräte zu modellieren, was zum Bau von Wendelstein 7-X führte, der kürzlich vielversprechende Ergebnisse zeigen konnte. Es gab jedoch überraschend wenig Aktivität in der 3D magnetohydrodynamischen (MHD) Modellierung von Stellaratoren. Der Zweck dieser Arbeit besteht darin, den nichtlinearen MHD-Code JOREK auf Stellaratoren zu erweitern. Dies erfordert zunächst, dass das reduzierte MHD-Modell zu dreidimensionalen Geometrien kompatibel ist. Ein entsprechendes Modell wird in dieser Dissertation analytisch hergeleitet und untersucht. Das Modell eliminiert schnelle magneto-sonische Wellen aus dem System, wie es ein reduziertes MHD-Modell sollte, und garantiert im Gegensatz zu mehreren älteren MHD-Modellen für Stellaratoren, dass $\nabla \cdot \vec{B} = 0$. Es wird gezeigt, dass das Modell energieerhaltend, aber nicht exakt impulserhaltend ist. Ein alternatives Modell ist nicht exakt energieerhaltend, hat dafür aber einen kleineren Fehler in der Impulserhaltung. Es wird gezeigt, dass das Hauptmodell einen Fehler in der Gleichgewichtskraft-Balance einführt, der jedoch vernachlässigbar ist. Die Energie- und Impulseinhaltungseigenschaften der Haupt- und Alternativmodelle werden dann im Tokamak-Limit numerisch untersucht. Es wird gezeigt, dass der Impuls-Erhaltungsfehler des Hauptmodells klein ist und der Energieerhaltungssfehler des alternativen Modells im Allgemeinen ebenfalls, es sei denn, man verwendet eine numerisch weniger stabile Definition der Entwicklungsgleichung für den magnetischen Fluss.

Einmal umgesetzt, wurde das Hauptmodell auf einen Satz von $l = 2$ Stellarator-Gleichgewichten angewendet, basierend auf dem klassischen Wendelstein 7-A-Stellarator, der früher in Garching betrieben wurde. Der GVEC-Code wurde verwendet, um die Gleichgewichte zu berechnen, die dann als Anfangsbedingungen für die JOREK-Läufe dienen. Die Simulationen zeigen, dass ein stabiles volles MHD-Gleichgewicht im reduzierten Modell erhalten bleibt: Die Flussflächen verschieben sich in der Simulation nicht und stimmen mit den in GVEC berechneten Flussflächen überein. Ferner wurden Tearing-Moden simuliert und die mit JOREK berechneten linearen Wachstumsraten stimmen mit dem vollen-MHD-Codes CASTOR3D überein. Zukünftige Arbeit beinhaltet Optimierungen, einen Benchmark für Ballooning-Moden mit CASTOR3D, einen nichtlinearen Benchmark mit dem MIPS-Code und die weitere analytische Untersuchung potenzieller Verbesserungen des reduzierten MHD-Modells.

List of publications

Publications in peer-reviewed journals

- **Nikita Nikulsin**, Matthias Hoelzl, Alessandro Zocco, Karl Lackner, Sibylle Günter and the JOREK Team. Testing of the new JOREK stellarator-capable model in the tokamak limit. *Journal of Plasma Physics*, 87(3):855870301, 2021. doi:10.1017/S0022377821000477.
- **N. Nikulsin**, M. Hoelzl, A. Zocco, K. Lackner and S. Günter. A three-dimensional reduced MHD model consistent with full MHD. *Physics of Plasmas*, 26(10):102109, 2019. doi:10.1063/1.5122013.
- M. Hoelzl, G.T.A. Huijsmans, S.J.P. Pamela, M. Bécoulet, E. Nardon, F.J. Artola, B. Nkonga, C.V. Atanasiu, V. Bandaru, A. Bhole, D. Bonfiglio, A. Cathey, O. Czarny, A. Dvornova, T. Fehér, A. Fil, E. Franck, S. Futatani, M. Gruca, H. Guillard, J.W. Haverkort, I. Holod, D. Hu, S.K. Kim, S.Q. Korving, L. Kos, I. Krebs, L. Kripner, G. Latu, F. Liu, P. Merkel, D. Meshcheriakov, V. Mitterauer, S. Mochalskyy, J.A. Morales, R. Nies, **N. Nikulsin**, F. Orain, J. Pratt, R. Ramasamy, P. Ramet, C. Reux, K. Särkimäki, N. Schwarz, P. Singh Verma, S.F. Smith, C. Sommariva, E. Strumberger, D.C. van Vugt, M. Verbeek, E. Westerhof, F. Wieschollek and J. Zielinski. The JOREK non-linear extended MHD code and applications to large-scale instabilities and their control in magnetically confined fusion plasmas. *Nuclear Fusion*, 61(6):065001, 2021. doi:10.1088/1741-4326/abf99f.

Contributions at conferences, seminars, and workshops

- Talk: N. Nikulsin, R. Ramasamy, M. Hoelzl, A. Zocco, K. Lackner and S. Guenter. First results for stellarator simulations with JOREK. DPG Meeting of the Matter and Cosmos Section, Virtual (9/2021).
- Talk: N. Nikulsin, M. Hoelzl, R. Ramasamy, A. Zocco, K. Lackner and S. Günter. Implementation and testing of stellarator-capable models in JOREK. 4th Asia-Pacific Conference on Plasma Physics (AAPPS-DPP), Remote e-conference (10/2020).
- Talk: N. Nikulsin, M. Hoelzl, A. Zocco, S. Günter and K. Lackner. A three-dimensional reduced MHD model consistent with full MHD. 18th European Fusion Theory Conference (EFTC), Ghent, Belgium (10/2019).
- Poster: N. Nikulsin and M. Hoelzl, Towards nonlinear MHD simulations of quasi-axisymmetric stellarators. DPG Spring Meeting, Munich, Germany (3/2019).

Acknowledgements

To begin with, I would like to thank my direct supervisor, Matthias Hölzl, for all of his help and advice with my doctoral project, from suggesting the research topic to helping translate the abstract of this dissertation to German. He was always readily available for consultation on short notice when I encountered difficulties in my work. I would also like to thank my academic supervisor, Sibylle Günter, for guiding me along this project and for finding the time to have regular meetings with me despite her busy schedule as the scientific director of IPP. Finally, and not in the least, I would like to thank Karl Lackner and Alessandro Zocco for co-supervising my doctoral project and sharing their valuable insight acquired from many years of research experience.

I would like to also thank Rohan Ramasamy, another doctoral student working on modelling stellarators with JOREK, for collaborating with me, most importantly, for extending the JOREK grids to allow for non-axisymmetry and for running CASTOR3D when I needed it. His suggestions, given during regular meetings where we discussed each others doctoral projects, are also very much appreciated. I also thank Florian Hindenlang, the author of the GVEC code, for all his help with calculating the equilibria and also for valuable advice extending far beyond questions related to GVEC. I would also like to thank Erika Strumberger, the author of the CASTOR3D code, for her help and advice, and for always being willing to discuss any questions that I had, whether related to CASTOR3D or not. I would also like to thank several other members of the JOREK group at IPP, namely Vinodh Bandaru, Zhixin Lu, Andres Cathey, Fabian Wieschollek, Verena Mitterauer and Nina Schwarz, who have all, at various points, helped me with both technical and non-technical questions. Within the broader JOREK community, I would like to thank Guido Huijsmans and Boniface Nkonga for the interesting and friutful discussions that I had with them. I would also like to thank Michael Drevlak for giving me access to his EXTENDER_P code, showing me how to use it and patiently answering my questions. I also thank Brendan Shanahan and Paul Huslage for sharing their Python implementation of Dommaschk potentials with me. Finally, I would like to thank Farah Atour for getting me involved in a side project not related to this dissertation, which I very much enjoyed, and Xin Wang for supervising that project. On a note unrelated to research, I would like to thank Gergely Papp, Philipp Lauber and Peter Manz for allowing me to get involved as a tutor in the courses that they taught, so that I could satisfy the university's teaching requirement for doctoral students.

Contents

1 Introduction

The stellarator, having been proposed by Lyman Spitzer in 1951, is one of the oldest plasma confinement concepts potentially applicable as a fusion power plant. However, early stellarators were plagued with problems stemming from neoclassical transport losses, leading to them being largely phased out in favor of tokamaks by the 1970s [1–3]. However, improved mathematical models and increased computational power, which became available by the late 1980s, allowed to overcome the main challenges faced by the stellarator concept. Moreover, the revival of stellarators brought with it a new strategy for fusion research, where numerical modelling drives the development of future machines, as opposed to the traditional strategy, where smaller scale machines had to be built and experimented on before advancing to larger scale machines. The creation of Wendelstein 7-X is one example of the successful application of this new strategy. The advantages are clear: not only is it more cost effective, but it also allows to consider a much wider range of potential machine designs in a much shorter amount of time [1].

However, most of the computational devlopments mentioned above focussed on the optimization of stellarator equilibria. Until recently, there has been almost no work done on nonlinear magnetohydrodynamic (MHD) simulations of stellarators. Thus, the goal of this dissertation is to extend JOREK, one of the leading nonlinear MHD codes for tokamaks [4–6], to stellarators. The work consists of two parts: first, a reduced MHD model compatible with three-dimensional geometries is derived by generalizing the ideas of Breslau et al, Izzo et al and Strauss [7–9], then this model is implemented in the JOREK code and tested on a simple stellarator. The rest of this dissertation is organized as follows. The rest of this chapter introduces the concepts that will be used later on. In chapter 2, the main model that will be

used for stellarators is derived; in the tokamak limit, this model reduces to the tokamak reduced MHD model normally used by JOREK. In addition, an alternate model with somewhat better momentum conservation properties, but worse energy conservation properties will be derived in chapter 2. In chapter 3, the alternate model is be tested in the tokamak limit; the momentum conservation properties of the main model are also be tested. Finally, in chapter 4, the main model is validated using a set of simple stellarator equilibria based on Wendelstein 7-A.

1.1 Ideal and viscoresistive magnetohydrodynamics

The equations of ideal MHD are as follows:

$$\begin{aligned}
\frac{\partial \rho}{\partial t} + \nabla \cdot (\rho \vec{v}) &= 0, \\
\frac{\partial}{\partial t}(\rho \vec{v}) + \nabla \cdot (\rho \vec{v} \vec{v}) &= \vec{j} \times \vec{B} - \nabla p, \\
\frac{\partial p}{\partial t} + \vec{v} \cdot \nabla p + \gamma p \nabla \cdot \vec{v} &= 0, \\
\frac{\partial \vec{B}}{\partial t} &= -\nabla \times \vec{E}, \\
\nabla \times \vec{B} = \mu_0 \vec{j}, \quad \nabla \cdot \vec{B} = 0, \quad \vec{E} &= -\vec{v} \times \vec{B}.
\end{aligned} \tag{1.1}$$

In the above equations, the usual notation is followed, with ρ, p, $\vec{v}$, $\vec{E}$, $\vec{B}$ and $\vec{j}$ being density, pressure, velocity, electric field, magnetic field and current, respectively, and the constant $\gamma = 5/3$ being the ratio of specific heats. It is also assumed that the ideal gas law $p = \rho RT$ holds. Note that, using the continuity equation, the momentum equation can be rewritten in a simpler form:

$$\rho \frac{\partial \vec{v}}{\partial t} + \rho(\vec{v} \cdot \nabla)\vec{v} = \vec{j} \times \vec{B} - \nabla p.$$

The MHD equations can be derived from the Boltzmann-Maxwell system of equations by taking moments of the Boltzmann equation: the continuity equation corresponds to the zeroth moment, the momentum equation to the first moment and the pressure equation to the second moment. This derivation procedure is presented in chapter 2 of Ref [3].

When applying ideal MHD to plasmas, it is assumed that the plasma is a superconducting inviscid fluid that forms a closed system (i.e. there are no sources or sinks in the equations). Despite its relative simplicity, ideal MHD has seen much success in describing basic plasma behavior, sometimes even outside its formal range of validity (see chapters 9 and 10 in Ref [3] for a more detailed discussion on the applicability of ideal MHD). Nevertheless, fusion plasmas exhibit many phenomena that are not captured by ideal MHD; these phenomena become important on time scales longer than the ideal time scale, and so, for example, an equilibrium that is stable in the context of ideal MHD may actually be unstable to resistive tearing modes in reality. Viscoresistive MHD, which is employed by most modern fluid codes, attempts to extend the scope of MHD beyond ideal effects, while maintaining the framework of a fluid model. All of the work presented in this dissertation was done in the context of single-fluid viscoresistive MHD.

Viscoresistive MHD can be obtained by starting with resistive MHD. The resistive MHD model can be derived from the Boltzmann-Maxwell system similarly to ideal MHD, but without neglecting the terms that end up producing the resistive term in Ohm's Law [10]. Then, the divergence of the viscous stress tensor, which was neglected in the derivation, is, in the case considered here, approximated by a viscosity coefficient multiplied by the Laplacian of velocity, just like in the Navier-Stokes equation of standard fluid dynamics. While this is a very rough approximation, it does not detract significantly from the general applicability of the model [4, 11, 12], and such a viscosity term can sometimes help prevent numerical instabilities in simulations [13]. In addition to viscosity, the viscoresistive model used by the JOREK code also includes anisotropic mass and heat diffusion, as well as mass and heat sources. The mass and heat diffusion coefficients perpendicular to field lines are meant to approximate the effect of microinstabilities.

The full set of viscoresistive MHD equations is as follows:

$$\begin{gathered}
\frac{\partial \rho}{\partial t} + \nabla \cdot (\rho \vec{v}) = P, \\
\frac{\partial}{\partial t}(\rho \vec{v}) + \nabla \cdot (\rho \vec{v} \vec{v}) = \vec{j} \times \vec{B} - \nabla p + \mu \Delta \vec{v}, \\
\frac{\partial p}{\partial t} + \vec{v} \cdot \nabla p + \gamma p \nabla \cdot \vec{v} = (\gamma - 1) \left[\nabla \cdot \left(\kappa_\perp \nabla_\perp T + \kappa_\parallel \nabla_\parallel T + \frac{p}{\gamma - 1} \frac{D_\perp}{\rho} \nabla_\perp \rho \right) + S_e + \eta j^2 \right], \\
\frac{\partial \vec{B}}{\partial t} = -\nabla \times \vec{E}, \\
\nabla \times \vec{B} = \mu_0 \vec{j}, \quad \nabla \cdot \vec{B} = 0, \quad \vec{E} = -\vec{v} \times \vec{B} + \eta \vec{j}, \quad P = \nabla \cdot (D_\perp \nabla_\perp \rho) + S_\rho.
\end{gathered} \tag{1.2}$$

Here, η is the resistivity, μ is the dynamic viscosity, $D_\perp$ is the mass diffusion coefficient across field lines, $\kappa_\perp$ and $\kappa_\parallel$ are the heat conduction coefficients across and along field lines, respectively, and S_ρ and S_e are the mass and energy sources, respectively. The gradient operators parallel and perpendicular to the magnetic field $\vec{B}$ are defined as follows: $\nabla_\parallel = \frac{\vec{B}}{B^2} \vec{B} \cdot \nabla$ and $\nabla_\perp = \nabla - \nabla_\parallel$. The $D_\perp$ term in the pressure equation represents the internal energy carried by mass diffusing across field lines. Finally, both the ideal and viscoresistive models introduced in this section will be referred to as full MHD, in contrast to reduced MHD, which will be introduced in section 1.3.

1.2 Linearized MHD

The ideal MHD model (1.1) is sufficient to describe the three main types of MHD waves and many of the fastest-growing instabilities. In this section, the basics of MHD waves and instabilities will be summarized, mostly following section 8.3 of Ref [3].

To begin with, the equations (1.1) must be linearized. Suppose that some equilibrium, i.e. a solution of the equations (1.1) that does not depend on time, is known:

$$\vec{B}(\vec{r}, t) = \vec{B}_0(\vec{r}), \qquad p(\vec{r}, t) = p_0(\vec{r}), \qquad \rho(\vec{r}, t) = \rho_0(\vec{r}), \qquad \vec{v}(\vec{r}, t) = \vec{v}_0(\vec{r}). \tag{1.3}$$

One then looks for an approximate time-dependent solution to the equations (1.1) in the form

$$Q(\vec{r},t) = Q_0(\vec{r}) + Q_1(\vec{r},t),$$

where $Q \in \{\vec{B}, p, \rho, \vec{v}\}$ and $|Q_1/Q_0| \ll 1$. Since Q_1 is a small first order perturbation to Q_0, the equations can be expanded around Q_0, dropping all higher order terms, i.e. terms that contain more than one Q_1 factor. Since the Q_0's are known functions, what remains then is a set of linear equations with Q_1 as the unknowns:

$$\begin{aligned}
\frac{\partial \rho}{\partial t} + \nabla\cdot(\rho_0\vec{v}) + \nabla\cdot(\rho\vec{v}_0) &= 0,\\
\rho_0\frac{\partial \vec{v}}{\partial t} + \rho_0(\vec{v}_0\cdot\nabla)\vec{v} + \rho_0(\vec{v}\cdot\nabla)\vec{v}_0 + \rho(\vec{v}_0\cdot\nabla)\vec{v}_0 &= \vec{j}_0\times\vec{B} + \vec{j}\times\vec{B}_0 - \nabla p,\\
\frac{\partial p}{\partial t} + \vec{v}_0\cdot\nabla p + \vec{v}\cdot\nabla p_0 + \gamma p_0\nabla\cdot\vec{v} + \gamma p\nabla\cdot\vec{v}_0 &= 0,\\
\frac{\partial \vec{B}}{\partial t} &= \nabla\times(\vec{v}_0\times\vec{B} + \vec{v}\times\vec{B}_0),
\end{aligned} \tag{1.4}$$

where the "1" subscripts have been dropped, and the fact that the equilibrium satisfies the ideal MHD equations was used to remove zeroth order terms, i.e. terms that only contain Q_0 factors.

1.2.1 MHD waves

Consider a simple equilibrium in the ideal case $\eta = 0$:

$$\vec{B}_0 = B_0\widehat{z}, \qquad p_0 = \text{const}, \qquad \rho_0 = \text{const}, \qquad \vec{v}_0 = 0, \tag{1.5}$$

where $B_0 = \text{const}$. Thus, the plasma fills all space with a uniform density and pressure, permeated by a homogeneous magnetic field. It is easy to see that the equilibrium (1.5) satisfies the ideal MHD equations (1.1). Since the equilibrium is also independent of spatial position, one can look for a plane wave solution to the equations (1.4) in this particular case:

$$Q(\vec{r},t) = \widetilde{Q}e^{i(\vec{k}\cdot\vec{r}-\omega t)}.$$

Since only the z axis has been fixed so far, one can use this freedom to choose the x and y axes so that $\vec{k}$ lies in the $y-z$ plane: $\vec{k} = k_\perp\widehat{y} + k_\parallel\widehat{z}$. The equations (1.4)

then become:

$$\begin{aligned} \omega\widetilde{\rho} &= \rho_0 \vec{k} \cdot \widetilde{\vec{v}}, \\ \rho_0 \omega \widetilde{\vec{v}} &= i\widetilde{\vec{j}} \times \vec{B}_0 + \vec{k}\widetilde{p}, \\ \omega\widetilde{p} &= \gamma p_0 \vec{k} \cdot \widetilde{\vec{v}}, \\ \omega\widetilde{\vec{B}} &= -\vec{k} \times (\widetilde{\vec{v}} \times \vec{B}_0), \end{aligned} \tag{1.6}$$

where $\widetilde{\vec{j}} = i\vec{k} \times \widetilde{\vec{B}}/\mu_0$. Since all of the amplitudes can be expressed in terms of the velocity amplitude, substituting them into the momentum equation results in a vector equation for just the velocity amplitude, the three components of which are shown below:

$$\begin{aligned} (\omega^2 - k_\parallel^2 c_A^2)\widetilde{v}_x &= 0, \\ (\omega^2 - k_\perp^2 c_s^2 - k^2 c_A^2)\widetilde{v}_y - k_\perp k_\parallel c_s^2 \widetilde{v}_z &= 0, \\ -k_\perp k_\parallel c_s^2 \widetilde{v}_y + (\omega^2 - k_\parallel^2 c_s^2)\widetilde{v}_z &= 0, \end{aligned} \tag{1.7}$$

where $c_A = B_0/\sqrt{\mu_0 \rho_0}$ is the Alfvénic velocity and $c_s = \sqrt{\gamma p_0/\rho_0}$ is the speed of sound. This is a system of linear algebraic equations of the form $\overleftrightarrow{M} \cdot \widetilde{\vec{v}} = 0$. In order for the system to have a solution, the determinant of the coefficient matrix $\overleftrightarrow{M}$ must be zero. Note that there will be infinitely many solutions, initial conditions are required in order to be able to choose one particular solution. Setting the determinant to zero results in the dispersion relation, which gives the frequency ω in terms of the wave vector $\vec{k}$. The dispersion relation has three solutions:

$$\omega^2 = k_\parallel^2 c_A^2, \qquad \omega^2 = \frac{k^2(c_A^2 + c_s^2)}{2}\left(1 \pm \sqrt{1 - \frac{4k_\parallel^2 c_A^2 c_s^2}{k^2(c_A^2 + c_s^2)^2}}\right). \tag{1.8}$$

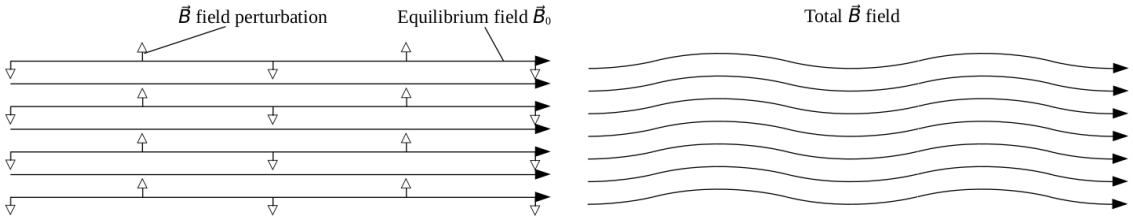

Figure 1.1: The equilibrium and perturbation magnetic fields in an Alfvén wave.

Each of the three solutions of the dispersion relation corresponds to an MHD

wave. The first solution, $\omega^2 = k_\parallel^2 c_A^2$, corresponds to an Alfvén wave. The wave is independent of $k_\perp$ and so it travels along field lines. Note that, for a pure Alfvén wave solution, equation (1.7) requires that $\widetilde{v}_y = \widetilde{v}_z = 0$; further, equations (1.6) give $\widetilde{B}_y = \widetilde{B}_z = \widetilde{\rho} = \widetilde{p} = 0$ and $\nabla \cdot \vec{v} = \vec{k} \cdot \widetilde{\vec{v}} = 0$. Therefore, in a uniform equilibrium, the wave compresses neither the fluid nor the magnetic field, but simply bends the magnetic field lines. However, when the background magnetic field $\vec{B}_0$ is not homogeneous, the Alfvén wave can result in compressional motion [14].

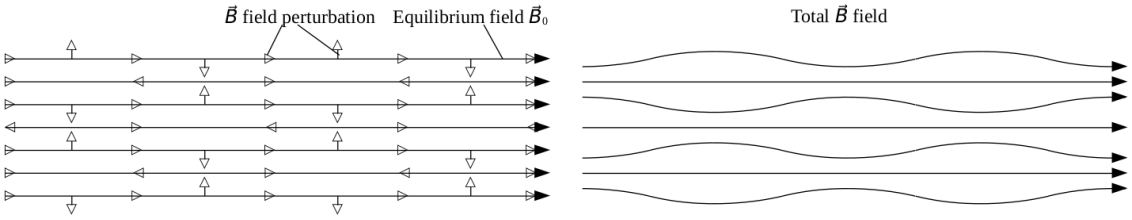

Figure 1.2: The equilibrium and perturbation magnetic fields in a fast magnetosonic wave at low β.

Now consider the solution to the dispersion relation corresponding to the second expression in (1.8) taken with the "+" sign. This solution corresponds to the fast magnetosonic wave, referred to as such because its phase velocity, $c_f = \omega/k$ is always greater than the Alfvénic velocity c_A. Note that, in general for a pure fast magnetosonic wave solution, $\widetilde{v}_x = 0$, while $\widetilde{v}_y \neq 0$ and $\widetilde{v}_z \neq 0$. Similarly, equations (1.6) give $\widetilde{B}_x = 0$, while $\widetilde{B}_y \neq 0$ and $\widetilde{B}_z \neq 0$. Therefore, since both $\nabla \cdot \vec{v} \neq 0$ and $B_z \neq 0$, the wave compresses both the fluid and magnetic field. In addition, when $\beta \ll 1$, $c_s^2 \ll c_A^2$ and so the fast magnetosonic wave solution reduces to $\omega^2 \approx k^2 c_A^2$; in this regime the fast magnetosonic wave is often referred to as the compressional Alfvén wave. It is also the only wave among the three MHD waves that can propagate orthogonally to field lines in the low β regime. Also note that $\widetilde{v}_z \ll \widetilde{v}_y$, which follows from the last equation in (1.7), assuming that $k_\parallel \sim k_\perp$. Then, from the equations (1.6), one gets that $\mu_0 \widetilde{p}/(B_0 \widetilde{B}) \sim \beta$, which means that most of the the wave's energy is carried by magnetic field compression, as opposed to fluid compression.

Finally, consider the dispersion relation solution given by the second expression

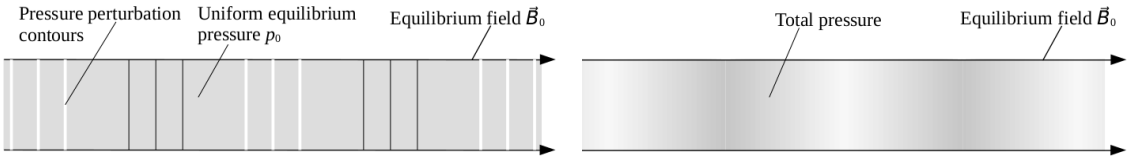

Figure 1.3: The equilibrium and perturbation magnetic fields in a slow magnetosonic wave at low β.

in (1.8) taken with the "$-$" sign. This is the slow magnetosonic wave, for which the phase velocity is always less than the Alfvénic velocity. In the low β regime, one can see that the dispersion relation solution approximates as $\omega^2 \approx k_\parallel^2 c_s^2$, and so the slow magnetosonic wave becomes a sound wave which is confined to propagate only along magnetic field lines. In this limit, since the wave propagates only along magnetic field lines, $k_\perp$ can be set to zero, then from (1.6) it follows that $\widetilde{B}_z = 0$, so the magnetic field is not compressed.

1.2.2 Instabilities

Now consider the more general case of an arbitrary *static* MHD equilibrium, i.e. an equilibrium where $\vec{v}_0 = 0$. In this case, the linearized equations (1.4) become

$$\begin{aligned} \frac{\partial \rho}{\partial t} + \nabla \cdot (\rho_0 \vec{v}) &= 0, \\ \rho_0 \frac{\partial \vec{v}}{\partial t} &= \vec{j}_0 \times \vec{B} + \vec{j} \times \vec{B}_0 - \nabla p, \\ \frac{\partial p}{\partial t} + \vec{v} \cdot \nabla p_0 + \gamma p_0 \nabla \cdot \vec{v} &= 0, \\ \frac{\partial \vec{B}}{\partial t} &= \nabla \times (\vec{v} \times \vec{B}_0). \end{aligned} \tag{1.9}$$

Note that the ideal MHD linearized equations can rewritten as one vector equation for velocity. Indeed, after differentiating the momentum equation with respect to time, one can substitute the other three equations into it, resulting in

$$\rho_0 \frac{\partial^2 \vec{v}}{\partial t^2} = \vec{j}_0 \times [\nabla \times (\vec{v} \times \vec{B}_0)] + \frac{1}{\mu_0} [\nabla \times [\nabla \times (\vec{v} \times \vec{B}_0)]] \times \vec{B}_0 + \nabla (\vec{v} \cdot \nabla p_0 + \gamma p_0 \nabla \cdot \vec{v}). \tag{1.10}$$

This is an important simplification, which paves the way to the energy principle approach, which will not be discussed here (see chapter 8 of Ref [3] for more details). However, this simplification is available only in ideal MHD. For example, had the

resistive term $\eta\vec{j}$ been present under the curl on the RHS of Faraday's law in (1.9), the simplification would obviously not be possible.

Since the coefficients of the equations (1.9) are independent of time, one can look for a solution of the form

$$Q(\vec{r},t) = \widetilde{Q}(\vec{r})e^{-i\omega t}.$$

Such solutions are referred to as normal modes. The equations (1.9) then become an eigenvalue problem:

$$\begin{aligned} i\omega\widetilde{\rho} &= \nabla\cdot(\rho_0\widetilde{\vec{v}}),\\ i\omega\widetilde{\vec{v}} &= -\frac{\vec{j}_0\times\widetilde{\vec{B}}}{\rho_0} - \frac{\widetilde{\vec{j}}\times\vec{B}_0}{\rho_0} + \frac{\nabla\widetilde{p}}{\rho_0},\\ i\omega\widetilde{p} &= \widetilde{\vec{v}}\cdot\nabla p_0 + \gamma p_0\nabla\cdot\widetilde{\vec{v}},\\ i\omega\widetilde{\vec{B}} &= -\nabla\times(\widetilde{\vec{v}}\times\vec{B}_0). \end{aligned} \tag{1.11}$$

For each normal mode solution, the associated eigenvalue determines the oscillation frequency and growth or decay rate of the mode. If, for a particular equilibrium, there exists an eigenvalue with $\mathrm{Im}\,\omega > 0$, then the associated normal mode will grow exponentially and the equilibrium is said to be unstable. Conversely, if all of the eigenvalues of an equilibrium satisfy $\mathrm{Im}\,\omega \leq 0$, the equilibrium is said to be stable.

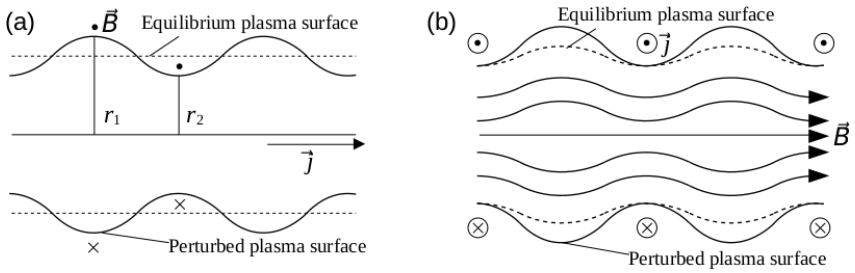

Figure 1.4: An interchange mode in a Z-pinch (a), and a ballooning mode in a linked mirror machine (b).

Two particular instabilities, namely tearing modes and ballooning modes, deserve special mention, as they will appear in the simulations presented in the following chapters. The ballooning mode is a pressure-driven instability that can be described

with ideal MHD, however the presence of a resistive term can affect its behavior. The ideal ballooning mode can be illustrated using the example from section 12.3 of Ref [15]. First, consider an interchange mode in a Z-pinch, which is a linear device where plasma is confined in a column by a current flowing along the length of the column. At a distance r away from the axis, the magnetic field will scale as $B \sim 1/r$, and so the magnetic tension force scales as $F = (B^2/\mu_0)(2\pi r L) \sim 1/r$. If the surface is perturbed, as shown in Figure 1.4 a, the magnetic tension will be the greatest at position 2 and the least at position 1, since $r_1 > r_2$. Due to this disparity, the magnetic field pushes the plasma harder in the more narrow region than in the wider region, and so the net force from both the magnetic field and pressure is radially inward in the narrow region and radially outward in the wider region. The plasma moves from the narrow region into the wider region, increasing the force disparity and causing the instability to grow exponentially. In general, whenever the field line curvature vector $\vec{\kappa} = (\vec{b} \cdot \nabla)\vec{b}$, where $\vec{b} = \vec{B}/B$, points in the same direction as the pressure force $-\nabla p$, the magentic field will have a destabilizing influence, whereas if $\vec{\kappa}$ points in the opposite direction to $-\nabla p$, the magnetic field will counteract the instability. Regions where the magnetic field has a stabilizing effect are said to have favorable curvature, whereas those where the magnetic field is destabilizing are said to have unfavorable curvature. Both kinds of curvature can be seen in a linked mirror machine, where instead of an axial current, the plasma is confined by several current-carrying loops around it, as shown in Figure 1.4 b. In such a configuration, the curvature is favorable near the loops, but unfavorable away from them. A ballooning mode is thus a perturbation which grows in regions of unfavorable curvature, but is suppressed where the curvature is favorable. Ballooning modes are referred to as such because the tend to "balloon out" in regions of unfavorable curvature [15]. A more rigorous discussion of ballooning modes in more complicated configurations can be found in chapter 12 of Ref [3].

Unlike ballooning modes which can be described with ideal MHD, a tearing mode

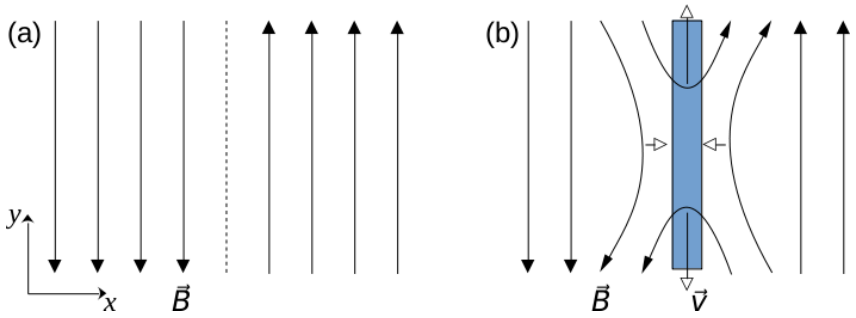

Figure 1.5: An equilibrium with a magnetic field reversal (a), and a tearing mode that arises in such an equilibrium (b). The blue rectangle indicates the layer where resistive effects are important.

requires resistivity to be taken into account. As will be shown in the next chapter, ideal MHD conserves magnetic flux through any arbitrary surface that is advected with the fluid flow, and so the field lines must move with the plasma. Since fluid elements cannot break into smaller elements, the magnetic field lines also cannot break or reconnect in ideal MHD. However, tearing modes require just that: the breaking and reconnecting of magnetic field lines. Consider a two-dimensional equilibrium, where the magnetic field reverses direction at $x = 0$ (Figure 1.5 a). A tearing mode arises when the field lines break and reconnect, as shown in Figure 1.5 b, but that can only happen where the field reverses direction. Thus, the resistivity will only be important in a thin layer around $x = 0$; outside of that layer the plasma can still be described by ideal MHD [16]. In toroidal plasma configurations, such as tokamaks and stellarators, a similar situation occurs on rational flux surfaces [17], which are flux surfaces where a field line returns to the same point on the surface after a finite number of toroidal turns, forming a helix. Suppose that, after returning to the same point, the field line has completed n toroidal turns and m poloidal turns, which corresponds to a safety factor $q = n/m$. Following Ref [17], introduce a coordinate on the flux surface in an orthogonal direction to the field line:

$$\xi = \theta - \frac{m}{n}\phi$$

where ϕ and θ are the toroidal and poloidal angles, respectively. Then, the ξ

component of the magnetic field will reverse direction at the rational flux surface:

$$B_\xi = B_\theta \left(1 - \frac{m}{n} q(r)\right),$$

where r is the radial coordinate. This leads to a tearing mode arising at the rational flux surface. A more rigorous treatment of the tearing mode in the two-dimensional case is given in Ref [16], whereas Ref [17] considers tearing modes in toroidal geometry.

1.3 Reduced MHD

One technique that allows to use a larger time step with a reasonable spatial resolution is the elimination of fast magnetosonic waves from the plasma by using a reduced MHD model, which nevertheless can retain the relevant physics which one intends to study [9, 18]. As fast magnetosonic waves are the fastest of the three types of MHD waves, their removal eliminates the shortest time scale, thus relaxing the constraint imposed by the CFL condition and allowing the use of larger time steps.

Implicit time integration methods are another method by which the CFL condition can be relaxed. Instead of removing the shortest time scale from the system, implicit methods simply avoid the CFL condition altogether. However, even with implicit methods, using time steps that are much larger than the shortest time scale can lead to poor accuracy [18, 19]. Thus, using reduced MHD in combination with implicit methods confers the most advantages. Finally, reduced MHD has less unknowns than full MHD, which can reduce the memory required for a typical simulation.

Many different versions of reduced MHD have been derived over the years, however all those versions can be grouped into two main categories: ordering-based reduced MHD and ansatz-based reduced MHD. These two categories will be introduced in the following subsections. Using an ansatz tends to involve less assumptions, while keeping more physics. For example, Park *et al* show that internal kink

modes in a cylindrical geometry can be studied with ansatz-based models, but not ordering-based models, as only keeping the lowest order in the inverse aspect ratio does not cpature these modes [20]. However, the various equations of ansatz-based models tend to be harder to interpret, owing to their complexity. In addition, error estimation is more difficult in ansatz-based models due to the lack of an ordering parameter.

1.3.1 Ordering-based reduced MHD

The first reduced MHD models to be derived historically were ordering-based. Greene and Johnson first used these models to study MHD equilibria for stellarators in the 1960s [21]; later Kadomtsev, Pogutse and Strauss [22, 23] developed dynamic reduced MHD models, which they used to study instabilities in tokamaks. To introduce the main ideas behind ordering-based reduced MHD, Strauss's model derived in Ref [23] will be summarized here.

Strauss begins his derivation from ideal MHD (1.1). The derivation relies on an expansion in the inverse aspect ratio ϵ, which is the ratio of the minor radius to the major radius of the tokamak. An ordering is then introduced, which is a set of assumptions determining the relative order (in terms of ϵ) of any physical quantity in the system with respect to any other quantity of the same dimension. Strauss uses the following ordering:

$$\begin{gathered}
\frac{\partial}{\partial x}, \frac{\partial}{\partial y} = O(1), \qquad \frac{\partial}{\partial z} = O(\epsilon), \qquad B_x, B_y = O(\epsilon), \\
B_z = O(1) + O(\epsilon^2), \qquad j_x, j_y = O(\epsilon^2), \qquad j_z = O(\epsilon), \qquad \beta = O(\epsilon^2), \\
\rho = O(1), \qquad \vec{v} = O(\epsilon), \qquad \frac{\partial}{\partial t} = O(\epsilon)
\end{gathered} \tag{1.12}$$

where β is the ratio of fluid pressure p to magnetic pressure and (x, y, z) is a Cartesian coordinate system. Toroidal effects are neglected, as the corresponding terms in the equations are of order ϵ^3, and all terms of that order and higher are neglected. Thus, the plasma is a column extending in the z direction, with periodic boundary conditions at the ends. The line $(0, 0, z)$ represents the magnetic axis.

In agreement with the ordering, the z-component of the magnetic field is defined as $B_z = B_0 + B_2$, where $B_0 = \text{const}$ is the cylindrical magnetic field generated by the coils and B_2 is an $O(\epsilon^2)$ correction due to poloidal currents. From the divergence-free condition for $\vec{B}$, one gets

$$\nabla \cdot \vec{B} = \nabla^\perp \cdot \vec{B}^\perp + \frac{\partial B_2}{\partial z} = 0, \tag{1.13}$$

where $\vec{B}^\perp$ are the x and y components of $\vec{B}$ and $\nabla^\perp$ is the gradient operator in the $x-y$ plane. The second term is of order ϵ^3 and can be dropped. What remains is a two-dimensional divergence-free condition on $\vec{B}^\perp$, which means that $\vec{B}^\perp$ can be expressed in terms of a stream function A, which is also the z component of the magnetic vector potential:

$$\vec{B}^\perp = \nabla A \times \widehat{z}. \tag{1.14}$$

The z component of the momentum equation reads:

$$\rho \frac{\partial v_z}{\partial t} + \rho(\vec{v} \cdot \nabla) v_z = j_x B_y - j_y B_x - \frac{\partial p}{\partial z}. \tag{1.15}$$

All terms on the RHS are of order ϵ^3 and can be neglected. Because of this, Strauss sets $v_z = 0$. Next, Faraday's law is rewritten in potential form:

$$\frac{\partial \vec{A}}{\partial t} = \vec{v} \times \vec{B} + \nabla \phi, \tag{1.16}$$

where ϕ is a gauge potential. The x and y components of the vector potential $\vec{A}$ must be of order ϵ^2 in order for B_2 to be of that same order. Therefore, taking the cross product with $\widehat{z}$ and dropping terms of order ϵ^3, one gets:

$$-B_0 \vec{v} + \nabla \phi \times \widehat{z} = 0, \tag{1.17}$$

which means that $\vec{v}$ can also be represented by a stream function:

$$\vec{v} = \nabla U \times \widehat{z}, \tag{1.18}$$

where $U = \phi / B_0$. Now, the z component of equation (1.16) becomes

$$\frac{\partial A}{\partial t} = (\nabla U \times \nabla A) \cdot \widehat{z} B_z \frac{\partial U}{\partial z} = \vec{B} \cdot \nabla U. \tag{1.19}$$

The current is as follows:

$$\vec{j} = \frac{1}{\mu_0} \nabla \times (B_z \widehat{z} + \nabla A \times \widehat{z}) = \frac{1}{\mu_0} \left(\nabla B_z \times \widehat{z} - \Delta^\perp A \widehat{z} + \nabla^\perp \frac{\partial A}{\partial z} \right), \tag{1.20}$$

where $\Delta^\perp = \nabla \cdot \nabla^\perp$. Substituting the current into the momentum equation and

dropping terms of order ϵ^3, one gets

$$\rho\frac{\partial\vec{v}}{\partial t}+\rho(\vec{v}\cdot\nabla)\vec{v}=\frac{B_z}{\mu_0}\nabla\frac{\partial A}{\partial z}\times\widehat{z}-\frac{1}{\mu_0}\Delta^\perp A\nabla^\perp A-\nabla^\perp\left(p+\frac{B_z^2}{2\mu_0}\right). \tag{1.21}$$

Since $\nabla\cdot\vec{v}=0$, one can consider the special case $\rho=$ const, so Strauss normalizes equation (1.21) by ρ. The last step is to take the curl of equation (1.21). After dropping all terms of order ϵ^3, only the z component of the resulting vorticity equation remains. Using equation (1.18), the result is:

$$\Delta^\perp\frac{\partial U}{\partial t}+\vec{v}\cdot\nabla\Delta^\perp U=\frac{1}{\mu_0}\vec{B}\cdot\nabla\Delta^\perp A. \tag{1.22}$$

Equations (1.19) and (1.22) are the two equations of this simple reduced MHD model. Note that B_2 does not enter the equations, since in both equations B_z is multiplied by a factor of order ϵ. Thus, since including B_2 will result in terms of order ϵ^3, $B_z = B_0$ for the purposes of this model. Finally, note that since both the fluid and magnetic field cannot be compressed in this model, there are no fast magnetosonic waves.

While the simple ordering-based reduced MHD model shown here is mostly a toy model, more sophisticated ordering-based models have been derived [9, 19]. These will not be discussed here, as the purpose of this section was just to illustrate the ordering-based approach. All of the models that will be used in this dissertation are ansatz-based, however, some ordering-based arguments will be presented in the later chapters.

1.3.2 Ansatz-based reduced MHD

The ansatz-based approach was first introduced by Park *et al* in the 1980s [20]. Instead of expanding the MHD equations in terms of the inverse aspect ratio, this approach starts with an ansatz for the magnetic field and velocity. Simulations show that fast magnetosonic waves are eliminated when using the ansatzes [18]; this will be confirmed more rigorously in the next chapter. Here, the JOREK reduced MHD model for tokamaks [6, 13] will be presented to illustrate the ansatz-based approach and to serve as a comparison for stellarator-capable reduced MHD, which will be

derived in the next chapters.

The derivation in Ref [13] begins with introducing the ansatzes for the magnetic field and velocity:

$$\begin{aligned} \vec{B} &= F_0 \nabla\phi + \nabla\psi \times \nabla\phi, \\ \vec{v} &= -R^2 \nabla u \times \nabla\phi + v_\parallel \vec{B}. \end{aligned} \tag{1.23}$$

Here, a cylindrical coordinate system (R, z, ϕ) was set up with the origin being the intersection of the axis of symmetry with the midplane. The variables ψ, u and $v_\parallel$ are the unknowns which need to be solved for. These ansatzes are then used in the equations (1.2). Note the similarity of the ansatzes to equations (1.14) and (1.18), which were derived from the ordering. Also note that, due to axisymmetry, the equilibrium ψ is a flux function:

$$(\vec{B} \cdot \nabla\psi)|_{t=0} = \frac{F_0}{R^2} \frac{\partial\psi}{\partial\phi}\bigg|_{t=0} = 0.$$

At this point, two things should be noted. First, the derivation in Ref [13] does not take into account sources and diffusion, i.e. it assumes $\kappa_\parallel = \kappa_\perp = 0$, $P = 0$, $S_e = 0$ and neglects the ηj^2 term in equations (1.2). A derivation with a more complete set of equations is presented in Ref [6]; the derivation summarized here will mostly follow Ref [13]. Second, the viscosity term is not treated in the derivation, meaning that the derivation works with an inviscid momentum equation, and then a generic viscosity term is added in the end.

The first and most trivial step is to insert the ansatzes (1.23) into the continuity and pressure equations in (1.2). Under the source- and diffusion-free assumption, the following equations are obtained:

$$\begin{aligned} \frac{\partial\rho}{\partial t} &= R[\rho, u] + 2\rho\frac{\partial u}{\partial z} - \frac{1}{R}[\rho v_\parallel, \psi] - \frac{F_0}{R^2}\frac{\partial}{\partial\phi}(\rho v_\parallel), \\ \frac{\partial p}{\partial t} &= R[p, u] + 2\gamma p\frac{\partial u}{\partial z} - \frac{F_0 v_\parallel}{R^2}\frac{\partial p}{\partial\phi} - \frac{v_\parallel}{R}[p, \psi] - \frac{\gamma p}{R}[v_\parallel, \psi] - \frac{F_0\gamma p}{R^2}\frac{\partial v_\parallel}{\partial\phi}, \end{aligned} \tag{1.24}$$

where $[f, g] = \widehat{\phi} \cdot (\nabla f \times \nabla g)$ is a Poisson bracket.

The remaining two equations in (1.2) are vector equations, and one cannot use them as is after inserting the ansatzes into them, as there would be more equations then unknowns. Thus, appropriate projection operators need to be applied to the

vector equations in order to obtain a scalar equation for each of the three unknowns ψ, u and $v_\parallel$. First consider Faraday's law, which, after inserting the ansatzes (1.23), becomes:

$$\nabla\frac{\partial\psi}{\partial t}\times\nabla\phi = \nabla\times(F_0\nabla^\perp u + [\psi,u]\widehat{\phi} - \eta\vec{j}),$$

where $\nabla^\perp$ is the gradient operator in the $R-z$ plane and $\vec{j} = \nabla\times(\nabla\psi\times\nabla\phi)/\mu_0$. Since the curl of a gradient is zero, one can subtract $F_0\nabla u$ from the expression under the curl on the LHS. Then, since both sides are curls, the entire equation can be un-curled, resulting in:

$$\frac{\partial\psi}{\partial t}\nabla\phi = -F_0\frac{\partial u}{\partial\phi}\nabla\phi + [\psi,u]\widehat{\phi} - \eta\vec{j}.$$

The last step is to project this equation on $R\widehat{\phi}$. The final equation for ψ is then

$$\frac{\partial\psi}{\partial t} = -F_0\frac{\partial u}{\partial\phi} + R[\psi,u] - \eta j, \tag{1.25}$$

where a simple algebraic calculation shows that $j = R\widehat{\phi}\cdot\vec{j} = \Delta^*\psi/\mu_0$ and $\Delta^* = R^2\nabla\cdot(R^{-2}\nabla^\perp$ is the Grad-Shafranov operator. The R and z components of the current were neglected, and the point of subtracting $F_0\nabla u$ under the curl was to avoid neglecting $\nabla^\perp u$ as well. In Ref [13], an attempt is made to avoid neglecting the R and z components of current by using gauge freedom. However, an error is present in the derivation (a factor of $1/R^2$ slips through a $\partial/\partial R$ derivative unnoticed in equation (2.5)) which makes it seem like the gauge potential can be defined in such a way that its gradient will cancel both the R and z components of current simultaneously, however this is not possible. This error leads to the presence of an extra term, $\eta R^{-2}\partial^2\psi/\partial\phi^2$, in the reduced MHD ψ equation presented in Ref [13], however this term is not implemented in JOREK [6].

Now consider the momentum equation in (1.2). There are two velocity-related unknowns, u and $v_\parallel$, so two different projection operators will be needed, namely:

$$\begin{gathered}\nabla\phi\cdot\nabla\times(R^2,\\ \vec{B}\cdot,\end{gathered} \tag{1.26}$$

Note that, for any vector $\vec{Q}$ and test function u^*, one has, using the identity

$\nabla f \cdot \nabla \times \vec{U} = -\nabla \cdot (\nabla f \times \vec{Q})$ and integration by parts,

$$\int_V u^* \nabla\phi \cdot \nabla \times (R^2 \vec{Q}) dV = \int_V (R^2 \nabla u^* \times \nabla\phi) \cdot \vec{Q} dV,$$

where V is the volume occupied by the plasma and it is assumed that $u^* = 0$ on ∂V. Thus, within the context of the Galerkin method, using this operator amounts to projecting the momentum equation on the subspace of vector functions representable by $R^2 \nabla u^* \times \nabla\phi$, where u^* is an arbitrary scalar function. Inserting the ansatzes (1.23) and applying the first projection operator, the following equation is obtained for u:

$$\begin{aligned}
&\nabla \cdot \left(R^2 \rho \nabla^\perp \frac{\partial u}{\partial t} \right) - \nabla \cdot \left[\rho \frac{\partial}{\partial t} (v_\parallel \nabla^\perp \psi) \right] = \frac{1}{2R} [R^2 (u,u), R^2 \rho] + \frac{1}{R} [R^4 \rho w, u] \\
&- \frac{1}{R} [R^2, p] + \frac{1}{R} [\psi, j] - \frac{F_0}{R^2} \frac{\partial j}{\partial \phi} + \frac{1}{R} [\rho v_\parallel^2 j, \psi] + \frac{1}{R} [\rho v_\parallel (v_\parallel, \psi), \psi] \\
&- \nabla \cdot \left[F_0 \rho v_\parallel \nabla^\perp \left(\frac{\partial u}{\partial \phi} \right) \right] + \frac{1}{R} [R^2 \rho, v_\parallel (\psi, u)] - \frac{1}{2R} \left[R^2 \rho, \frac{v_\parallel^2 (\psi, \psi)}{R^2} \right] \\
&- \frac{1}{R} [R^2 \rho v_\parallel w, \psi] + \frac{1}{R} [u, R^2 \rho v_\parallel j] + \frac{1}{R} [u, R^2 \rho (\psi, v_\parallel)] - \frac{1}{R} \frac{\partial}{\partial z} \left(\frac{F_0^2 \rho v_\parallel^2}{R} \right) \\
&+ \frac{1}{R} \frac{\partial}{\partial R} \left[\frac{F_0 \rho v_\parallel}{R} \frac{\partial}{\partial \phi} \left(v_\parallel \frac{\partial \psi}{\partial R} \right) \right] + \frac{1}{R} \frac{\partial}{\partial z} \left[\frac{F_0 \rho v_\parallel}{R} \frac{\partial}{\partial \phi} \left(v_\parallel \frac{\partial \psi}{\partial z} \right) \right] + \nabla \cdot (\mu_\perp^t \nabla w),
\end{aligned} \tag{1.27}$$

where $w = \Delta^\perp u = \nabla \cdot \nabla^\perp u$ and $(f,g) = \nabla^\perp f \cdot \nabla^\perp g$. The term $\nabla \cdot (\mu_\perp^t \nabla w)$ is the previously mentioned generic viscosity term. Finally, applying the second projection operator after inserting the ansatzes (1.23) results in the equation for $v_\parallel$:

$$\begin{aligned}
&\rho B^2 \frac{\partial v_\parallel}{\partial t} + \frac{\rho v_\parallel}{R^2} \left(\psi, \frac{\partial \psi}{\partial t} \right) - \rho \left(u, \frac{\partial \psi}{\partial t} \right) = -\frac{1}{R} [p, \psi] - \frac{F_0}{R^2} \frac{\partial p}{\partial \phi} + \frac{\rho}{2R} [\psi, v_\parallel^2 B^2] \\
&- \frac{F_0 \rho}{2R} \frac{\partial}{\partial \phi} \left(\frac{v_\parallel^2 B^2}{R} \right) - \frac{\rho}{2R} [R^2 (u,u), \psi] - R \rho w [\psi, u] - R \rho B^2 [u, v_\parallel] \\
&- \frac{\rho v_\parallel j}{R} [u, \psi] - \frac{\rho v_\parallel}{R} [\psi, (\psi, u)] + \frac{F_0 \rho v_\parallel}{R^2} \left(\psi, \frac{\partial \psi}{\partial \phi} \right).
\end{aligned} \tag{1.28}$$

For the sake of simplicity, only reduced MHD models for tokamaks have been presented in this section. Stellarator-capable models have also been derived previously, but most of them only approximately satisfy the condition $\nabla \cdot \vec{B} = 0$, like

the model in Ref [24]. An exception is a newer model by Strauss [9], where the magnetic field is expanded around an arbitrary curl-free background field, without making any assumptions on the geometry while exactly satisfying $\nabla \cdot \vec{B} = 0$. However, the model in Ref [9] is an ordering-based ideal MHD model. The models that will be derived in this dissertation will expand the magnetic field similarly to Ref [9], while following the ansatz-based approach in the context of viscoresistive MHD. In addition, the models will be derived first as an alternate formulation of full MHD, with the reduction being a separate step, much like the approach used by Breslau *et al* [7].

1.4 The JOREK code

JOREK is a fully implicit Galerkin finite element nonlinear MHD code, which is used extensively to study tokamaks. Several different reduced and full MHD models have been implemented [6]. JOREK is one of several major nonlinear MHD codes in the world, with a primarily European community. Several other comparable MHD codes exist, with a few of them, including M3D-C^1 [25], M3D [26] and MIPS [27], having also been expanded to stellarators. All three of these codes use full MHD on flux surface aligned grids, except for MIPS, which uses a cylindrical grid. NIMROD, another major tokamak code, is still in the process of being extended to stellarators [28].

The spatial discretization in JOREK is done via two-dimensional quadrilateral finite elements in the poloidal plane and a toroidal Fourier expansion. The finite element discretization has G^1 continuity, meaning that any discretized functions and their first derivatives are continuous across element boundaries, but second derivatives can jump.

In each element, an element-local coordinate system (s, t, ϕ), $s, t \in [0, 1]$, is set up in each element, where $(s, t) = (0, 0), (0, 1), (1, 0), (1, 1)$ correspond to the four vertices of the element and ϕ is the geometric toroidal angle, identical to the ϕ

coordinate of the cylindrical coordinate system (R, z, ϕ) introduced in the previous section. In general, s and t can be have arbitrary orientations in the poloidal plane, however in most configurations without an X-point, s is the radial coordinate and t is the poloidal coordinate. All quantities, including the cylindrical coordinates R and z, are expressed in terms of the element-local coordinates. Expressing R and z in terms of element-local coordinates allows one to adjust the positions of the vertices of an element, which is normally used to build a flux surface aligned grid. Previously, R and z could only depend on s and t, but not ϕ [6], however a recent development by R. Ramasamy removed this constraint. Now, the cylindrical coordinates inside a particular element are represented as:

$$\{R, z\}(s, t, \phi) = \sum_{n=1}^{N_{\text{ctor}}} \sum_{i=1}^{4} \sum_{j=1}^{4} \{R_{ijn}, z_{ijn}\} B_{ij}(s, t) Z_n^{\text{c}}(\phi), \tag{1.29}$$

where i sums over the four vertices of the element, j sums over the degrees of freedom at each vertex and n sums over the toroidal Fourier modes, with N_{ctor} being an adjustable parameter. In addition, $B_{ij}(s, t)$ are Bezier basis functions, and

$$Z_n^{\text{c}}(\phi) = \begin{cases} 1, & n = 1 \\ \cos\left(N_{\text{cp}} \frac{n}{2} \phi\right), & n \text{ even} \\ \sin\left(N_{\text{cp}} \frac{n-1}{2} \phi\right), & n \text{ odd and } n > 1 \end{cases}$$

where N_{cp} is the periodicity of the underlying geometry. Allowing R and z to depend on ϕ makes it possible to build a flux surface aligned grid in a stellarator configuration. The physical quantities, such as density, temperature and ψ are represented in a similar way:

$$Q(s, t, \phi) = \sum_{n=1}^{N_{\text{tor}}} \sum_{i=1}^{4} \sum_{j=1}^{4} Q_{ijn} B_{ij}(s, t) Z_n(\phi). \tag{1.30}$$

Note that N_{tor} and N_{ctor} are distinct parameters; on a flux surface aligned grid less modes are needed to represent the physical quantities than the geometry. The Fourier basis function $Z_n(\phi)$ is defined in a similar way to $Z_n^{\text{c}}(\phi)$, with the difference that N_{cp} is replaced by N_{p}; this allows running full torus simulations without having

to add unnecessary modes to the geometry.

For clarity, the covariant basis vectors of the element-local coordinate system will be calculated here in terms of the cylindrical basis vectors:

$$\begin{aligned}
\vec{e}_s &= \left(\frac{\partial \vec{r}}{\partial s}\right)_{t,\phi} = \frac{\partial R}{\partial s}\vec{b}_R + R\frac{\partial \vec{b}_R}{\partial s} + \frac{\partial z}{\partial s}\vec{b}_z = \frac{\partial R}{\partial s}\vec{b}_R + \frac{\partial z}{\partial s}\vec{b}_z, \\
\vec{e}_t &= \left(\frac{\partial \vec{r}}{\partial t}\right)_{s,\phi} = \frac{\partial R}{\partial t}\vec{b}_R + R\frac{\partial \vec{b}_R}{\partial t} + \frac{\partial z}{\partial t}\vec{b}_z = \frac{\partial R}{\partial t}\vec{b}_R + \frac{\partial z}{\partial t}\vec{b}_z, \\
\vec{e}_\phi &= \left(\frac{\partial \vec{r}}{\partial \phi}\right)_{s,t} = \frac{\partial R}{\partial \phi}\vec{b}_R + R\frac{\partial \vec{b}_R}{\partial \phi} + \frac{\partial z}{\partial \phi}\vec{b}_z = \frac{\partial R}{\partial \phi}\vec{b}_R + \frac{\partial z}{\partial \phi}\vec{b}_z + \vec{b}_\phi,
\end{aligned} \tag{1.31}$$

where $\vec{r} = R\vec{b}_R + z\vec{b}_z$ is the position vector and cylindrical basis vectors are represented with the letter "b" to avoid confusion. In addition, since the covariant basis vectors $\vec{e}_s$ and $\vec{e}_t$ should lie in the poloidal plane, the derivative of $\vec{b}_R$ with respect to s or t should be zero, as $\vec{b}_R$ is constant in the poloidal plane. The derivative of $\vec{b}_R$ with respect to ϕ can be calculated as follows:

$$\begin{aligned}
\left(\frac{\partial \vec{b}_R}{\partial \phi}\right)_{s,t} &= \vec{e}_\phi \cdot \nabla \vec{b}_R = \vec{e}_\phi \cdot \nabla R \left(\frac{\partial \vec{b}_R}{\partial R}\right)_{z,\phi} + \vec{e}_\phi \cdot \nabla z \left(\frac{\partial \vec{b}_R}{\partial z}\right)_{R,\phi} + \vec{e}_\phi \cdot \nabla \phi \left(\frac{\partial \vec{b}_R}{\partial \phi}\right)_{R,z} \\
&= \left(\frac{\partial \vec{b}_R}{\partial \phi}\right)_{R,z} = \frac{1}{R}\vec{b}_\phi.
\end{aligned}$$

Knowing the covariant basis vectors completely defines the coordinate system. The metric tensor (not shown here) can be easily calculated from the basis vectors, if needed.

Finally, the temporal discretization in JOREK is done using either the Crank-Nicolson, Gears (BDF2) or the implicit Euler time stepping schemes [6]. An evolution equation can be written in the form

$$\frac{\partial \vec{A}(\vec{u})}{\partial t} = \vec{B}(\vec{u}, t),$$

where $\vec{u}$ is the n-dimensional vector of all physical quantities. After discretizing the equation and linearizing it around the current time step, the following general form is obtained:

$$\left[(1+\xi)\left(\frac{\partial \vec{A}}{\partial \vec{u}}\right)^n - \Delta t\theta\left(\frac{\partial \vec{B}}{\partial \vec{u}}\right)^n\right] \cdot \delta\vec{u}^{\,n} = \Delta t\vec{B}^n + \xi\left(\frac{\partial \vec{A}}{\partial \vec{u}}\right)^n \cdot \delta\vec{u}^{\,n-1}, \tag{1.32}$$

where the superscripts refer to the time step at which a particular expression is evaluated at: either the current time step (n), the previous one ($n-1$) or the next one ($n+1$), and $\delta\vec{u}^{\,n} = \vec{u}^{\,n+1} - \vec{u}^{\,n}$. The parameters ξ an θ determine which time stepping scheme is used: $\xi = 0$, $\theta = 1/2$ corresponds to the Crank-Nicolson scheme, $\xi = 1/2$, $\theta = 1$ corresponds to the Gears scheme and $\xi = 0$, $\theta = 1$ corresponds to implicit Euler [6].

After applying the Galerkin method to equations (1.32), a system of linear algebraic equations is obtained, where the unknowns are increments to the finite element degrees of freedom Q_{ijn} (see equation (1.30)). This system is solved iteratively, with the initial guess obtained by breaking the matrix into separate blocks for each Fourier mode and neglecting the cross terms. The initial guess is then refined using the GMRES method [29]. Such a strategy works fine for tokamaks and simple stellarators, such as Wendelstein 7-A, however may become problematic for more complicated stellarators, where mode coupling becomes significant. This issue has been solved in a recent development by I. Holod, where the matrix is broken into blocks that encompass entire mode families, not just individual modes.

2 Derivation of the reduced MHD models

In this chapter, the reduced MHD model, which will be used in later chapters is derived. This model can be seen as a direct generalization of the JOREK tokamak reduced MHD model summarized in section 1.3.2 to stellarators. Indeed, as will be seen, setting the magnetic scalar potential to $\chi = F_0\phi$ reduces the stellarator model back to the tokamak model. This choice of χ will be referred to as the tokamak limit. Unlike the derivation summarized in section 1.3.2, in this chapter, the stellarator models will be derived first as an alternate formulation of full MHD, with the magnetic field and velocity ansatzes being general enough to represent any arbitrary magnetic field and velocity. The reduction is then a separate step, where extra terms in the ansatzes are dropped, much like the approach used by Breslau *et al* [7].

In addition to the main model, a separate reduced model will be derived, which has better momentum conservation properties but does not conserve energy exactly. This alternate model uses the same ansatzes, but different projection operators. This model will be tested in the tokamak limit in the next chapter, but it will not be used for stellarator simulations.

The altenate model was first published in Ref [30]. Ref [31] then uses the same ansatz as Ref [30] to derive the main model.

2.1 Magnetic field and velocity ansatzes

The vector potential of any magnetic field can be represented in a arbitrary coordinate system (q^1, q^2, q^3) using just two covariant components:

$$\vec{A} = A_3 \nabla q^3 + A_1 \nabla q^1, \tag{2.1}$$

where the ∇q^2 component was eliminated using a gauge transform. Now suppose that the total magnetic field $\vec{B}$ in a fusion device is split into a curl-free (vacuum) field $\nabla\chi$, which is generated by the coils, and an induced field $\vec{B}_{\text{ind}}$, which is generated by plasma currents, so that $\vec{B} = \nabla\chi + \vec{B}_{\text{ind}}$. Consider the so-called *Clebsch-type* coordinate system (ψ_v, β_v, χ) aligned to the vacuum magnetic field $\nabla\chi$, where the coordinates satisfy

$$\nabla\chi = \nabla\psi_v \times \nabla\beta_v.$$

As shown in Ref [32], a Clebsch-type coordinate system can be constructed for any divergence-free field; since $\nabla\chi$ is a magnetic field, it must also be divergence-free. It follows that χ must satisfy the Laplace equation.

If the vector potential of the induced magnetic field $\vec{A}_{\text{ind}}$ is expressed in the form (2.1), then the total magnetic field can be expressed as:

$$\vec{B} = \nabla\chi + \nabla\Psi \times \nabla\chi + \nabla\Omega \times \nabla\psi_v, \tag{2.2}$$

where $\Psi = A_\chi$ and $\Omega = A_{\psi_v}$. Note that this ansatz guarantees that $\vec{B}$ will be divergence-free, even if the last term is dropped, as will be done in reduced MHD, since each of the three terms are individually divergence-free. The ansatz also partially fixes the gauge, as one can now only add the gradient of an arbitrary scalar f to $\vec{A}_{\text{ind}}$ if $\partial f/\partial\beta_v = 0$.

Now consider the velocity field. In previous work, Izzo *et al* [8] and Breslau *et al* [7] considered the case when $\chi = F_0\phi$. They use a three-term ansatz for the velocity to separate the MHD waves, where each term contains one of the three waves. Generalizing their expression to $\chi \neq F_0\phi$ while making sure that the first two terms will reduce back to (1.23) in the tokamak limit, the following is obtained:

$$\vec{v} = \frac{\nabla\Phi \times \nabla\chi}{B_v^2} + v_\parallel \vec{B} + \nabla^\perp\zeta, \tag{2.3}$$

where $B_v = |\nabla\chi|$, $\nabla^\perp = \nabla - \nabla^\parallel$ and $\nabla^\parallel = B_v^{-2}\nabla\chi\nabla\chi\cdot\nabla$. In the tokamak limit, the ansatz above matches that of Izzo *et al* and Breslau *et al*, except for the second term, which was made to match the second term in the velocity ansatz (1.23).

The terms in the ansatzes (2.2) and (2.3) can be interpreted as follows. The

magnetic field ansatz consists of the background vacuum field, the field line bending term and the field compression term, while the velocity ansatz consists of the $\vec{E}\times\vec{B}$ flow, field-aligned flow and fluid compression. However, these interpretations are not exact. For example, the last term in the ansatz (2.2) contains $\nabla^{\parallel}\Omega\times\nabla\psi_v$ as a vector component, which contributes a correction to the field line bending. Note that, due to both $\nabla^{\perp}\Omega$ and $\nabla\psi_v$ being orthogonal to $\nabla\chi$, their cross product will be colinear with $\nabla\chi$ and thus will not contribute to field line bending. If an ordering is inroduced, the correction $\nabla^{\parallel}\Omega\times\nabla\psi_v$ is already one order higher than the field compression $\nabla^{\perp}\Omega\times\nabla\psi_v$, which itself is one order higher than the main field line bending term $\nabla\Psi\times\nabla\chi$ in most configurations, so it does not make a significant contribution. Also, as will be shown in section 2.5, the first term in the velocity ansatz (2.3) only matches the $\vec{E}\times\vec{B}$ velocity exactly in ideal reduced MHD. Finally, since all terms in the velocity ansatz (2.3) individually have nonzero divergence, the last term is not the exact fluid compression term.

While it is clear that any magnetic field can be expressed using the ansatz (2.2), it remains to be proven that the ansatz (2.3) does not impose any restrictions on the velocity. To show this, define three projection operators:

$$\begin{gathered}\nabla\chi\cdot\nabla\times[\nabla\chi\times(\vec{e}_\chi\times\\ \nabla\chi\cdot\\ \nabla\cdot[B_v^2\nabla\chi\times(\vec{e}_\chi\times\end{gathered}\tag{2.4}$$

Here, $\vec{e}_\chi=\vec{B}/B^\chi$ is the covariant basis vector in the Clebsch-type coordinate system (α,β,χ) aligned to the total magnetic field $\vec{B}=\nabla\alpha\times\nabla\beta$. The superscript represents a contravariant component: $B^\chi=\nabla\chi\cdot\vec{B}$. The identity $\nabla f\cdot\nabla\times\vec{Q}=-\nabla\cdot(\nabla f\times\vec{Q})$, which follows directly from the divergence of a cross product rule, can be used to rewrite the first projection operator as

$$-\nabla\cdot[\nabla\chi\times(\nabla\chi\times(\vec{e}_\chi\times\tag{2.5}$$

It should be pointed out that the sub-operator $\nabla\chi\times(\vec{e}_\chi\times$ subtracts out the contravariant χ component of a vector: $\nabla\chi\times(\vec{e}_\chi\times\vec{Q})=-\vec{Q}+Q^\chi\vec{e}_\chi$. Applying the

three projection operators to the ansatz (2.3), gives the equations for the three scalar functions Φ, $v_\parallel$ and ζ:

$$\begin{aligned} \Delta^\perp \Phi &= \nabla\chi \cdot \nabla \times [\nabla\chi \times (\vec{e}_\chi \times \vec{v})], \\ v_\parallel &= \frac{v^\chi}{B^\chi}, \\ \nabla \cdot (B_v^2 \nabla^\perp \zeta) &= -\nabla \cdot [B_v^2 \nabla\chi \times (\vec{e}_\chi \times \vec{v})]. \end{aligned} \tag{2.6}$$

As can be seen, once the velocity field is specified, Φ and ζ are given each determined by solving a linear differential equation $v_\parallel$ is given by a direct relation. Both differential equations are generalized Poisson equations. The boundary conditions for these equations can be determined as follows. In a fixed-boundary simulation, the velocity must satisfy $\vec{n}\cdot\vec{v} = 0$ on the boundary, where $\vec{n}$ is the unit normal vector to the boundary. Assuming that the plasma is surrounded by a perfect conductor, as will be done in the simulations presented in this dissertation, the magnetic field must satisfy $\vec{n} \cdot \vec{B} = 0$. Thus, the velocity boundary condition becomes

$$\vec{n} \cdot \frac{\nabla\Phi \times \nabla\chi}{B_v^2} + \vec{n} \cdot \nabla^\perp \zeta = 0.$$

Imposing a Dirichlet condition of $\Phi = 0$ on the boundary makes $\nabla\Phi$ colinear with $\vec{n}$, so a cross product involving $\nabla\Phi$ will be orthogonal to $\vec{n}$ and the first term above is zero. What remains is a Neumann boundary condition for ζ: $\vec{n} \cdot \nabla^\perp \zeta = 0$. The consistency condition for the third equation in (2.6) and the boundary condition is

$$\oint_{\partial V} B_v^2 \nabla^\perp \zeta \cdot d\vec{S} = -\int_V \nabla \cdot [B_v^2 \nabla\chi \times (\vec{e}_\chi \times \vec{v})] dV = \oint_{\partial V} B_v^2 (\vec{v} - v_\parallel \vec{B}) \cdot d\vec{S}.$$

The LHS is zero due to the boundary condition, and the $v_\parallel \vec{B}$ term on the RHS is zero due to the magnetic field boundary condition. Thus, the Neumann boundary condition is consistent with the equation as long as the prescribed vector field $\vec{v}$ itself satisfies to the boundary condition $\vec{n} \cdot \vec{v} = 0$. Clearly, it would not make much sense to try to calculate the scalar functions Φ, $v_\parallel$ and ζ assuming a fixed boundary from a vector field $\vec{v}$ if that vector field itself is not compatible with a fixed boundary setup.

2.2 MHD waves and the velocity ansatz

Using ideal linearized MHD, it can be shown that the three terms of the velocity ansatz (2.3) approximately separate the MHD waves, with each term containing a specific wave. In addition to the assumptions leading up equation (1.10), which will be used shortly, one must also assume that the induced part of the equilibrium magnetic field is much smaller than the coil-generated vacuum field:

$$\frac{|\vec{B}_0 - \nabla\chi|}{|\nabla\chi|} \ll 1. \tag{2.7}$$

Using this assumption, $\vec{B}_0$ will be approximated by $\nabla\chi$. Meanwhile, it is not necessary to neglect $\vec{j}_0 = \frac{1}{\mu_0}\nabla \times \vec{B}_0$, as the equilibrium current $\vec{j}_0$ does not affect the following analysis.

Approximating $\vec{B}_0$ by $\nabla\chi$, equation (1.10) becomes

$$\begin{aligned}\rho_0 \frac{\partial^2 \vec{v}}{\partial t^2} = \vec{j}_0 \times [\nabla \times (\vec{v} \times \nabla\chi)] + \frac{1}{\mu_0}[\nabla \times [\nabla \times (\vec{v} \times \nabla\chi)]] \times \nabla\chi \\ + \nabla(\vec{v} \cdot \nabla p_0) + \gamma\nabla(p_0 \nabla \cdot \vec{v}).\end{aligned} \tag{2.8}$$

Similarly to an elastic solid, a plasma can support both fluid-compressional and shear waves. The individual terms in a typical elastic wave equation, as given in Ref [33], can be compared to the terms in equation (2.8). The second term on the RHS of equation (2.8), which can compress the magnetic field, but not the fluid, has a structure similar to the shear wave term in the elastic wave equation, while the last term on in equation (2.8) is similar to the compressional wave term in the elastic wave equation. Notice that the other two terms on the RHS of equation (2.8) do not contain second order derivatives of the velocity, so these terms do not produce wave-like behavior.

To show that each term of the velocity anstaz (2.3) contains a specific MHD wave, one can insert each term individually into equation (2.8). Note that, since each term contains only one unknown scalar function, inserting just one term into the vector equation in general results in an overconstrained equation. However, the point of this excercise is to analyze the interplay of the structure of the terms in the velocity ansatz (2.3) with the terms in the equation (2.8); to actually solve the

linear equations, one would need to apply the corresponding projection operator, as done in the next section. Inserting the first term from the velocity ansatz into the equation gives:

$$\begin{aligned}\frac{\rho_0}{B_v^2}\frac{\partial^2 \nabla\Phi}{\partial t^2}\times\nabla\chi = -\vec{j}_0\times(\nabla\times\nabla^\perp\Phi) - \frac{1}{\mu_0}[\nabla\times(\nabla\times\nabla^\perp\Phi)]\times\nabla\chi \\ + \nabla\left(\frac{1}{B_v}[p_0,\Phi]\right) - 2\gamma\nabla\left(\frac{p_0}{B_v^2}[B_v,\Phi]\right),\end{aligned} \tag{2.9}$$

where $[f,g] = B_v^{-1}\nabla\chi\cdot(\nabla f\times\nabla g)$ is the Poisson bracket of two scalar fields f and g. While the first term of the velocity ansatz captures both shear Alfvén waves and many instabilities, this section is only concerned with waves, namely with identifying the type of MHD wave contained in each term of the ansatz. The wave type can be identified by determining the phase velocity of wave-like perturbations, which is given by the coefficient in front of the term in the wave equation that contains the second order derivative of the unknown [14, 34].

Since equation (2.9) contains third order derivatives of Φ, it makes sense to let the unknown be the first derivatives of Φ rather than Φ itself, so that equation (2.9) takes the form of a wave equation. Let $\nabla^\perp\Phi$, which, as shown in section 2.5, can be interpreted as the component of the electric field perpendicular to the vacuum magnetic field in ideal reduced MHD, be the unknown in equation (2.9). Only the second term on the RHS of equation (2.9) contains third order derivatives of Φ, which, conveniently, are expressed as second order derivatives of $\nabla^\perp\Phi$; what is left of the fluid compressional term only contains second derivatives of Φ. Thus, only the second term is needed to identify the wave; this term can be rewritten as

$$-\frac{1}{\mu_0}[\nabla^\perp(\Delta^\perp\Phi) - \Delta^\perp(\nabla^\perp\Phi) - \Delta^\parallel(\nabla^\perp\Phi)]\times\nabla\chi, \tag{2.10}$$

where the identities $\nabla\times(\nabla\times\vec{A}) = \nabla(\nabla\cdot\vec{A}) - \Delta\vec{A}$, $\nabla = \nabla^\perp + \nabla^\parallel$ and $\Delta = \Delta^\perp + \Delta^\parallel$ were used, with $\Delta^\parallel = \nabla\cdot\nabla^\parallel$. It is important to note that, while the operators $\Delta^\perp$ and $\nabla^\perp$ do not commute when the vacuum field $\nabla\chi$ is not uniform, the third order derivatives cancel in their commutator, and only the $-\Delta^\parallel(\nabla^\perp\Phi)$ term contains third order derivatives of Φ. Taking the cross product of equation (2.9) with $\nabla\chi$

on the the left and dividing by ρ_0 gives

$$\frac{\partial^2 \nabla^\perp \Phi}{\partial t^2} = \frac{B_v^2}{\mu_0 \rho_0}\left[\Delta^\parallel(\nabla^\perp\Phi) + [\Delta^\perp, \nabla^\perp]\Phi\right] - \frac{\nabla\chi}{\mu_0\rho_0}\nabla\chi\cdot\left[[\Delta^\parallel, \nabla^\perp]\Phi + [\Delta^\perp, \nabla^\perp]\Phi\right] + \frac{j_0^\chi}{\rho_0}\nabla\times\nabla^\perp\Phi + \frac{1}{\rho_0}\nabla\chi\times\nabla\left(\frac{1}{B_v}[p_0,\Phi]\right) - \frac{2\gamma}{\rho_0}\nabla\chi\times\nabla\left(\frac{p_0}{B_v^2}[B_v,\Phi]\right). \tag{2.11}$$

In the above equation, square brackets applied to operators instead of scalar functions are to be understood as the commutator: $[A, B]f = A(Bf) - B(Af)$. In a sense, the commutator is a type of Poisson bracket that acts on operators instead of scalar functions. Note that the commutator $[\Delta^\parallel, \nabla^\perp]$ also does not contain third order derivatives. As can be seen from the only term containing third order derivatives, waves in the vector field $\nabla^\perp\Phi$ will propagate with the Alfvén velocity along field lines. Also note that the fluid velocity, $\nabla\Phi\times\nabla\chi/B_v^2$ is orthogonal to field lines. However, unlike the uniform case presented in section 1.2.1, the divergence of the fluid velocity is nonzero due to the magnetic field curvature [14]. Thus, the first term contains Alfvén waves.

Proceeding to the second term in the velocity ansatz (2.3), note that using assumption (2.7) along with the assumptions of linearized MHD, the second term is approximated as

$$v_\parallel\vec{B} = v_\parallel(\vec{B}_0 + \vec{B}_1) \approx v_\parallel\nabla\chi, \tag{2.12}$$

due to both $v_\parallel$ and $\vec{B}_1$ being first order quantities in linearized MHD. While, from the linear MHD standpoint, there is not much difference in using the vacuum magnetic field instead of the total field in the second term, the choice becomes important for nonlinear effects. For example, using the total field allows the temperature and density profiles to flatten in a region where the magnetic field is stochastic.

After inserting (2.12) into (2.8), the equation becomes:

$$\rho_0\frac{\partial^2 v_\parallel}{\partial t^2}\nabla\chi = \gamma\nabla(B_v p_0 \partial^\parallel v_\parallel), \tag{2.13}$$

where $\partial^\parallel = B_v^{-1}\nabla\chi\cdot\nabla$ is the derivative along the vacuum field. Since $\nabla p_0 = \vec{j}_0\times\vec{B}_0$ and $\vec{B}_0 \approx \nabla\chi$ (assumption (2.7)), it follows that $\partial^\parallel p_0 \approx 0$; this allows one to drop the third term on the RHS of equation (2.8) and only the fluid compressional term

is left. Dotting the equation with $\nabla\chi/(\rho_0 B_v^2)$ and expanding the derivative in the RHS gives

$$\begin{aligned}\frac{\partial^2 v_\parallel}{\partial t^2} &= \frac{\gamma p_0}{\rho_0}(\partial^\parallel)^2 v_\parallel + \frac{\gamma p_0}{\rho_0 B_v}\partial^\parallel v_\parallel \partial^\parallel B_v \\ &= \frac{\gamma p_0}{\rho_0}\Delta^\parallel v_\parallel + \frac{2\gamma p_0}{\rho_0 B_v}\partial^\parallel v_\parallel \partial^\parallel B_v.\end{aligned} \tag{2.14}$$

As can be seen from the first term on the RHS, waves in the scalar field $v_\parallel$ will move with the sound speed along field lines, and the fluid velocity $v_\parallel \nabla\chi$ is directed along field lines. Thus, the second term in the ansatz contains slow magnetosonic waves. Note, however, that the waves propagate with the sound speed and not with the slow magnetosonic speed due to the velocity being constrained to be strictly in the direction of the field lines, which eliminates the shear term, preventing the magnetic field from being compressed. Thus, the wave can only compress the fluid, forcing it to act like a sound wave confined to propagating along field lines due to its longitudinal nature. A true slow magnetosonic wave can emerge when the third term in the velocity ansatz is present, via coupling between the two terms.

At this point, after having considered the first two terms in the velocity ansatz, it should be pointed out that these first two terms do not compress the magnetic field even in the nonlinear regime. This can be shown by projecting the ideal Faraday's law on $\nabla\chi$, after inserting the magnetic field ansatz (2.2) and the first two terms of the velocity ansatz (2.3):

$$\frac{\partial B^\chi}{\partial t} = B_v\left[\frac{\partial\Omega}{\partial t},\psi_v\right] = \nabla\chi\cdot\nabla\times(\vec{v}\times\vec{B}) = B_v\left[\frac{[\psi_v,\Phi]}{B_v},\Omega\right] - B_v\left[\frac{[\Omega,\Phi]}{B_v},\psi_v\right]. \tag{2.15}$$

The contribution to the component of the magnetic field along $\nabla\chi$ that does not come from $\nabla\chi$ itself corresponds to field compression. As discussed in the previous section, the Ω term in the magnetic field ansatz (2.2) contains both the field compression and a correction to field line bending, however, the field line bending correction is due to $\partial^\parallel\Omega \neq 0$, and $\partial^\parallel\Omega$ does not contribute to the Poisson brackets in the equation above. Thus, if there is no field compression at $t = 0$, $\partial B^\chi/\partial t = 0$, meaning that the field cannot be compressed at any point in the simulation. For this reason, it is appropriate to drop the Ω term of the magnetic field ansatz (2.2)

in the context of reduced MHD, where the third term of the velocity ansatz (2.3) is not present. Note that the effect of resistivity is not considered here. Resistivity can lead to a nonzero value of $\partial B^x/\partial t$, however it is unrelated to the velocity ansatz terms, and practice shows that it is usually small enough to neglect.

To conclude this section, consider the last term of the velocity ansatz (2.3). After substituting it into equation (2.8), one gets

$$\rho_0 \frac{\partial^2 \nabla^\perp \zeta}{\partial t^2} = \vec{j}_0 \times [\nabla \times (\nabla\zeta \times \nabla\chi)] - \frac{1}{\mu_0}\Delta(\nabla\zeta \times \nabla\chi) \times \nabla\chi + \nabla(\zeta, p_0) + \gamma\nabla(p_0 \Delta^\perp \zeta), \tag{2.16}$$

where $(f, g) = \nabla^\perp f \cdot \nabla^\perp g$ is the inner product of the components of the gradients of f and g perpendicular to $\nabla\chi$. As was done when examining the first term in the velocity ansatz, let the perpendicular gradient $\nabla^\perp\zeta$ be the unknown. Since the time derivative on the LHS does not have a component along $\nabla\chi$, one only needs to consider the perpendicular component of the RHS. Expanding the second term on the RHS using the identity $\Delta(\vec{A} \times \vec{B}) = (\Delta\vec{A}) \times \vec{B} + 2\nabla\vec{A} \overset{\bullet}{\times} \nabla\vec{B} + \vec{A} \times (\Delta\vec{B})$ and dividing by ρ_0, the perpendicular component of equation (2.16) becomes

$$\begin{aligned}\frac{\partial^2 \nabla^\perp \zeta}{\partial t^2} = {} & \frac{\vec{j}_0}{\rho_0} \times [\nabla \times (\nabla\zeta \times \nabla\chi)] - \frac{\nabla\chi}{B_v\rho_0} \cdot [\vec{j}_0 \times [\nabla \times (\nabla\zeta \times \nabla\chi)]] + \frac{B_v^2}{\mu_0\rho_0}\Delta(\nabla^\perp\zeta) \\ & - \frac{\nabla\chi}{\mu_0\rho_0}(\nabla\chi \cdot [\Delta, \nabla^\perp]\zeta) + \frac{2}{\mu_0\rho_0}\nabla\chi \times (\nabla\nabla^\perp\zeta \overset{\bullet}{\times} \nabla\nabla\chi) + \frac{1}{\rho_0}\nabla^\perp(\zeta, p_0) \\ & + \frac{\gamma}{\rho_0}\Delta^\perp\zeta\nabla^\perp p_0 + \frac{\gamma p_0}{\rho_0}\Delta^\perp(\nabla^\perp\zeta) + \frac{\gamma p_0}{\rho_0}[\nabla^\perp, \Delta^\perp]\zeta,\end{aligned} \tag{2.17}$$

where $\overleftrightarrow{T} \overset{\bullet}{\times} \overleftrightarrow{U} = \epsilon_{ijk} J T^{lj} U_l{}^k \vec{e}^{\,i}$ is the dot-cross product of two tensors, ϵ_{ijk} is the Levi-Civita symbol and J is the Jacobian. As third order derivatives are not present in the commutators, only the third and eighth terms have third order derivatives of ζ. These two terms can be expressed as

$$\left(\frac{B_v^2}{\mu_0\rho_0} + \frac{\gamma p_0}{\rho_0}\right)\Delta^\perp(\nabla^\perp\zeta) + \frac{B_v^2}{\mu_0\rho_0}\Delta^\parallel(\nabla^\perp\zeta). \tag{2.18}$$

Unlike the first two terms in the velocity ansatz, the wave contained in the third term can propagate both across and along field lines, but the phase velocity depends

on the direction of propagation. In general, the phase velocity of this wave is

$$c_w = \sqrt{(c_A^2 + c_s^2)\sin^2\theta + c_A^2\cos^2\theta} = \sqrt{c_A^2 + c_s^2 - c_s^2\cos^2\theta}, \tag{2.19}$$

where θ is the angle between the direction of wave propagation and $\nabla\chi$, $c_A = B_v/\sqrt{\mu_0\rho_0}$ is the Alfvén velocity and $c_s = \sqrt{\gamma p_0/\rho_0}$ is the sound speed. This is not quite the fast magnetosonic wave speed, which, according to the dispersion relation solution for a uniform equilibrium (1.8), should be

$$c_f = \sqrt{\frac{1}{2}(c_A^2 + c_s^2)\left(1 + \sqrt{1 - 4\cos^2\theta\frac{c_A^2 c_s^2}{(c_A^2 + c_s^2)^2}}\right)}. \tag{2.20}$$

The phase velocities (2.19) and (2.20) match when $\theta = 0$, both being c_A and also when $\theta = \pi/2$, where both equal $\sqrt{c_A^2 + c_s^2}$. For arbitrary θ, the error in the fast magnetosonic speed as estimated by (2.19) is still small in the fusion relevant $\beta < 1$ regime. Note that when $\beta < 1$, $c_s < c_A$. In the $c_s \leq c_A$ regime, which also includes a certain range of β values above 1, the error is maximized to about 9% when $c_s = c_A$ (corresponding to $\beta = 2/\gamma$, which is already greater than 1), and $\theta = \arccos(\pm\sqrt{2\sqrt{2} - 2})$. The situation is similar to what was seen before for the slow magnetosonic wave. As the third term in the velocity ansatz is constrained to being perpendicular to $\nabla\chi$, it cannot separate out the fast magnetosonic wave exactly, and so both the second and third terms are needed in order to have a true fast magnetosonic wave. Nevertheless, the third term still isolates the fast $\sqrt{c_A^2 + c_s^2}$ dynamics, the elimination of which is sufficient for the purposes of reduced MHD.

2.3 Derivation of the main set of equations

Having introduced the new velocity variables Φ, $v_\parallel$ and ζ and the new magnetic field variables Ψ and Ω, the set of unknowns for the MHD system becomes $\{\rho, p, \Phi, v_\parallel, \zeta, \Psi, \Omega\}$. The equations for these variables can be derived from the viscoresistive MHD equations (1.2) as follows. For the density ρ and pressure p, one can use the continuity and internal energy equations (first and third equations in

(1.2)) directly, after plugging in the ansatzes (2.2) and (2.3):

$$\frac{\partial \rho}{\partial t} = -B_v \left[\frac{\rho}{B_v^2}, \Phi\right] - B_v \partial^{\parallel}(\rho v_{\parallel}) - B_v[\rho v_{\parallel}, \Psi] - F_v[\rho v_{\parallel}, \Omega]_{\psi_v} - \nabla\cdot(\rho\nabla^{\perp}\zeta) + P, \quad (2.21)$$

$$\begin{aligned}\frac{\partial p}{\partial t} = &-\frac{1}{B_v}[p,\Phi] - v_{\parallel}B_v\partial^{\parallel}p - v_{\parallel}B_v[p,\Psi] - v_{\parallel}F_v[p,\Omega]_{\psi_v} - (\zeta,p) - \gamma p B_v\left[\frac{1}{B_v^2},\Phi\right]\\ &- \gamma p B_v\partial^{\parallel}v_{\parallel} - \gamma p B_v\left[v_{\parallel},\Psi\right] - \gamma p F_v\left[v_{\parallel},\Omega\right]_{\psi_v} - \gamma p\Delta^{\perp}\zeta + \nabla\cdot\Bigg[(\gamma-1)\frac{\kappa_{\perp}}{R}\nabla\left(\frac{p}{\rho}\right)\\ &+ (\gamma-1)\frac{\kappa_{\parallel}-\kappa_{\perp}}{RB^2}\vec{B}\left(B_v\partial^{\parallel}\left(\frac{p}{\rho}\right) + B_v\left[\frac{p}{\rho},\Psi\right] + F_v\left[\frac{p}{\rho},\Omega\right]_{\psi_v}\right)\\ &+ \frac{pD_{\perp}}{\rho}\left(\nabla\rho - \frac{\vec{B}}{B^2}(B_v\partial^{\parallel}\rho + B_v[\rho,\Psi] + F_v[\rho,\Omega]_{\psi_v})\right)\Bigg] + (\gamma-1)(S_e + \eta j^2),\end{aligned} \quad (2.22)$$

where $F_v = |\nabla\psi_v|$, $\partial_{\psi_v} = F_v^{-1}\nabla\psi_v\cdot\nabla$, $[f,g]_{\psi_v} = F_v^{-1}\nabla\psi_v\cdot(\nabla f\times\nabla g)$ is a Poisson bracket with respect to $\nabla\psi_v$ and

$$\begin{aligned}P &= \nabla\cdot\left[D_{\perp}\nabla\rho - \frac{D_{\perp}\vec{B}}{B^2}(B_v\partial^{\parallel}\rho + B_v[\rho,\Psi] + F_v[\rho,\Omega]_{\psi_v})\right] + S_{\rho},\\ \vec{j} &= \frac{1}{\mu_0}[-\nabla\chi\Delta\Psi + B_v\partial^{\parallel}\nabla\Psi - (\nabla\Psi\cdot\nabla)\nabla\chi + \nabla\Omega\Delta\psi_v - \nabla\psi_v\Delta\Omega\\ &\quad + F_v\partial_{\psi_v}\nabla\Omega - (\nabla\Omega\cdot\nabla)\nabla\psi_v].\end{aligned} \quad (2.23)$$

To derive the equations for the magnetic field variables Ψ and Ω, one begins by inserting the magnetic field and velocity ansatzes (2.2) and (2.3) into Faraday's law in (1.2), which results in

$$\begin{aligned}\nabla\frac{\partial\Psi}{\partial t}\times\nabla\chi + \nabla\frac{\partial\Omega}{\partial t}\times\nabla\psi_v = \nabla\times\Bigg[&\frac{\nabla\chi}{B_v}(\partial^{\parallel}\Phi - [\Psi,\Phi]) + \frac{\nabla\Omega}{B_v}[\psi_v,\Phi] - \frac{\nabla\psi_v}{B_v}[\Omega,\Phi]\\ &+ \nabla\zeta\times\nabla\chi - \nabla\chi(\zeta,\Psi) + \nabla\Omega(\zeta,\psi_v) - \nabla\psi_v(\zeta,\Omega) - \eta\vec{j}\Bigg].\end{aligned} \quad (2.24)$$

The individual scalar evolution equations for Ψ and Ω are then obtained by projecting the above equation on $\nabla\psi_v$ and $\nabla\chi$:

$$\begin{aligned}\left[\psi_v, \frac{\partial\Psi}{\partial t}\right] = &\left[\frac{[\Psi,\Phi] - \partial^{\parallel}\Phi}{B_v}, \psi_v\right] - \frac{F_v}{B_v}\left[\Omega, \frac{[\psi_v,\Phi]}{B_v}\right]_{\psi_v} + \partial^{\parallel}(F_v\partial_{\psi_v}\zeta)\\ &+ [(\zeta,\Psi),\psi_v] - \frac{F_v}{B_v}[\Omega,(\zeta,\psi_v)]_{\psi_v} + \frac{1}{B_v}\nabla\cdot(\eta\nabla\psi_v\times\vec{j}),\end{aligned} \quad (2.25)$$

$$\begin{aligned}\left[\frac{\partial\Omega}{\partial t},\psi_v\right] = &-\left[\Omega,\frac{[\psi_v,\Phi]}{B_v}\right]+\left[\psi_v,\frac{[\Omega,\Phi]}{B_v}\right]-2(B_v,\zeta)-B_v\Delta^{\perp}\zeta\\ &-[\Omega,(\zeta,\psi_v)]+[\psi_v,(\zeta,\Omega)]+\frac{1}{B_v}\nabla\cdot(\eta\nabla\chi\times\vec{j}).\end{aligned} \tag{2.26}$$

Finally, to get the scalar evolution equations for the velocity variables Φ, $v_{\parallel}$ and ζ, the following projection operators should be applied to the momentum equation in (1.2):

$$\begin{gathered}\nabla\chi\cdot\nabla\times(B_v^{-2}\\ \vec{B}\cdot\\ \nabla\chi\cdot\nabla\times(B_v^{-2}\nabla\chi\times\end{gathered} \tag{2.27}$$

As will be shown in section 2.6.1, these projection operators are chosen so that energy is conserved in reduced MHD. After inserting the magnetic field and velocity ansatzes, the momentum equation becomes

$$\rho\nabla\frac{\partial\Phi}{\partial t}\times\frac{\nabla\chi}{B_v^2}+\rho\frac{\partial}{\partial t}(v_{\parallel}\vec{B})+\rho\nabla^{\perp}\frac{\partial\zeta}{\partial t}+\frac{\rho}{2}\nabla v^2+\rho\vec{\omega}\times\vec{v}+\vec{v}P=\vec{j}\times\vec{B}-\nabla p, \tag{2.28}$$

where identity $(\vec{v}\cdot\nabla)\vec{v}=\frac{1}{2}\nabla v^2+\vec{\omega}\times\vec{v}$ was used and $\vec{\omega}$ is the vorticity:

$$\vec{\omega}=\nabla\times\vec{v}=-\nabla\chi\nabla\cdot\left(\frac{\nabla\Phi}{B_v^2}\right)+B_v\partial^{\parallel}\frac{\nabla\Phi}{B_v^2}-\frac{\nabla\Phi\cdot\nabla}{B_v^2}\nabla\chi+\nabla v_{\parallel}\times\vec{B}+\mu_0 v_{\parallel}\vec{j}+\nabla\chi\times\nabla\frac{\partial^{\parallel}\zeta}{B_v}. \tag{2.29}$$

Just as in Ref [13] (see section 1.3.2), the viscous term of the momentum equation (1.2) will not be treated in this derivation, as it is anyway only a rough estimate of the divergence of the viscous stress tensor. Instead, a generic viscosity term will be added to each of the scalar evolution equations after the derivation.

The equation for Φ is derived by applying the first projection operator in (2.27)

or its equivalent, $-\nabla\cdot(B_v^{-2}\nabla\chi\times$, when deemed more appropriate:

$$\nabla\cdot\left[\frac{\rho}{B_v^2}\nabla^\perp\frac{\partial\Phi}{\partial t}+\rho\frac{\partial}{\partial t}(v_\parallel\nabla^\perp\Psi)-\frac{\rho}{B_v}\frac{\partial}{\partial t}(v_\parallel\partial^\parallel\Omega)\nabla\psi_v\right]-B_v\left[\frac{\rho}{B_v^2},\frac{\partial\zeta}{\partial t}\right]=\frac{B_v}{2}\left[\frac{\rho}{B_v^2},v^2\right]$$
$$+B_v\left[\frac{\rho\omega^\chi}{B_v^4},\Phi\right]-\nabla\cdot(\rho v_\parallel\vec{\omega}^\perp)+B_v\left[\frac{\rho v_\parallel\omega^\chi}{B_v^2},\Psi\right]+B_v\left[\frac{\rho v_\parallel\omega^{\psi_v}}{B_v^2},\Omega\right]$$
$$-B_v\left[\frac{\rho v_\parallel\vec{\omega}\cdot\nabla\Omega}{B_v^2},\psi_v\right]+\nabla\cdot\left(\frac{\rho\omega^\chi}{B_v^2}\nabla^\perp\zeta-\frac{P}{B_v^2}\nabla^\perp\Phi-Pv_\parallel\nabla^\perp\Psi+\frac{Pv_\parallel\partial^\parallel\Omega}{B_v}\nabla\psi_v\right)$$
$$+B_v\left[\frac{P}{B_v^2},\zeta\right]+\nabla\cdot\left(\frac{B^\chi}{B_v^2}\vec{j}-\frac{j^\chi}{B_v^2}\vec{B}\right)+B_v\left[\frac{1}{B_v^2},p\right]+\nabla\cdot(\mu_\perp\nabla^\perp\Delta^\perp\Phi),\tag{2.30}$$

where superscripts indicate contravariant vector components, i.e. $Q^f=\nabla f\cdot\vec{Q}$, and $\vec{Q}^\perp=\vec{Q}-Q^\chi\nabla\chi/B_v^2$ is the vector component perpendicular to the vacuum field. The generic viscosity term $\nabla\cdot(\mu_\perp\nabla^\perp\Delta^\perp\Phi)$, which was added to the above equation, was chosen to match the generic viscosity term in Ref [13] (see section 1.3.2). It should be pointed out that the viscosity coefficient $\mu_\perp$ in equation (2.30) is not the same as the physical viscosity μ from the momentum equation (1.2): a simple dimensional analysis shows that the SI units for $\mu_\perp$ are $\mathrm{T}^2\cdot\mathrm{Pa}\cdot\mathrm{s}$. In other words, $\mu_\perp$ has a dimensionality of viscosity times magnetic field squared. Note that $\nabla\chi\cdot\nabla\times(B_v^{-2}\mu\Delta\vec{v})$, which consists of the first projection operator (2.27) applied to the viscous term from (1.2), scales as $\mu B_v^{-2}\Phi/L_\perp^4$, where only the first term of the velocity ansatz was used for scaling purposes, and $L_\perp$ is the length scale perpendicular to the magnetic field, with $L_\perp\ll L_\parallel$ being true for most magnetic fusion configurations. The same scaling analysis gives the following for the generic viscosity term: $\nabla\cdot(\mu_\perp\nabla^\perp\Delta^\perp\Phi)\sim\mu_\perp\Phi/L_\perp^4$. Thus, comparing the two, one has $\mu_\perp\sim\mu B_v^{-2}$. Since the scaling is just an order of magnitude estimate, one can neglect the spatial variation of B_v and just take its value at the axis as the typical value: $\mu_\perp\sim\mu B_{v,axis}^{-2}$.

To obtain the $v_\parallel$ evolution equation, one simply has to project equation (2.28) on $\vec{B}$, which is what the action of the second projection operator in (2.27) amounts

to:

$$\rho\left(\frac{\partial\Phi}{\partial t},\Psi\right)-\rho\frac{F_v}{B_v}\partial^{\parallel}\Omega\partial_{\psi_v}\frac{\partial\Phi}{\partial t}+\rho B^2\frac{\partial v_{\parallel}}{\partial t}+\frac{\rho v_{\parallel}}{2}\frac{\partial B^2}{\partial t}+\rho B_v\left[\frac{\partial\zeta}{\partial t},\Psi\right]+\rho F_v\left[\frac{\partial\zeta}{\partial t},\Omega\right]_{\psi_v}$$
$$=-\frac{\rho B_v}{2}\partial^{\parallel}v^2-\frac{\rho B_v}{2}\left[v^2,\Psi\right]-\frac{\rho F_v}{2}\left[v^2,\Omega\right]_{\psi_v}-\frac{\rho\omega^{\chi}}{B_v}\partial^{\parallel}\Phi-\frac{\rho\omega^{\chi}}{B_v}\left[\Phi,\Psi\right]$$
$$-\frac{\rho\omega^{\chi}F_v}{B_v^2}\left[\Phi,\Omega\right]_{\psi_v}+\frac{\rho B^{\chi}}{B_v^2}\vec{\omega}\cdot\nabla\Phi-\rho\vec{\omega}\cdot(\nabla\zeta\times\nabla\chi)+\rho\omega^{\chi}(\Psi,\zeta)-\rho\vec{\omega}\cdot\nabla\Omega F_v\partial_{\psi_v}\zeta$$
$$+\rho\omega^{\psi_v}(\Omega,\zeta)-\vec{v}\cdot\vec{B}\;P-B_v\partial^{\parallel}p-B_v\left[p,\Psi\right]-F_v\left[p,\Omega\right]_{\psi_v}+\nabla\cdot(\mu_{\parallel}\nabla^{\perp}v_{\parallel}),\tag{2.31}$$

Again, a generic viscosity term was added; this term was chosen to be analogous to the generic viscosity term of equation (2.30).

The scalar evolution equation for ζ is derived by applying the last projection operator in (2.27), or its equivalent, $-\nabla\cdot[B_v^{-2}\nabla\chi\times(\nabla\chi\times$, when appropriate, to each term in equation (2.28):

$$B_v\left[\frac{\rho}{B_v^2},\frac{\partial\Phi}{\partial t}\right]+B_v\left[\rho\frac{\partial v_{\parallel}}{\partial t},\Psi\right]+B_v\left[\rho v_{\parallel},\frac{\partial\Psi}{\partial t}\right]-B_v\left[\frac{\rho}{B_v}\frac{\partial}{\partial t}(v_{\parallel}\partial^{\parallel}\Omega),\psi_v\right]$$
$$+\nabla\cdot\left(\rho\nabla^{\perp}\frac{\partial\zeta}{\partial t}\right)=-\nabla\cdot\left(\frac{\rho}{2}\nabla^{\perp}v^2+\frac{\rho\omega^{\chi}}{B_v^2}\nabla^{\perp}\Phi-\frac{\rho v_{\parallel}B^{\chi}}{B_v^2}\nabla\chi\times\vec{\omega}+\frac{\rho v_{\parallel}\omega^{\chi}}{B_v^2}\nabla\chi\times\vec{B}\right)$$
$$+B_v\left[\frac{\rho\omega^{\chi}}{B_v^2},\zeta\right]-B_v\left[\frac{P}{B_v^2},\Phi\right]-B_v\left[Pv_{\parallel},\Psi\right]+B_v\left[\frac{Pv_{\parallel}\partial^{\parallel}\Omega}{B_v},\psi_v\right]$$
$$-\nabla\cdot\left(P\nabla^{\perp}\zeta+\frac{B^{\chi}}{B_v^2}\nabla\chi\times\vec{j}-\frac{j^{\chi}}{B_v^2}\nabla\chi\times\vec{B}\right)-\Delta^{\perp}p+\nabla\cdot(\mu_{\zeta}\nabla^{\perp}\Delta^{\perp}\zeta).\tag{2.32}$$

This concludes the derivation of scalar evolution equations for the new set of MHD variables $\{\rho,p,\Phi,v_{\parallel},\zeta,\Psi,\Omega\}$. It should be stressed that, since any magnetic field and velocity can be represented by the ansatzes (2.2) and (2.3), the equations derived in this section are still full MHD; the reduction is done in section 2.5.

2.4 Derivation of an alternate set of equations

In the previous section, the projection operators (2.27) were used to get the scalar evolution equations for the velocity variables. There is another set of projection operators, namely (2.4), which can also be applied to the momentum equation.

Unlike the projection operators (2.27), each of the operators (2.4) is orthogonal to all but one term in the velocity ansatz (2.3). Following Ref [30], where the alternate set of equations was first derived, the momentum equation will be divided by ρ before applying the projection operators (2.4). As will be shown in section 2.6, the alternate set of equations obtained using the projection operators (2.4) does not guarantee conservation of energy in the context of reduced MHD like the equations derived in the previous section, however the reduction introduces less error into momentum conservation when using the alternate equations.

As a first step, it is convenient to apply the sub-operator $\nabla\chi\times(\vec{e}_\chi\times$ to equation (2.28), after dividing by ρ, which results in

$$\begin{aligned}
&-\nabla\frac{\partial\Phi}{\partial t}\times\frac{\nabla\chi}{B_v^2}-v_\parallel\nabla\frac{\partial\Psi}{\partial t}\times\nabla\chi-v_\parallel\nabla\frac{\partial\Omega}{\partial t}\times\nabla\psi_v+\vec{e}_\chi v_\parallel B_v\left[\frac{\partial\Omega}{\partial t},\psi_v\right]-\nabla^\perp\frac{\partial\zeta}{\partial t}\\
&=\frac{1}{2}\nabla v^2-\vec{e}_\chi\frac{B_v}{2}\partial^\parallel v^2+\left(\frac{\nabla\Phi\times\nabla\chi}{B_v^2}+\nabla^\perp\zeta\right)\frac{P}{\rho}-v_\chi\nabla\chi\times\vec{\omega}+\omega_\chi\nabla\chi\times\vec{v}\\
&+\frac{B^2}{\rho B^\chi}\nabla\chi\times\vec{j}-\frac{j_\chi}{\rho}\nabla\chi\times\vec{B}+\frac{\nabla p-\vec{e}_\chi B_v\partial^\parallel p}{\rho}.
\end{aligned}\tag{2.33}$$

From here, the alternate equation for Φ is obtained by applying $\nabla\chi\cdot(\nabla\times$, the remainder of the first projection operator in (2.4), or its equivalent, $-\nabla\cdot(\nabla\chi\times$, to each term in equation (2.33):

$$\begin{aligned}
&\Delta^\perp\frac{\partial\Phi}{\partial t}+\left(v_\parallel B_v^2,\frac{\partial\Psi}{\partial t}\right)+v_\parallel B_v^2\Delta^\perp\frac{\partial\Psi}{\partial t}-\frac{v_\parallel B_v^2}{B_v+[\Omega,\psi_v]}\left[\frac{\partial\Omega}{\partial t},\psi_v\right]\Delta^\perp\Psi-v_\parallel B_v\partial^\parallel\frac{\partial\Omega}{\partial t}\Delta\psi_v\\
&-\left(\frac{v_\parallel B_v^2}{B_v+[\Omega,\psi_v]}\left[\frac{\partial\Omega}{\partial t},\psi_v\right],\Psi\right)-F_v\partial_{\psi_v}\left(v_\parallel B_v\partial^\parallel\frac{\partial\Omega}{\partial t}\right)+\frac{v_\parallel B_v\partial^\parallel\Omega}{B_v+[\Omega,\psi_v]}\left[\frac{\partial\Omega}{\partial t},\psi_v\right]\Delta\psi_v\\
&+F_v\partial_{\psi_v}\left(\frac{v_\parallel B_v\partial^\parallel\Omega}{B_v+[\Omega,\psi_v]}\left[\frac{\partial\Omega}{\partial t},\psi_v\right]\right)=\nabla\cdot\left[\frac{B_v\nabla^\perp\Psi-\partial^\parallel\Omega\nabla\psi_v}{B_v+[\Omega,\psi_v]}\frac{B_v\partial^\parallel v^2}{2}\right.\\
&+\omega_\chi(\nabla\Phi\times\nabla\chi+B_v^2v_\parallel\vec{B}^\perp+B_v^2\nabla^\perp\zeta)-v_\chi B_v^2\vec{\omega}^\perp+\frac{B^2B_v}{\rho(B_v+[\Omega,\psi_v])}\vec{j}^\perp-\frac{j_\chi B_v^2}{\rho}\vec{B}^\perp\\
&\left.-(\nabla^\perp\Phi+\nabla\chi\times\nabla\zeta)\frac{P}{\rho}\right]+B_v\left[\frac{1}{\rho},p\right]+\left(\frac{B_v^2\partial^\parallel p}{\rho(B_v+[\Omega,\psi_v])},\Psi\right)+\frac{B_v^2\partial^\parallel p\Delta^\perp\Psi}{\rho(B_v+[\Omega,\psi_v])}\\
&-F_v\partial_{\psi_v}\left(\frac{B_v\partial^\parallel\Omega\partial^\parallel p}{\rho(B_v+[\Omega,\psi_v])}\right)-\frac{B_v\partial^\parallel\Omega\partial^\parallel p}{\rho(B_v+[\Omega,\psi_v])}\Delta\psi_v+\nu\Delta\Delta^\perp\Phi,
\end{aligned}\tag{2.34}$$

where subscripts indicate covariant vector components: $Q_\chi = \vec{e}_\chi \cdot \vec{Q}$. Just as in the previous section, a generic viscosity term was added to the final equation. Here, ν is the kinematic viscosity and the form of the generic viscosity term was chosen by taking the viscosity term $\rho^{-1}\mu\Delta\vec{v} = \nu\Delta\vec{v}$ in the momentum equation (1.2) and allowing the projection operator to act directly on $\vec{v}$, effectively neglecting its commutator with the operator $\nu\Delta$.

The alternate equation for $v_\parallel$ can be obtained by applying the second projection operator in (2.4) to equation (2.28) and dividing by ρB^χ:

$$\frac{\partial v_\parallel}{\partial t} + \frac{v_\parallel}{B_v + [\Omega, \psi_v]}\left[\frac{\partial \Omega}{\partial t}, \psi_v\right] = -\frac{v_\parallel}{\rho}P + \frac{1}{B_v + [\Omega, \psi_v]}\left[\frac{\vec{\omega}\cdot\nabla^\perp\Phi}{B_v} + B_v v_\parallel \vec{\omega}\cdot\nabla^\perp\Psi \right.$$
$$\left. - v_\parallel\omega^{\psi_v}\partial^\parallel\Omega - \frac{\vec{\omega}\cdot(\nabla\zeta\times\nabla\chi)}{B_v} - \frac{\partial^\parallel v^2}{2} - \frac{B_v\vec{j}\cdot\nabla^\perp\Psi + j^{\psi_v}\partial^\parallel\Omega - \partial^\parallel p}{\rho}\right] + \nu\Delta v_\parallel. \tag{2.35}$$

The alternate equation for ζ is obtained by applying $\nabla\cdot(B_v^2$, the remainder of third projection operator in (2.4), to each term in equation (2.33):

$$B_v^2\Delta^\perp\frac{\partial\zeta}{\partial t} + \left(B_v^2, \frac{\partial\zeta}{\partial t}\right) + B_v\left[v_\parallel B_v^2, \frac{\partial\Psi}{\partial t}\right] - B_v\partial^\parallel\left(\frac{v_\parallel B_v^2}{B_v + [\Omega,\psi_v]}\left[\frac{\partial\Omega}{\partial t}, \psi_v\right]\right)$$
$$- B_v\left[\frac{v_\parallel B_v^2}{B_v + [\Omega,\psi_v]}\left[\frac{\partial\Omega}{\partial t}, \psi_v\right], \Psi\right] - F_v\left[\frac{v_\parallel B_v^2}{B_v + [\Omega,\psi_v]}\left[\frac{\partial\Omega}{\partial t}, \psi_v\right], \Omega\right]_{\psi_v}$$
$$+ F_v\left[v_\parallel B_v^2, \frac{\partial\Omega}{\partial t}\right]_{\psi_v} = \nabla\cdot\left[B_v^2 v_\chi\nabla\chi\times\vec{\omega} - \frac{B_v^2}{2}\nabla v^2 - B_v^2\omega_\chi(\nabla^\perp\Phi + v_\parallel B_v^2\nabla^\perp\Psi\right.$$
$$- v_\parallel B_v\partial^\parallel\Omega\nabla\psi_v + \nabla\chi\times\nabla\zeta) - (\nabla\Phi\times\nabla\chi + B_v^2\nabla^\perp\zeta)\frac{P}{\rho} - \frac{B_v B^2}{\rho(B_v + [\Omega,\psi_v])}\nabla\chi\times\vec{j}$$
$$\left. + \frac{B_v^3 j_\chi}{\rho}(B_v\nabla^\perp\Psi - \partial^\parallel\Omega\nabla\psi_v) + \frac{B_v^2(\nabla\chi + \nabla\Psi\times\nabla\chi + \nabla\Omega\times\nabla\psi_v)\partial^\parallel v^2}{2(B_v + [\Omega,\psi_v])}\right] - \frac{B_v^2}{\rho}\Delta p$$
$$- \nabla\left(\frac{B_v^2}{\rho}\right)\cdot\nabla p + B_v\partial^\parallel\left(\frac{B_v^2\partial^\parallel p}{\rho(B_v + [\Omega,\psi_v])}\right) + B_v\left[\frac{B_v^2\partial^\parallel p}{\rho(B_v + [\Omega,\psi_v])}, \Psi\right]$$
$$+ F_v\left[\frac{B_v^2\partial^\parallel p}{\rho(B_v + [\Omega,\psi_v])}, \Omega\right]_{\psi_v} + \nu B_v^2\Delta\Delta^\perp\zeta. \tag{2.36}$$

Having derived the three alternate equations for the velocity variables, equations (2.21), (2.22), (2.25) and (2.26) can simply be carried over from the main model,

completing the alternate model.

2.5 Reduction of the MHD models

Having derived two different sets of equations for the variables $\{\rho, p, \Phi, v_\parallel, \zeta, \Psi, \Omega\}$ in the previous two sections, the next step is to reduce them. The reduction procedure is straightforward: since fast magnetosonic waves are contained in the last term of the velocity ansatz (2.3), as was shown in section 2.2, they are eliminated by setting $\zeta = 0$ in all of the equations. However, since neither equation (2.32) nor equation (2.36) have $\zeta = 0$ as a trivial solution, the ζ evolution equations must be dropped in both the main model and the alternate model to avoid having an overconstrained system of equations. In addition, since the first two terms of the velocity ansatz do not compress the magnetic field, as was discussed in section 2.2, one should also set $\Omega = 0$ and drop equation (2.26). However, as will be shown in the next section, dropping the Ω equation requires one to also neglect $\vec{j}^\perp$, the component of the current perpendicular to $\nabla\chi$, in equation (2.25) in order to maintain energy conservation. Even though the reduced alternate model does not guarantee energy conservation, $\vec{j}^\perp$ will be neglected in it as well, in order to eliminate an extra source of energy non-conservation.

Note that, unlike in the reduced tokamak model presented in section 1.3.2, the equilibrium Ψ is not, in general, a flux function in the reduced stellarator model:

$$(\vec{B} \cdot \nabla\Psi)|_{t=0} = B_v \partial^\parallel \Psi \neq 0.$$

Since stellarators, unlike tokamaks, do not have a symmetry in the $\nabla\chi$ direction.

For clarity, the reduced equations will be shown here explicitly. The continuity equation (2.21), internal energy equation (2.22) and Ψ equation (2.25), which are the same in both the main model and alternate model, reduce to the following form:

$$\frac{\partial \rho}{\partial t} = -B_v \left[\frac{\rho}{B_v^2}, \Phi\right] - B_v \partial^\parallel(\rho v_\parallel) - B_v[\rho v_\parallel, \Psi] + P, \tag{2.37}$$

$$\frac{\partial p}{\partial t} = -\frac{1}{B_v}\left[p,\Phi\right] - v_\parallel B_v \partial^\parallel p - v_\parallel B_v \left[p,\Psi\right] - \gamma p B_v \left[\frac{1}{B_v^2},\Phi\right] - \gamma p B_v \partial^\parallel v_\parallel - \gamma p B_v \left[v_\parallel,\Psi\right]$$
$$+ \nabla\cdot\left[(\gamma-1)\frac{\kappa_\perp}{R}\nabla\left(\frac{p}{\rho}\right) + (\gamma-1)\frac{\kappa_\parallel-\kappa_\perp}{RB^2}\vec{B}\left(B_v\partial^\parallel\left(\frac{p}{\rho}\right) + B_v\left[\frac{p}{\rho},\Psi\right]\right)\right.$$
$$\left. + \frac{pD_\perp}{\rho}\left(\nabla\rho - \frac{\vec{B}}{B^2}(B_v\partial^\parallel\rho + B_v[\rho,\Psi])\right)\right] + (\gamma-1)(S_e + \eta j^2), \tag{2.38}$$

$$\left[\psi_v, \frac{\partial\Psi}{\partial t}\right] = \left[\frac{[\Psi,\Phi]-\partial^\parallel\Phi}{B_v},\psi_v\right] + \frac{1}{B_v}\nabla\cdot(\eta\nabla\psi_v\times\vec{j}^\parallel), \tag{2.39}$$

where

$$P = \nabla\cdot\left[D_\perp\nabla\rho - \frac{D_\perp\vec{B}}{B^2}(B_v\partial^\parallel\rho + B_v[\rho,\Psi])\right] + S_\rho,$$
$$\vec{j} = \frac{1}{\mu_0}[-\nabla\chi\Delta\Psi + B_v\partial^\parallel\nabla\Psi - (\nabla\Psi\cdot\nabla)\nabla\chi], \tag{2.40}$$
$$\vec{\omega} = -\nabla\chi\nabla\cdot\left(\frac{\nabla\Phi}{B_v^2}\right) + B_v\partial^\parallel\frac{\nabla\Phi}{B_v^2} - \frac{1}{B_v^2}(\nabla\Phi\cdot\nabla)\nabla\chi + \nabla v_\parallel\times\vec{B} + \mu_0 v_\parallel\vec{j}.$$

Reduction of the equations for the velocity variables in the main model leads to

$$\nabla\cdot\left[\frac{\rho}{B_v^2}\nabla^\perp\frac{\partial\Phi}{\partial t} + \rho\frac{\partial}{\partial t}(v_\parallel\nabla^\perp\Psi)\right] = \frac{B_v}{2}\left[\frac{\rho}{B_v^2},v^2\right] + B_v\left[\frac{\rho\omega^\chi}{B_v^4},\Phi\right] - \nabla\cdot(\rho v_\parallel\vec{\omega}^\perp)$$
$$+ B_v\left[\frac{\rho v_\parallel\omega^\chi}{B_v^2},\Psi\right] - \nabla\cdot\left(\frac{P}{B_v^2}\nabla^\perp\Phi + Pv_\parallel\nabla^\perp\Psi\right) - \nabla\cdot\left(\frac{j^\chi}{B_v^2}\vec{B}\right) + B_v\left[\frac{1}{B_v^2},p\right]$$
$$+ \nabla\cdot(\mu_\perp\nabla^\perp\Delta^\perp\Phi), \tag{2.41}$$

$$\rho\left(\frac{\partial\Phi}{\partial t},\Psi\right) + \rho B^2\frac{\partial v_\parallel}{\partial t} + \frac{\rho v_\parallel}{2}\frac{\partial B^2}{\partial t} = -\frac{\rho B_v}{2}\partial^\parallel v^2 - \frac{\rho B_v}{2}\left[v^2,\Psi\right] - \frac{\rho\omega^\chi}{B_v}\partial^\parallel\Phi$$
$$- \frac{\rho\omega^\chi}{B_v}\left[\Phi,\Psi\right] + \rho\vec{\omega}\cdot\nabla\Phi - \vec{v}\cdot\vec{B}\ P - B_v\partial^\parallel p - B_v\left[p,\Psi\right] + \nabla\cdot(\mu_\parallel\nabla^\perp v_\parallel), \tag{2.42}$$

whereas in the alternate model, the reduced equations for Φ and $v_\parallel$ are

$$\Delta^\perp\frac{\partial\Phi}{\partial t} + \left(v_\parallel B_v^2, \frac{\partial\Psi}{\partial t}\right) + v_\parallel B_v^2\Delta^\perp\frac{\partial\Psi}{\partial t} = \nabla\cdot\left[\frac{B_v\partial^\parallel v^2}{2}\nabla^\perp\Psi\right.$$
$$+ \omega_\chi(\nabla\Phi\times\nabla\chi + B_v^2 v_\parallel\nabla\Psi\times\nabla\chi) - v_\chi B_v^2\vec{\omega}^\perp + \frac{B^2}{\rho}\vec{j}^\perp - \frac{j_\chi B_v^2}{\rho}\nabla\Phi\times\nabla\chi \tag{2.43}$$
$$\left. - \nabla^\perp\Phi\frac{P}{\rho}\right] + B_v\left[\frac{1}{\rho},p\right] + \left(\frac{B_v\partial^\parallel p}{\rho},\Psi\right) + \frac{B_v\partial^\parallel p\Delta^\perp\Psi}{\rho} + \nu\Delta\Delta^\perp\Phi,$$

$$\frac{\partial v_\parallel}{\partial t} = -\frac{v_\parallel}{\rho}P + \frac{1}{B_v}\left[\frac{\vec{\omega}\cdot\nabla^\perp\Phi}{B_v} + B_v v_\parallel \vec{\omega}\cdot\nabla^\perp\Psi - \frac{\partial^\parallel v^2}{2} - \frac{B_v\vec{j}\cdot\nabla^\perp\Psi - \partial^\parallel p}{\rho}\right] + \nu\Delta v_\parallel. \tag{2.44}$$

A further reduction, applicable to both the main and alternate models, could be carried out by setting $v_\parallel = 0$ and dropping the $v_\parallel$ equation. These reduced models without parallel flows will be used extensively in the next chapters.

Note that the reduced Ψ equation (2.39) can expressed in a simpler form. Indeed, equation (2.39) can be rewritten as

$$\nabla\psi_v\cdot\nabla\times\left(\frac{\partial\Psi}{\partial t}\nabla\chi\right) = \nabla\psi_v\cdot\nabla\times\left(\frac{\partial^\parallel\Phi - [\Psi,\Phi]}{B_v}\nabla\chi - \eta\frac{j^\chi}{B_v^2}\nabla\chi\right).$$

Since all of the terms under the curl both on the LHS and the RHS only have components in the $\nabla\chi$ direction, the above equation will be satisfied as long as the following equation is satisfied:

$$B_v\frac{\partial\Psi}{\partial t} = \partial^\parallel\Phi - [\Psi,\Phi] - \eta\frac{j^\chi}{B_v} \tag{2.45}$$

This equation does not involve ψ_v and, as will be shown in the next chapter, tends to be more numerically stable.

In closing, it will be shown that in reduced ideal MHD, the velocity stream function Φ is equal to the negative electric potential, up to an additive constant. Faraday's law can be written in potental form:

$$\frac{\partial\vec{A}}{\partial t} = -\vec{E} - \nabla V,$$

where V is the electric potential and $\vec{A}$ is the magnetic vector potential. Substituting the ideal Ohm's law $\vec{E} = -\vec{v}\times\vec{B}$ into the above equation and using the ansatzes (2.2), (2.3) with $\Omega = 0$ and $\zeta = 0$, the equation becomes

$$\frac{\partial\Psi}{\partial t}\nabla\chi = -\nabla^\perp\Phi - \frac{\nabla\chi}{B_v}[\Psi,\Phi] - \nabla V.$$

One can get that $\partial\vec{A}/\partial t = \partial\Psi/\partial t\nabla\chi$ by first taking the time derivative of $\vec{B} = \nabla\chi + \nabla\Psi\times\nabla\chi$ and then un-curling the result. The components of the above equation perpendicular to $\nabla\chi$ read $\nabla^\perp\Phi = -\nabla^\perp V$, which requires that $\Phi = -V + c(\chi)$, where c is an arbitrary function of χ. The component along $\nabla\chi$ reads

$$\frac{\partial\Psi}{\partial t}\nabla\chi = (\partial^\parallel\Phi - c' - [\Psi,\Phi])\frac{\nabla\chi}{B_v},$$

where V was replaced by $-\Phi+c(\chi)$. This equation matches (2.45) exactly if $c'=0$. Thus, c is an additive constant and $\Phi=-V+c$.

2.6 Conservation properties of the reduced MHD models

Having derived the main and alternate reduced MHD models, the conservation of energy, flux and momentum in both models will now be considered. Mass is conserved exactly, due to the continuity equation being used directly to evolve density in both models.

2.6.1 Conservation of energy

As was mentioned previously, the main model conserves energy. This can be proven as follows. Applying the first projection operator in (2.27) to some vector function $\vec{Q}$, multiplying the result by an arbitrary test function Φ^*, and then integrating over the plasma volume V, the following expression can be obtained:

$$\int_V \Phi^* \nabla\chi\cdot\nabla\times\left(\frac{\vec{Q}}{B_v^2}\right)dV=\int_V \frac{\nabla\Phi^*\times\nabla\chi}{B_v^2}\cdot\vec{Q}\,dV, \tag{2.46}$$

where the identity $\nabla f\cdot\nabla\times\vec{U}=-\nabla\cdot(\nabla f\times\vec{U})$ was used, along with integration by parts. It is assumed that $\Phi^*=0$ on ∂V, making the surface integral term is zero. Similarly, for the third projection operator in (2.27) and test function ζ^*, one gets

$$\int_V \zeta^*\nabla\chi\cdot\nabla\times\left(\frac{\nabla\chi\times\vec{Q}}{B_v^2}\right)dV=-\int_V\frac{\nabla\zeta^*}{B_v^2}\cdot[\nabla\chi\times(\vec{Q}\times\nabla\chi)]dV=-\int_V\nabla^\perp\zeta^*\cdot\vec{Q}\,dV, \tag{2.47}$$

also with $\zeta^*=0$ on ∂V. Finally, applying the second projection operator in (2.27) to $\vec{Q}$, multiplying by a test function $v_\parallel^*$ and integrating, one has

$$\int_V v_\parallel^*\vec{B}\cdot\vec{Q}dV=\int_V v_\parallel^*\vec{B}\cdot\vec{Q}dV. \tag{2.48}$$

Now, let $\vec{Q}$ be the momentum equation in (1.2) without the viscosity term: $\vec{Q}\equiv\rho\partial\vec{v}/\partial t+\rho(\vec{v}\cdot\nabla)\vec{v}+\vec{v}P-\vec{j}\times\vec{B}+\nabla p$. Note that $\vec{Q}$ is not set to zero, as this derivation must be applicable also to reduced MHD, where the vector momentum equation of full MHD is not satisfied. Letting $\Phi^*=\Phi$, $v_\parallel^*=v_\parallel$ and $\zeta^*=-\zeta$, it

follows from equations (2.46)–(2.48) and (2.30)–(2.32) that

$$0 = \int_V \vec{v} \cdot \left[\rho \frac{\partial \vec{v}}{\partial t} + \rho(\vec{v} \cdot \nabla)\vec{v} + \vec{v}P - \vec{j} \times \vec{B} + \nabla p \right] dV. \tag{2.49}$$

The important point to note here is that equation (2.49) continues to hold even in reduced MHD. Indeed, setting $\zeta = 0$ makes equation (2.47) reduce to $0 = 0$ and equation (2.32) is no longer needed in order for equation (2.49) to be satisfied. Thus, equation (2.32) can be dropped. Similarly, setting $v_\parallel = 0$ allows equation (2.31) to be dropped while equation (2.49) continues to be satisfied. Finally, using the continuity equation, equation (2.49) can be rewritten as

$$\int_V \left[\frac{\partial}{\partial t} \left(\frac{\rho v^2}{2} \right) + \nabla \cdot \left(\frac{\rho v^2}{2} \vec{v} \right) \right] dV = \int_V \left[\vec{v} \cdot (\vec{j} \times \vec{B}) - \vec{v} \cdot \nabla p - \frac{v^2}{2} P \right] dV, \tag{2.50}$$

which is the kinetic energy equation.

Consider now the magnetic field equations. When both Ψ and Ω terms are present in the magnetic field ansatz, both equations (2.25) and (2.26) are satisfied, which means that Faraday's law in (1.2) is also satisfied, since the Ψ and Ω equations are just two vector components of Faraday's law. Only two equations are needed to evolve the full magnetic field, since the third degree of freedom is eliminated by the $\nabla \cdot \vec{B} = 0$ constraint. In the reduced MHD case, when the Ω term is removed from the magnetic field ansatz, Faraday's law continues to be satisfied. This can be shown by multiplying equation (2.45) by $\nabla\chi/B_v$ and taking the curl. Thus, the magnetic energy equation can be derived from Faraday's law by dotting with $\vec{B}$ and following the usual procedure:

$$\frac{1}{2\mu_0} \frac{\partial B^2}{\partial t} + \frac{1}{\mu_0} \nabla \cdot (\vec{E} \times \vec{B}) = -\vec{v} \cdot (\vec{j} \times \vec{B}) - \eta (j^*)^2, \tag{2.51}$$

where $j^* = j$ in the full MHD case and $j^* = j^\parallel$ in the reduced MHD case, when the component of current perpendicular to $\nabla\chi$ must be dropped.

Finally, the total energy equation is obtained by putting together the three energy equations. Dividing the internal energy equation (1.2) by $\gamma - 1$, then integrating both that and the magnetic energy equation (2.51) over the plasma volume V and adding up the two resulting equations with the kinetic energy equation (2.50), the

following is obtained:

$$\int_V \left[\frac{\partial}{\partial t}\left(\frac{\rho v^2}{2} + \frac{p}{\gamma - 1} + \frac{B^2}{2\mu_0} \right) + \nabla \cdot \left(\frac{\rho v^2}{2}\vec{v} + \frac{\gamma p}{\gamma - 1}\vec{v} + \frac{\vec{E} \times \vec{B}}{\mu_0} \right.\right.$$
$$\left.\left. - \kappa_\perp \nabla_\perp T - \kappa_\parallel \nabla_\parallel T - \frac{p}{\gamma - 1}\frac{D_\perp}{\rho}\nabla_\perp \rho \right) \right] dV = \int_V \left(S_e - \frac{v^2}{2}P \right) dV.$$

The above equation can be rewritten as

$$\frac{dE}{dt} = \oint_{\partial V} \left(\kappa_\perp \nabla_\perp T + \frac{RT}{\gamma - 1} D_\perp \nabla_\perp \rho \right) \cdot d\vec{S} + \int_V \left(S_e - \frac{v^2}{2}P \right) dV, \tag{2.52}$$

where the boundary conditions $\vec{n} \cdot \vec{v} = 0$ and $\vec{n} \cdot \vec{B} = 0$ have been applied.

Having considered energy conservation in the main reduced model, the necessity of dropping the perpendicular current in Ohm's law can now be demonstrated. Suppose that Ψ_1 and Ψ_2 satisfy the equations

$$\left[\psi_v, \frac{\partial \Psi_1}{\partial t} \right] = \left[\frac{[\Psi, \Phi] - \partial^\parallel \Phi}{B_v}, \psi_v \right] + \frac{1}{B_v} \nabla \cdot (\eta \nabla \psi_v \times \vec{j}^\parallel),$$
$$\left[\psi_v, \frac{\partial \Psi_2}{\partial t} \right] = \frac{1}{B_v} \nabla \cdot (\eta \nabla \psi_v \times \vec{j}^\perp),$$

then clearly $\Psi = \Psi_1 + \Psi_2$ will satisfy equation (2.25) with $\Omega = 0$ but without neglecting $\vec{j}^\perp$ in the last term. With the same reasoning that was used to argue that Faraday's law is satisfied in reduced MHD, it can be shown that the Ψ_1 equation above is equivalent to $\partial \vec{B}_1 / \partial t = -\nabla \times \vec{E}_1$, where $\vec{B}_1 = \nabla \chi + \nabla \Psi_1 \times \nabla \chi$ and $\vec{E}_1 = -\vec{v} \times \vec{B} + \eta \vec{j}^\parallel$. Dotting the Faraday's-law-like equation for $\vec{B}_1$ with $\vec{B} = \vec{B}_1 + \vec{B}_2$ and adding $\vec{B} \cdot \partial \vec{B}_2 / \partial t + \nabla \cdot (\vec{E}_2 \times \vec{B})$ to both sides, where $\vec{B}_2 = \nabla \Psi_2 \times \nabla \chi$ and $\vec{E}_2 = \eta \vec{j}^\perp$, the following equation is obtained:

$$\frac{1}{2}\frac{\partial B^2}{\partial t} + \nabla \cdot (\vec{E} \times \vec{B}) = \mu_0 [(\vec{v} \times \vec{B}) \cdot \vec{j} - \eta j^2] + \vec{B} \cdot \frac{\partial \vec{B}_2}{\partial t} + \vec{B} \cdot \nabla \times \vec{E}_2.$$

The Ψ_2 equation is equivalent to $(\partial \vec{B}_2 / \partial t)^{\psi_v} = -(\nabla \times \vec{E}_2)^{\psi_v}$. Thus, if the dot products in the last two terms of the above equation are expanded, only the terms involving the ψ_v components can be cancelled; the nonconservative terms $B_{\beta_v} \partial B_2^{\beta_v} / \partial t + B_{\beta_v} (\nabla \times \vec{E}_2)^{\beta_v} + (\nabla \times \vec{E}_2)^\chi$ still remain.

To conclude this subsection, it will be shown why non-conservation of energy is possible in the alternate reduced MHD model. The velocity field can be written

using a covariant ansatz:

$$\vec{v} = B_v^2 \nabla^\perp \widetilde{\Phi} \times \vec{e}_\chi + \widetilde{v_\parallel} \nabla\chi + B_v^2 \vec{e}_\chi \times (\nabla\widetilde{\zeta} \times \nabla\chi), \tag{2.53}$$

as opposed to the contravariant ansatz (2.3). This can be shown by applying the projection operators (2.27) to the covariant ansatz (2.53), which results in the following equations:

$$\begin{gathered} \nabla\chi \cdot \nabla \times \left(\frac{1}{B_v^2} \vec{v} \right) = -\nabla \cdot (\nabla^\perp \widetilde{\Phi}), \\ \vec{B} \cdot \vec{v} = B^\chi \widetilde{v_\parallel}, \\ \nabla\chi \cdot \nabla \times \left(\frac{1}{B_v^2} \nabla\chi \times \vec{v} \right) = \nabla \cdot (B_v^2 \nabla^\perp \widetilde{\zeta}). \end{gathered} \tag{2.54}$$

Similarly to how each of the projection operators (2.4) was orthogonal to all but one term in the contravariant velocity ansatz (2.3), each of the projection operators (2.27) is orthogonal to all but one term in the covariant velocity ansatz (2.53). Using the above equations, one can see that any velocity can be represented with the covariant ansatz by following the same steps as in section 2.1.

Now, following the same steps as in the beginning of this subsection, apply the first projection operator in (2.4) to a vector function $\vec{Q}$, multiply by an arbitrary test function Φ^* and integrate over the plasma volume V, resulting, after integration by parts, in

$$\int_V \Phi^* \nabla\chi \cdot \nabla \times [\nabla\chi \times (\vec{e}_\chi \times \vec{Q})] dV = -\int_V B_v^2 (\nabla^\perp \Phi^* \times \vec{e}_\chi) \cdot \vec{Q} dV. \tag{2.55}$$

Doing the same for the third projection operator in (2.4) and test function ζ^* gives

$$\int_V \zeta^* \nabla \cdot [B_v^2 \nabla\chi \times (\vec{e}_\chi \times \vec{Q})] dV = \int_V B_v^2 [\vec{e}_\chi \times (\nabla\zeta^* \times \nabla\chi)] \cdot \vec{Q} dV. \tag{2.56}$$

Just as before, no transformations are needed for the second projection operator in (2.4):

$$\int_V v_\parallel^* \nabla\chi \cdot \vec{Q} dV = \int_V v_\parallel^* \nabla\chi \cdot \vec{Q} dV. \tag{2.57}$$

Setting $\vec{Q} \equiv \partial\vec{v}/\partial t + (\vec{v}\cdot\nabla)\vec{v} + \vec{v}P/\rho - \vec{j} \times \vec{B}/\rho + \nabla p/\rho$, one needs $\Phi^* = -\widetilde{\Phi}$, $v_\parallel^* = \widetilde{v_\parallel}$, $\zeta^* = \widetilde{\zeta}$ and $\rho = \text{const}$ in order for the kinetic energy equation, $\int_V \rho\vec{v}\cdot\vec{Q} dV = 0$, to be satisfied. The first three of these conditions are satisfied in full MHD, however $\zeta = 0$ does not imply that $\widetilde{\zeta} = 0$, and so equation (2.56) does not reduce to $0 = 0$, unlike

equation (2.47) in the main model. Thus, since equation (2.36) must be dropped, equation (2.56) is no longer satisfied in the alternate reduced model, which means that the kinetic energy equation also cannot be satisfied. Also, due to the vector momentum equation being divided by ρ before applying the projection operators in the derivation of the alternate model, the density must be spatially constant in order for the kinetic energy equation to be satisfied, even in the full MHD case. Therefore, both the reduction and nonzero density gradients can lead to violations of energy conservation in the alternate model.

2.6.2 Conservation of flux

To begin with, consider the full MHD case. It can be shown that flux is not conserved for finite resistivity by following the same steps as Ref [3] did to prove conservation in the ideal case. Let $S(t_0)$ be an arbitrary surface anywhere in the plasma at time t_0. Then, $S(t)$ is obtained by letting the surface be advected with the plasma, while using $S(t_0)$ as an initial condition. At any time t, the magnetic flux through $S(t)$ is defined as

$$\psi = \int_{S(t)} \vec{B} \cdot d\vec{S}. \tag{2.58}$$

Differentiating the above equation with respect to time, and then using Faraday's law and Ohm's law (1.2), as well as Stokes' theorem, the following equation can be obtained:

$$\frac{d\psi}{dt} = \int_{S(t)} \frac{\partial \vec{B}}{\partial t} \cdot d\vec{S} + \oint_{\partial S(t)} \vec{B} \cdot (\vec{v} \times d\vec{l}) = -\oint_{\partial S(t)} \eta \vec{j} \cdot d\vec{l}. \tag{2.59}$$

This equation gives the physical non-conservation of flux due to finite resistivity. In reduced MHD, one must replace $\vec{j}$ by $\vec{j}^{\parallel}$; all of the other steps above are still valid, since Faraday's law and Ohm's law continue to hold in reduced MHD if the perpendicular current is dropped. Thus, in the ideal case, flux will be exactly conserved and the magnetic field will be frozen into the plasma even in the reduced MHD model. Alternatively, one can think of it as follows. Note that in reduced

MHD, when $\zeta = 0$ and $\Omega = 0$, equation (2.26) becomes

$$0 = \nabla \cdot (\eta \nabla \chi \times \vec{j}).$$

If $\eta = 0$, this equation will be satisfied exactly, reducing to $0 = 0$. Thus, in the ideal scenario, the Ω evolution equation is not dropped, but rather trivially satisfied. Therefore, in the ideal case, no part of the original Faraday's and Ohm's laws (1.2) are neglected.

2.6.3 Approximate conservation of momentum

In general, reduced MHD models do not conserve momentum, except for some special cases. The fact that momentum cannot be conserved locally becomes obvious when one considers that there are only two velocity variables in reduced MHD, namely Φ and $v_\parallel$, and so all three components of the momentum equation in (1.2) cannot be satisfied simultaneously. In this subsection, the amount of momentum conservation error introduced by the reduction will be considered in both the main and alternate models.

To begin with, consider the alternate model. Applying the first projection operator in (2.4) to an arbitrary vector function $\vec{Q}$, one can see that $\nabla\chi \cdot \nabla \times [\nabla\chi \times (\vec{e}_\chi \times \vec{Q})] = \nabla\chi \cdot \nabla \times (\vec{e}_\chi Q^\chi - \vec{Q})$. Now let $\vec{Q} \equiv \rho \partial \vec{v}/\partial t + \rho(\vec{v}\cdot\nabla)\vec{v} + \vec{v}P - \vec{j} \times \vec{B} + \nabla p = 0$ be the momentum equation in (1.2) without the viscosity term. Then, equation (2.34) is just the component of the vorticity-like equation $\nabla \times (\vec{e}_\chi Q^\chi - \vec{Q})$ along $\nabla\chi$. If all three components of this vorticity-like equation were satisfied, then the original momentum equation in (1.2) would also be satisfied; the reduction corresponds to dropping the two components of this vorticity-like equation that are perpendicular to $\nabla\chi$. The magnitude of the terms in these perpendicular components relative to the terms in the component that is kept can help to estimate the magnitude of the

momentum conservation error. The vorticity-like equation is as follows:

$$\begin{aligned}
&\frac{\partial\vec{\varpi}}{\partial t}+\mu_0 v_\parallel\frac{\partial\vec{j}}{\partial t}+\nabla v_\parallel\times\frac{\partial\vec{B}}{\partial t}-\frac{\mu_0\vec{j}}{B_v}\partial^\parallel v^2-\nabla\left(\frac{\partial^\parallel v^2}{B_v}\right)\times\vec{B}+\nabla\times(\vec{\omega}\times\vec{v})\\
&-\frac{\mu_0\vec{j}}{B_v^2}\nabla\chi\cdot(\vec{\omega}\times\vec{v})-\nabla\left[\frac{\nabla\chi\cdot(\vec{\omega}\times\vec{v})}{B_v^2}\right]\times\vec{B}+\vec{\varpi}\,\frac{P}{\rho}+\nabla\left(\frac{P}{\rho}\right)\times\vec{v}=\frac{\vec{B}}{\rho^2}(\vec{j}\cdot\nabla\rho)\\
&-\frac{\vec{j}}{\rho^2}(\vec{B}\cdot\nabla\rho)+\frac{1}{\rho}(\vec{B}\cdot\nabla)\vec{j}-\frac{1}{\rho}(\vec{j}\cdot\nabla)\vec{B}-\frac{\vec{j}}{\rho B_v^2}\nabla\chi\cdot(\vec{j}\times\vec{B})\\
&-\nabla\left[\frac{\nabla\chi\cdot(\vec{j}\times\vec{B})}{\rho B_v^2}\right]\times\vec{B}+\frac{1}{\rho^2}\nabla\rho\times\nabla p+\frac{\vec{j}}{\rho B_v}\partial^\parallel p+\nabla\left(\frac{\partial^\parallel p}{\rho B_v}\right)\times\vec{B},
\end{aligned}\tag{2.60}$$

where $\vec{v}=-\nabla\chi\times(\vec{e}_\chi\times\vec{v})=\nabla\Phi\times\nabla\chi/B_v^2$ is the reduced velocity and $\vec{\varpi}=\nabla\times\vec{v}$ is the reduced vorticity. If all terms in the perpendicular components of equation (2.60) vanish, then there is no error introduced by the reduction, and momentum will be conserved exactly. The most general situation in which this is the case is when the following condition is satisfied:

$$\partial^\parallel u=0,\qquad u\in\{g^{ik},\Phi,\Psi,v_\parallel,p,\rho,P\}\tag{2.61}$$

where g^{ik} is the metric tensor for the Clebsch-type coordinate system (ψ_v,β_v,χ) aligned to the vacuum field $\nabla\chi$. It can be easily seen that $\vec{\varpi}$ and $\vec{j}$ are colinear with $\nabla\chi$. However, if at least one of the variables g^{ik}, Φ or Ψ has a nonzero parallel derivative, $\vec{\varpi}$ will gain a perpendicular component, and so $\partial\vec{\varpi}/\partial t$ will have perpendicular components which cannot be cancelled by any other term as there are no other terms with time derivatives of Φ in the equation. One can further see that allowing $\partial^\parallel p\neq 0$ leads to the last and seventh terms on the RHS gaining perpendicular components, $\partial^\parallel\rho\neq 0$ leads to the first and seventh terms on the RHS gaining perpendicular components, $\partial^\parallel P\neq 0$ leads to the last term on the LHS gaining perpendicular components, and $\partial^\parallel v_\parallel\neq 0$ leads to the third term on the LHS gaining perpendicular components. None of these terms' perpendicular components can be cancelled by any other terms. On the other hand, if the condition (2.61) is satisfied, only the sixth and eighth terms on the LHS will have perpendicular

components. After some algebra, one can see that

$$[\nabla \times (\vec{\omega} \times \vec{v})]^{\perp} - \left[\nabla \left[\frac{\nabla\chi \cdot (\vec{\omega} \times \vec{v})}{B_v^2}\right] \times \vec{B}\right]^{\perp} \equiv 0.$$

The condition (2.61) is quite restrictive and cannot be satisfied for most simulations. However, as long as $|\partial^{\parallel} u| \ll |\nabla^{\perp} u|$, the momentum conservation error should not be too large.

Now, the main reduced model will be considered in contrast. The first projection operator in (2.27) applied to $\vec{Q} \equiv \rho\partial\vec{v}/\partial t + \rho(\vec{v}\cdot\nabla)\vec{v} + \vec{v}P - \vec{j} \times \vec{B} + \nabla p = 0$ is $\nabla\chi \cdot \nabla \times (\vec{Q}/B_v^2)$, and so the vorticity-like equation analogous to equation (2.60) will be given by $\nabla \times (\vec{Q}/B_v^2)$. Written out in full, this equation is

$$\begin{aligned}
&\nabla\left(\frac{\rho}{B_v^2}\right) \times \frac{\partial\vec{v}}{\partial t} + \frac{\rho}{B_v^2}\frac{\partial\vec{\omega}}{\partial t} + \nabla\left(\frac{\rho}{B_v^2}\frac{\partial v_{\parallel}}{\partial t}\right) \times \vec{B} + \frac{\mu_0\rho}{B_v^2}\frac{\partial v_{\parallel}}{\partial t}\vec{j} + \nabla\left(\frac{\rho v_{\parallel}}{B_v^2}\right) \times \frac{\partial\vec{B}}{\partial t} \\
&+ \frac{\mu_0\rho v_{\parallel}}{B_v^2}\frac{\partial\vec{j}}{\partial t} + \frac{1}{2}\nabla\left(\frac{\rho}{B_v^2}\right) \times \nabla v^2 + \nabla \times \left(\frac{\rho\vec{\omega} \times \vec{v}}{B_v^2}\right) + \nabla\left(\frac{P}{B_v^2}\right) \times \vec{v} + \frac{P}{B_v^2}\vec{\omega} \\
&+ \nabla\left(\frac{Pv_{\parallel}}{B_v^2}\right) \times \vec{B} + \frac{\mu_0 P v_{\parallel}}{B_v^2}\vec{j} = \frac{2\vec{B}}{B_v^3}\vec{j}\cdot\nabla B_v - \frac{2\vec{j}}{B_v^3}\vec{B}\cdot\nabla B_v + \frac{1}{B_v^2}(\vec{B}\cdot\nabla)\vec{j} \\
&- \frac{1}{B_v^2}(\vec{j}\cdot\nabla)\vec{B} + \frac{2}{B_v^3}\nabla B_v \times \nabla p,
\end{aligned} \tag{2.62}$$

with equation (2.30) being the component of this equation along $\nabla\chi$. Two things should be pointed out here. First, the perpendicular components of the third and eleventh terms on the LHS do not vanish even if condition (2.61) is satisfied. Second, while the eighth term on the LHS in equation (2.62) resembles the sixth term on the LHS in equation (2.60), there is no term to cancel its perpendicular components, as no term resembles the eighth term on the LHS in equation (2.60). However, imposing $v_{\parallel} = 0$ in addition to the condition (2.61) is enough to make the perpendicular components of equation (2.62) zero, as the third and eleventh terms disappear altogether, and the eighth term loses its perpendicular components:

$$\nabla \times \left(\frac{\rho\vec{\omega} \times \vec{v}}{B_v^2}\right) = \nabla \times \left(\frac{\rho\omega_{\chi}\nabla^{\perp}\Phi}{B_v^2}\right) = \nabla\left(\frac{\rho\omega_{\chi}}{B_v^2}\right) \times \nabla^{\perp}\Phi - \frac{\rho\omega_{\chi}}{B_v^2}\nabla\left(\frac{\partial^{\parallel}\Phi}{B_v}\right) \times \nabla\chi.$$

Clearly, when $v_{\parallel} \neq 0$, the alternate model conserves momentum better than the main model. However, since neither model conserves momentum exactly and the

alternate model doesn't conserve energy exactly, most of the simulations in this dissertation will be done with the main model, except for a few test cases in the next chapter, which were done with the alternate model.

2.7 Force balance in an equilibrium

A natural question that arises when considering reduced MHD is whether or not the reduction preserves equilibria. In other words: if a particular equilibrium solution to the full MHD equations is known, will it also be a solution to the reduced MHD equations? A simple argument shows that, when considering a static tokamak equilibrium, this is indeed the case for the main reduced model in the tokamak limit, where it reduces to the standard tokamak model used in JOREK.

Consider the Φ evolution equation (2.41) with $\Phi = v_\parallel = 0$ and $\chi = F_0\phi$; the equation reduces to the following

$$0 = -\frac{1}{F_0}\nabla\cdot(Rj_{\hat{\phi}}\vec{B}) + \frac{1}{F_0 R}[R^2, p] = -\frac{1}{R}\frac{\partial j_{\hat{\phi}}}{\partial\phi} - \frac{1}{R}[Rj_{\hat{\phi}}, \Psi] + \frac{1}{F_0 R}[R^2, p], \quad (2.63)$$

where $j_{\hat{\phi}} = \hat{\phi}\cdot\vec{j}$. The first term on the RHS is zero due to axisymmetry of the tokamak equilibrium. The toroidal current can be written as $j_{\hat{\phi}} = -(F_0\mu_0 R)^{-1}\Delta^*\Psi$, and the Grad-Shafranov equation reads: $\Delta^*\Psi = -\mu_0 R^2 p' - FF'$, where the derivatives are with respect to Ψ (recall that Ψ is a flux function in the tokamak limit) and $\Delta^* = R^2\nabla\cdot(R^{-2}\nabla^\perp$. In addition, since p is a flux function, $\nabla p = p'\nabla\Psi$, and so the Poisson bracket in the last term becomes $p'[R^2, \Psi]$. Inserting the expression for $j_{\hat{\phi}}$ and using the Grad-Shafranov equation, one gets

$$0 = -\frac{p'}{F_0 R}[R^2, \Psi] - \frac{R}{F_0}[p', \Psi] - \frac{1}{F_0\mu_0 R}[FF', \Psi] + \frac{p'}{F_0 R}[R^2, \Psi] \equiv 0, \quad (2.64)$$

where the second and third terms are zero due to p and F being flux functions. The $v_\parallel$ evolution equation (2.42) with $\Phi = v_\parallel = 0$ and $\chi = F_0\phi$ becomes

$$0 = -\frac{F_0}{R^2}\frac{\partial p}{\partial\phi} - \frac{F_0}{R}[p, \Psi] \equiv 0, \quad (2.65)$$

where the first term is zero due to axisymmetry and the second is zero due to p being a flux function.

The above argument does not hold for the alternate model. The next subsection will consider the case of the alternate model and introduce a force balancing term to compensate for the imbalance resulting from the reduction. All simulations with the alternate model, which are presented in the next chapter will use this force balancing term. When using the main model for a stellarator, the above argument also does not hold, however it will be shown in the last subsection that the imbalance is small enough to neglect.

2.7.1 The force balancing term in the alternate model

Consider the momentum equation in (1.2) after inserting the ansatzes with $\zeta = 0$ and $\Omega = 0$, but before applying projection operators. For the sake of clarity, it is better to introduce the force balancing term before applying the projection operators. Strictly speaking, the momentum equation is overconstrained at this point, but only the Φ and $v_{\parallel}$ equations will be kept at the end, as was done in section 2.5. The momentum equation with the force balancing term reads

$$\frac{\partial}{\partial t}(\rho\vec{v}) + \nabla\cdot(\rho\vec{v}\vec{v}) = \vec{j}\times\vec{B} - \nabla p + \rho\nu\Delta\vec{v} + (\vec{j}_f\times\vec{B}_f - \vec{j}\times\vec{B})|_{t=0}, \tag{2.66}$$

where $\vec{B}_f$ and $\vec{j}_f$ are the full MHD magnetic field and current. Assuming that the simulation starts from an equilibrium, at $t = 0$, the two reduced MHD Lorentz force term will cancel while the full MHD Lorentz force will balance the pressure. The first Lorentz force term will then evolve with time while the two in the force balancing term remain frozen. Since the Ω term, which is the difference between full and reduced MHD, corresponds mostly to field compression with its field line bending contribution being small, and most instabilities tend to not compress the magnetic field due to the large amount of energy required, such a force balancing term should not lead to any inaccuracies. For tokamak equilibria, the force balancing term becomes $-FF'\,\nabla\Psi|_{t=0}/R^2$.

It can be shown that the force balancing term in equation (2.66) does not introduce any significant error in the global conservation of momentum. Without

viscosity, equation (2.66) can be expressed as

$$\frac{\partial}{\partial t}(\rho\vec{v})+\nabla\cdot\left[\rho\vec{v}\vec{v}+\left(p+\frac{B^2+(B_f^2-B^2)|_{t=0}}{2\mu_0}\right)\overleftrightarrow{I}-\frac{\vec{B}\vec{B}+(\vec{B}_f\vec{B}_f-\vec{B}\vec{B})|_{t=0}}{\mu_0}\right]=0. \tag{2.67}$$

If $\vec{n}\cdot\vec{B}=\vec{n}\cdot\vec{B}_f=0$, then after integration over the plasma volume, the following equation results

$$\frac{d}{dt}\int_V\rho\vec{v}dV=-\oint_{\partial V}\left(p+\frac{B^2+(B_f^2-B^2)|_{t=0}}{2\mu_0}\right)d\vec{S}. \tag{2.68}$$

The term $(B_f^2-B^2)|_{t=0}/(2\mu_0)$ is approximately the density of the energy due to magnetic field compression in the initial equilibrium (Shafranov shift). Note that in a tokamak equilibrium, $(B_f^2-B^2)|_{t=0}/(2\mu_0)=(F^2-F_0^2)/(2\mu_0R^2)$ is exactly the energy density due to compression. Since instabilities should not affect the compression much, the energy due to compression should be roughly constant, and so $B^2+(B_f^2-B^2)|_{t=0}\approx B_f^2$, where $B_f^2/(2\mu_0)$ is the total magnetic energy density, both due to field line bending and compression.

Finally, it should be pointed out that the force balancing term does not affect the momentum conservation properties of the alternate model, as discussed in section 2.6.3. This can be seen by inserting $p=p|_{t=0}+\widetilde{p}$ in (2.66), with $\widetilde{p}$ being defined as $p-p|_{t=0}$. Then, $\nabla p|_{t=0}$ will cancel with $(\vec{j}_f\times\vec{B}_f)|_{t=0}$, leaving only the $-(\vec{j}\times\vec{B})|_{t=0}$ remaining from the force balancing term. This remaining term is just the reduced MHD Lorentz force term at $t=0$, which was already considered in section 2.6.3 and does not contribute to the perpendicular components of equation (2.60) if the condition (2.61) is satisfied. To be more precise, condition (2.61) when the force balancing term is included should be rewritten as

$$\partial^{\|}u=0,\qquad u\in\{g^{ik},\Phi,\Psi,v_{\|},\widetilde{p},\rho,P\}. \tag{2.69}$$

This modified condition is slightly less restrictive, since now only the pressure perturbation has to be constant along $\nabla\chi$, whereas before both the initial pressure (since the condition also has to be satisfied at $t=0$) and the perturbation had to have zero parallel derivatives.

2.7.2 Force balance in the main model for a general stellarator

In this subsection, an ordering-based argument will be used to show that, when applying the main model to a general stellarator, the force balance error is small enough to neglect. Let $L_\perp$ be the length scale perpendicular to $\nabla\chi$ and $L_\parallel$ be the length scale along $\nabla\chi$. Then, defining $\lambda \equiv L_\perp/L_\parallel$ as the ordering parameter, the spatial derivatives must satisfy $|\partial^\parallel| \sim \lambda|\nabla^\perp|$. The terms in the magnetic field ansatz (2.2) are ordered as follows:

$$\frac{|\nabla\Psi \times \nabla\chi|}{|\nabla\chi|} \sim |\nabla^\perp\Psi| \sim \lambda,$$

and

$$\frac{|\nabla\Omega \times \nabla\psi_v|}{|\nabla\chi|} \sim \frac{F_v}{B_v}|\nabla\Omega| \sim \lambda^2.$$

Identifying $L_\perp$, B_v and F_v as zeroth-order quantities, $L_\perp = O(1)$, $B_v = O(1)$, $F_v = O(1)$, it follows that $L_\parallel = O(\lambda^{-1})$, $\nabla^\perp = O(1)$, $\partial^\parallel = O(\lambda)$, $\Psi = O(\lambda)$ and $\Omega = O(\lambda^2)$. Meanwhile, the force imbalance due to the reduction is $\vec{f}_{imb} = \nabla p - \vec{j}\times\vec{B} = \vec{j}_f\times\vec{B}_f - \vec{j}\times\vec{B}$, where $\vec{B} = \nabla\chi + \nabla\Psi\times\nabla\chi$ and $\vec{B}_f = \vec{B} + \nabla\Omega\times\nabla\psi_v$. Inserting the ansatzes, the following expression is obtained for the residual force:

$$\begin{aligned}\vec{f}_{res} = {} & \frac{1}{\mu_0}[\nabla\times(\nabla\Psi\times\nabla\chi)]\times(\nabla\Omega\times\nabla\psi_v) + \frac{1}{\mu_0}[\nabla\times(\nabla\Omega\times\nabla\psi_v)]\times\nabla\chi \\ & + \frac{1}{\mu_0}[\nabla\times(\nabla\Omega\times\nabla\psi_v)]\times(\nabla\Psi\times\nabla\chi) + \frac{1}{\mu_0}[\nabla\times(\nabla\Omega\times\nabla\psi_v)]\times(\nabla\Omega\times\nabla\psi_v)\end{aligned} \tag{2.70}$$

After some algebra, the reduced MHD current can be written as

$$\begin{aligned}\vec{j} &= \frac{1}{\mu_0}\nabla\times(\nabla\Psi\times\nabla\chi) = \frac{1}{\mu_0}\Delta^*\Psi\nabla\chi + \vec{j}^\perp, \\ \vec{j}^\perp &= \frac{1}{\mu_0}\left(B_v\partial^\parallel\frac{\partial\Psi}{\partial q^i}\vec{e}^{\,i} - g^{kn}\frac{\partial\Psi}{\partial q^k}B_v\partial^\parallel g_{ni}\vec{e}^{\,i}\right),\end{aligned} \tag{2.71}$$

where the Einstein summation convention is used, with $k, n \in \{\psi_v, \beta_v, \chi\}$ and $i \in \{\psi_v, \beta_v\}$. Here, $\Delta^* = B_v^{-2}\nabla\cdot(B_v^2\nabla^\perp$, g is the metric tensor of the Clebsch-type coordinate system aligned to $\nabla\chi$, q^i represents the actual coordinates: $q^i \in \{\psi_v, \beta_v\}$, and $\vec{e}^{\,i}$ are the contravariant basis vectors: $\vec{e}^{\,i} \in \{\nabla\psi_v, \nabla\beta_v\}$. With this,

the first term in the residual force (2.70) expands to

$$-\frac{\partial\Omega}{\partial\beta_v}\vec{j}^{\perp}\times\nabla\chi-\frac{\Delta^*\Psi}{\mu_0}B_v\partial^{\parallel}\Omega\nabla\chi\times\vec{e}_{\beta_v}+B_v\partial^{\parallel}\Omega\vec{j}^{\perp}\times\vec{e}_{\beta_v}.$$

Since $\vec{j}^{\perp}=O(\lambda^2)$, it is easy to see that the first two terms above are $O(\lambda^4)$ and the third term is $O(\lambda^5)$.

The second term in the residual force (2.70) can be expanded as

$$\nabla\psi_v B_v\partial^{\parallel}(\nabla\Omega\times\nabla\psi_v)_{\psi_v}+\nabla\beta_v B_v\partial^{\parallel}(\nabla\Omega\times\nabla\psi_v)_{\beta_v}-B_v^2\nabla^{\perp}(\nabla\Omega\times\nabla\psi_v)_{\chi}$$

Note that $\nabla\Omega\times\nabla\psi_v=-(\partial\Omega/\partial\beta_v)\nabla\chi+(\partial\Omega/\partial\chi)\vec{e}_{\beta_v}/J$, where $\vec{e}_{\beta_v}=J\nabla\chi\times\nabla\psi_v$ is the covariant basis vector in the β_v direction in the Clebsch-type coordinate system aligned to $\nabla\chi$, and $J=[(\nabla\psi_v\times\nabla\beta_v)\cdot\nabla\chi]^{-1}=1/B_v^2$ is the Jacobian. Furthermore, since $B_v\partial/\partial\chi=\partial^{\parallel}$, one has $(\nabla\Omega\times\nabla\psi_v)_{\psi_v}=g_{\psi_v\beta_v}B_v\partial^{\parallel}\Omega$ and $(\nabla\Omega\times\nabla\psi_v)_{\beta_v}=g_{\beta_v\beta_v}B_v\partial^{\parallel}\Omega$. Thus, the first two terms above are $O(\lambda^4)$ and the third term is $O(\lambda^2)$. However, it is easy to see that the third term is in the kernel of the first projection operator in (2.27), and so this term will not contribute to the force balance error in the Φ evolution equation (2.41). Applying the second projection operator in (2.27) to the third term increases its order by λ, and so it will only contribute as $O(\lambda^3)$ in the $v_{\parallel}$ evolution equation (2.42).

The curl of the last term of the magnetic field ansatz can also be written as

$$\nabla\times(\nabla\Omega\times\nabla\psi_v)=-\nabla\frac{\partial\Omega}{\partial\beta_v}\times\nabla\chi+\nabla(B_v\partial^{\parallel}\Omega)\times\vec{e}_{\beta_v}+B_v\partial^{\parallel}\Omega\nabla\times\vec{e}_{\beta_v}.$$

Note that the first term is $O(\lambda^2)$ and the other two terms are $O(\lambda^3)$. The third term in the residual force (2.70) is then

$$-\left(\nabla\frac{\partial\Omega}{\partial\beta_v}\times\nabla\chi\right)\times(\nabla\Psi\times\nabla\chi)+O(\lambda^4)=\nabla\Psi\cdot\left(\nabla\frac{\partial\Omega}{\partial\beta_v}\times\nabla\chi\right)\nabla\chi+O(\lambda^4).$$

Terms of order λ^4 are not written out explicitly since there is no need to consider them, as it is already established that there is at least an $O(\lambda^4)$ contribution to equation (2.41). As can be seen, $O(\lambda^3)$ term above will be cancelled by the first projection operator in (2.27) and as such will not contribute to the Φ equation (2.41), however it will still contribute as $O(\lambda^3)$ to the $v_{\parallel}$ equation (2.42).

Finally, the last term in the residual force (2.70) is clearly of order λ^4 or higher, so there is no need to consider it in detail like the other terms. In order to compare

the residual force contributions to the other terms in equations (2.41) and (2.42), some more ordering needs to be done. Consider that the shortest time scale in the reduced system is the Alfvén time $\tau_A \equiv c_A/L_\parallel$, where the parallel length scale is used because the Alfvén wave travels along field lines, and so the time derivative is ordered as $|\partial/\partial t| \sim 1/\tau_A$. As such, $\partial/\partial t = O(\lambda)$. The Φ and $v_\parallel$ terms in the velocity ansatz are then ordered as

$$|v_\parallel \vec{B}| \div \frac{|\nabla\Phi \times \nabla\chi|}{B_v^2} \sim B_v^2 \frac{|v_\parallel|}{|\nabla^\perp \Phi|} \sim 1.$$

Assuming that the partial and convective terms in the material derivative are of the same order, $|\partial/\partial t| \sim |\vec{v} \cdot \nabla|$, one has $\Phi, v_\parallel = O(\lambda)$. After identifying $\rho = O(1)$, $\mu_\perp, \mu_\parallel, P = O(\lambda)$ and $p = O(\lambda^2)$, it is clear that the lowest order terms in equations (2.41) and (2.42) are $O(\lambda^2)$. Thus, the force balance error is at least one order of λ higher than the equations. In the stellarator simulations presented in chapter 4, the model without $v_\parallel$ will be used, where the force balance error is two orders of λ higher than the equations, since equation (2.42) is not included.

3 Testing the models in the tokamak limit

Having derived the main and alternate models in the previous chapter, it makes sense to first do some test runs simulating tokamaks, before moving on to stellarators. However, since in the tokamak limit, the main model reduces to the standard JOREK reduced MHD model that has already been used extensively in JOREK, there is not much to test in this model, except for momentum conservation, which has not been looked at before, and will be considered in section 3.2. The next section will deal mostly with the alternate model, which will not be studied any further after this chapter: the stellarator simulations in the next chapter will be carried out using the main model.

When implementing the models in JOREK, two auxilliary variables are introduced: $j = \Delta^*\Psi$ and $\omega = \Delta^\perp\Phi$, where $\Delta^* = B_v^{-2}\nabla\cdot(B_v^2\nabla^\perp$. These two variables are stored independently from Ψ and Φ, and have their own separate degrees of freedom. This allows one to avoid having second order derivatives in non-dissipative terms when the equations are written in weak form, where integration by parts moves one derivative to the test function. Since the finite element representation in JOREK is G^1 continuous, avoiding second order derivatives improves numerical stability by eliminating jump discontinuities. Note that this does not apply to derivatives with respect to ϕ, which are continuous to arbitrary order, due to the use of a Fourier series for toroidal discretization. Thus, the presence of higher order toroidal derivatives is not a problem. In addition, the auxilliary variables allow one to introduce hyperresistivity and hyperviscosity terms, which, without the auxilliary variables, would have involved derivatives of third and fourth order, respectively, in the weak form. However, the JOREK finite element basis, consisting of piecewise third order polynomials, does not have meaningful derivatives beyond

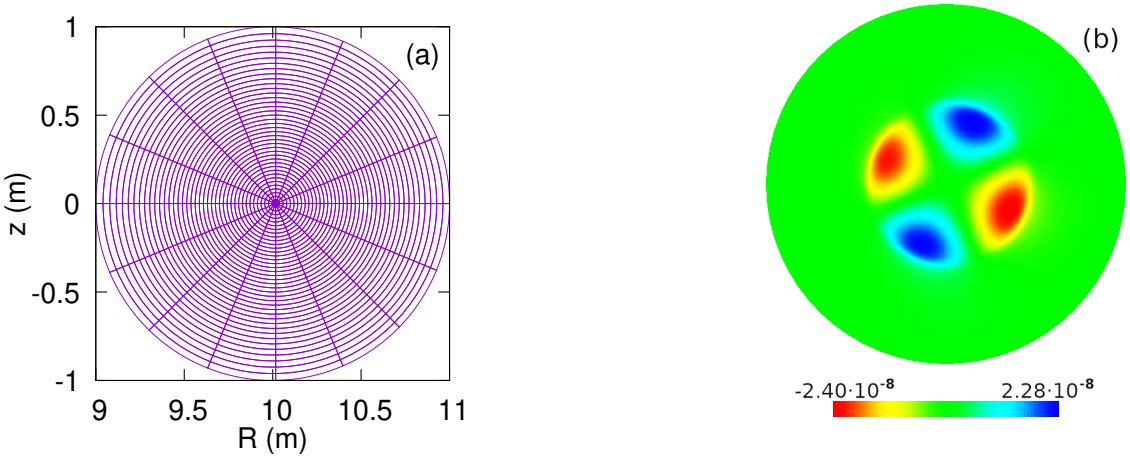

Figure 3.1: A flux surface aligned grid used in one of the simulations (a), and the unstable $n = 1$ Fourier mode of $\psi = F_0\Psi$ (JOREK units) in the standard tokamak model at $t = 50000$ Alfvén times (b).

the second order. Similar auxilliary variables j and w are used in the standard tokamak model in JOREK, as mentioned in section 1.3.2.

3.1 Benchmarking tearing modes in the alternate model

The simulations in this section were carried out for tearing modes in a tokamak with a circular cross section and an aspect ratio of 10. The reduced alternate model without $v_\parallel$ will be compared to the standard JOREK tokamak model without $v_\parallel$, which is identical to the reduced main model, as presented in section 2.5, with $\chi = F_0\phi$. In this section, $F_0 = 10\ \mathrm{T}\cdot\mathrm{m}$. The simulation is started from equilibrium, with the initial conditions for Ψ being determined from the Grad-Shafranov equation with $FF'(\psi_n) = 1.173(1-\psi_n)$ in units of $\mathrm{T}^2\cdot\mathrm{m}$, where $\psi_n = (\psi-\psi_{axis})/(\psi_{edge}-\psi_{axis})$ is the normalized poloidal flux, and zero beta: $p(\psi_n) = 0$. The ψ in the JOREK Grad-Shafranov sovler (denoted by lowercase ψ to avoid confusion) is normalized differently than the Ψ in the magnetic field ansatz (2.2), due to the solver originally being written for use with the model presented in section 1.3.2. The relation between the two psi's is $\psi = F_0\Psi$. Further, the initial density was set to a constant value of $3.346\cdot10^{-7}\mathrm{kg/m}^3$, which, for a pure deuterium plasma, equals 10^{20} deu-

Reduced alternate model	Standard tokamak model
$\frac{\partial \rho}{\partial t} = -B_v \left[\frac{\rho}{B_v^2}, \Phi\right] + P$	$\frac{\partial \rho}{\partial t} = \frac{1}{R}\left[R^2\rho, u\right] + P$
$\left[\psi_v, \frac{\partial \Psi}{\partial t}\right] = \left[\frac{[\Psi,\Phi]-\partial^\parallel \Phi}{B_v}, \psi_v\right] + \frac{1}{B_v}\nabla\cdot(\eta\nabla\psi_v \times \vec{j}_d^\parallel)$	$\frac{\partial \psi}{\partial t} = -F_0\frac{\partial u}{\partial \phi} + R\left[\psi, u\right] - \eta(j - j_0)$
$\Delta^\perp \frac{\partial \Phi}{\partial t} = \nabla\cdot\left[\frac{B_v \partial^\parallel v^2}{2}\nabla^\perp\Psi + \omega_\chi \nabla\Phi\times\nabla\chi\right.$	$\nabla\cdot\left(R^2\rho\nabla^\perp\frac{\partial u}{\partial t}\right) = \frac{-1}{2R}\left[R^2\rho, v^2\right]$
$-v_\chi B_v^2 \vec{\omega}^\perp + \frac{B^2}{\rho}\vec{j}^\perp - \frac{j_\chi B_v^2}{\rho}\nabla\Psi\times\nabla\chi - \frac{1}{\rho}\vec{f}_b\times\nabla\chi$	$+\frac{1}{R}\left[R^4\rho w, u\right] + \frac{F_0}{R^2}\frac{\partial j}{\partial \phi} + \frac{1}{R}\left[j, \psi\right]$
$\left.-\frac{P}{\rho}\nabla^\perp\Phi\right] + \nu\Delta\omega - \nu_h\Delta^2\omega$	$+\nabla\cdot(\mu_\perp^t\nabla^\perp w)$
$\vec{B} = \nabla\chi + \nabla\Psi\times\nabla\chi;\ \vec{v} = \frac{\nabla\Phi\times\nabla\chi}{B_v^2}$	$\vec{B} = F_0\nabla\phi + \nabla\psi\times\nabla\phi$
$\vec{j} = \frac{-1}{\mu_0}\left[\left(j - \frac{(B_v^2,\Psi)}{B_v^2} + B_v\partial^\parallel\left(\frac{\partial^\parallel\Psi}{B_v}\right)\right)\nabla\chi\right.$	$\vec{v} = R^2\nabla\phi\times\nabla u$
$\left.+B_v\partial^\parallel\nabla\Psi - (\nabla\Psi\cdot\nabla)\nabla\chi\right]$	
$\vec{\omega} = \frac{-\nabla\chi}{B_v^2}\left[\omega + B_v\partial^\parallel\left(\frac{\partial^\parallel\Phi}{B_v}\right)\right] + \frac{1}{B_v}\partial^\parallel\nabla\Phi$	
$-\frac{1}{B_v^2}(\nabla\Phi\cdot\nabla)\nabla\chi - \frac{2\nabla\Phi}{B_v^2}\partial^\parallel B_v + \frac{2\nabla\chi}{B_v^3}\nabla B_v\cdot\nabla\Phi$	
$j = \Delta^*\Psi;\ \omega = \Delta^\perp\Phi$	$j = \Delta^*\psi;\ w = \Delta^\perp u$

Table 3.1: The zero-β limit of the two models compared here: the reduced alternate model and the standard tokamak model, both with $v_\parallel = 0$. In the simulations discussed in this section, $P = \nabla\cdot(D_\perp\nabla_\perp\rho)$, $\chi = F_0\phi$ and $\psi_v = R$, where R is the distance from the central axis of symmetry, and $\vec{f}_b = -FF'\nabla\Psi|_{t=0}/R^2$ is the force balancing term. Subscripts represent covariant components. In order to make the initial condition a true equilibrium, a current source was introduced: $\vec{j}_d = \vec{j} - \vec{j}_0$, where $\vec{j}_0$ is the current at $t = 0$.

terium ions per cubic meter. The viscosity was set to $\mu = 5.159\cdot10^{-8}$ kg/(m · s), which is equivalent to 10^{-5} in JOREK units for $\mu_\perp^t$ in the standard tokamak model. Note that $\mu_\perp^t$ is not the same as $\mu_\perp$ in equation (2.30), instead $\mu_\perp^t = F_0^2\mu_\perp$. In the alternate model, a constant kinematic viscosity of $\nu = \mu/\rho_0 = 0.1542$ m^2/s (10^{-7} in JOREK units) was used. Finally, unless otherwise noted, only the $n = 0$ and $n = 1$ Fourier modes were kept in the toroidal discretization in all simulations, corrsponding to $N_{\text{tor}} = 3$ in JOREK, and the Crank-Nicolson time scheme was used for time stepping. For reference, Figure 3.1 shows a sample flux surface aligned grid used to simulate the tokamak, and the tearing mode perturbation to $F_0\Psi$. Since the pressure was set to zero, equation (2.38) is identically zero (resistive heating is not taken into account), and there is no need to evolve pressure, as it will stay at zero. For clarity, the precise systems of equations evolved are listed in Table 3.1.

The first test consisted of comparing the growth rates of the tearing mode in the

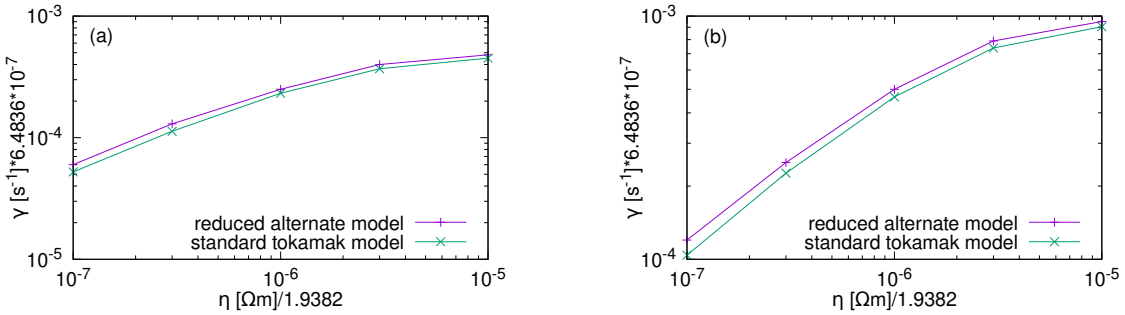

Figure 3.2: Tearing mode growth rates at five different resistivities in the reduced alternate model and the standard tokamak model without $v_{\parallel}$. The growth rates for the unstable $n = 1$ Fourier mode in simulations with $n = 0, 1$ are shown in (a), and those for the $n = 2$ toroidal mode in simulations with $n = 0, ..., 4$ are shown in (b). Note that the $n = 2$ growth rates are two times the value the $n = 1$ growth rates, suggesting that the $n = 2$ modes are not inherently unstable but driven by the $n = 1$ modes via nonlinear mode coupling.

two models at different resistivities. For both models, a scan was done over the spatial and temporal resolutions at each resistivity until the growth rate converged. The simulations were then repeated with Fourier modes $n = 0, ..., 4$ ($N_{\text{tor}} = 9$ in JOREK) with the same resolution and time step for which the growth rates converged in the $n = 0, 1$ simulations at the corresponding resistivity. Figure 3.2 shows the growth rates of the $n = 1$ mode, as measured in the $n = 0, 1$ simulations, (a), and the growth rates of the $n = 2$ mode (b), which is not unstable by itself, but rather nonlinearly driven by the $n = 1$ mode. As expected, the $n = 2$ growth rate is greater than the $n = 1$ growth rate at the corresponding resistivity by approximately a factor of two. The $n = 3$ and $n = 4$ modes are destabilized right before the transition into the post-saturation regime, and so their growth rates (not shown here) do not plateau, but rather peak at values approximately three and four times the $n = 1$ growth rate, respectively, before decreasing due to the mode saturating.

As can be seen, the alternate model does not deviate much from the predictions of the standard tokamak model in the linear regime and at $\beta = 0$, two problems appear after the onset of saturation. The first problem, which was already discussed in

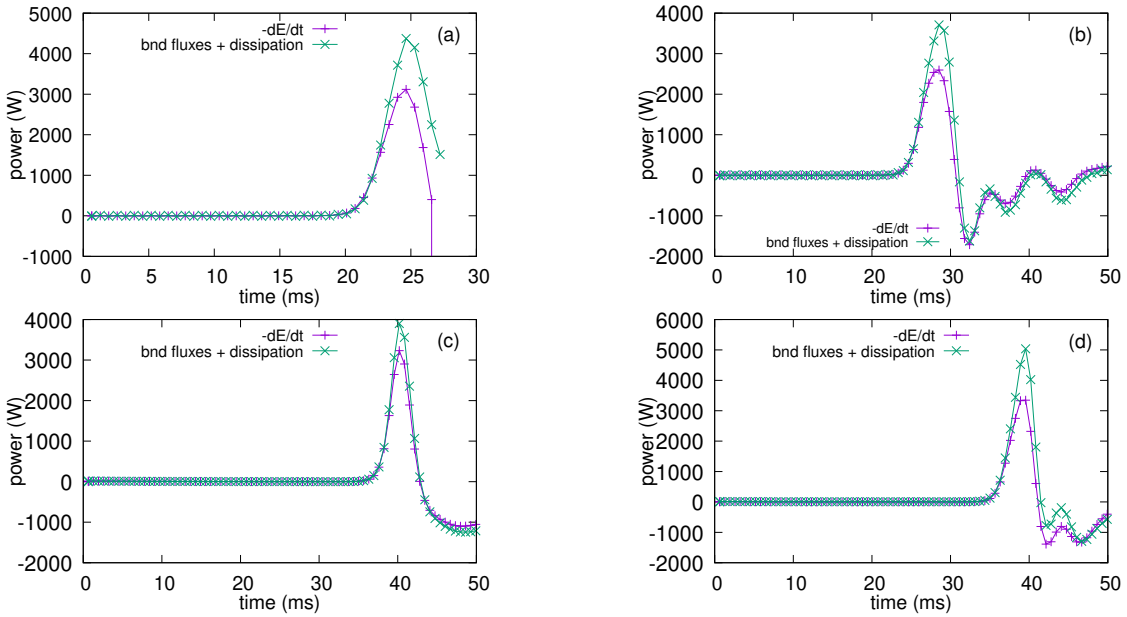

Figure 3.3: The value of $-dE/dt$ is plotted against the physical energy loss rate in (a) the reduced alternate model without artificial dissipation, (b) the reduced alternate model with hyperviscosity, (c) the standard tokamak model, and (d) the reduced alternate model using equation (2.45) instead of the Ψ equation in Table 3.1.

section 2.6.1, is that the reduced alternate model does not satisfy the kinetic energy equation, and so nonphysical kinetic energy can be generated. This error in energy conservation is small in the linear regime, but may become significant as saturation is approached. In Figure 3.3, the negative rate of change of the integrated total energy, $-dE/dt$, is compared to the physical energy loss rate for the simulation with resistivity $1.9382 \cdot 10^{-5}\Omega \cdot \mathrm{m}$ (10^{-5} JOREK units). The physical energy loss rate is simply the surface integral of any energy fluxes across the boundary plus the volume integral of any energy sinks. In this case, the energy sinks are due to viscous and resistive dissipation; since conversion of kinetic and magnetic energies to internal energy is not taken into account, dissipated energy is lost. The physical energy loss rate can be negative, i.e. energy is being gained, if the inward fluxes are greater than the outward fluxes plus sinks. Figure 3.3 a shows that the nonphysical energy generation rate (difference between the physical energy loss rate and $-dE/dt$) is

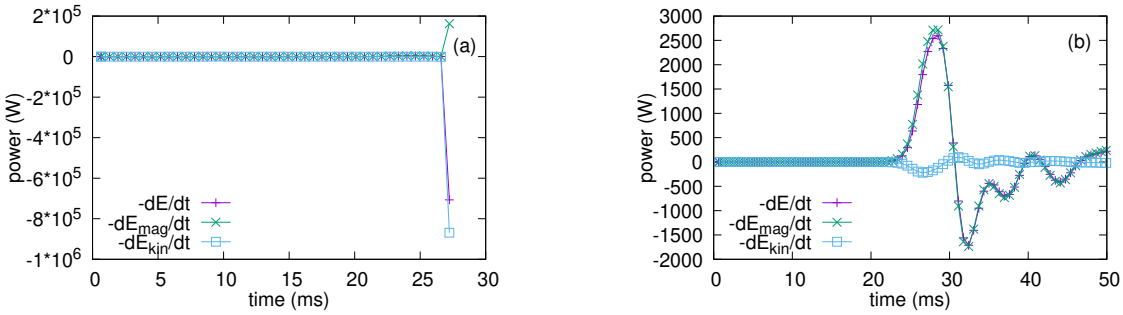

Figure 3.4: The $-dE/dt$ curve from Figure 3.3 plotted alongside the dE_{mag}/dt and dE_{kin}/dt curves for magnetic and kinetic energies, where $dE/dt = dE_{mag}/dt + dE_{kin}/dt$. Plot (a) is for the reduced alternate model without artificial dissipation, and (b) is for the reduced alternate model with hyperviscosity.

negligible in the linear regime, until about 20 ms, after which saturation sets in and the nonphysical energy generation rate grows rapidly. The simulation is stopped around 27 ms, as it would anyway crash quickly after that. One way to alleviate this problem is to add artificial dissipation in the form of a hyperviscosity term. Figure 3.3 b shows the result of a simulation with a hyperviscosity of $\nu_h = 1.08 \cdot 10^{-3}$ m^4/s ($7 \cdot 10^{-10}$ JOREK units). Note that the physical energy loss rate does not include dissipation due to hyperviscosity. With the hyperviscosity term in place, the simulation behaves much more reasonably, although the energy is still not conserved, as evidenced by the mismatch of the two curves in the plot. Since the energy conservation error comes mostly from the kinetic energy, which can be kept in check by the hyperviscosity term in the Φ evolution equation, the energy conservation error is minimized. Finally, as will be discussed below, inaccuracies in solution to the Ψ equation can result in numerical errors appearing in the magnetic field. The hyperviscosity slows down the plasma response to these numerical errors, stabilizing it against numerical instabilities that could otherwise occur.

For proper comparison, a similar plot with $-dE/dt$ and physical energy loss rate is also shown for the standard JOREK tokamak model in Figure 3.3 c. This plot also shows a mismatch between the two curves, albeit much smaller than the previous two. In this case, however, the error is purely numerical. This numerical

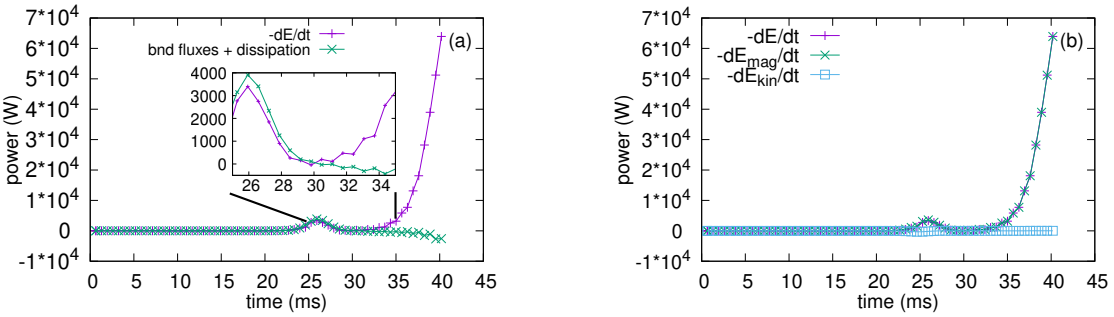

Figure 3.5: A tearing mode simulation using the standard tokamak model when the ψ equation is replaced with equation (2.39). Plot (a) is a comparison of $-dE/dt$ with the physical loss rate and (b) shows the curves for dE_{mag}/dt, dE_{kin}/dt and $-dE/dt$.

error is sensitive to two parameters: the number of toroidal Fourier modes included in the solution and the time step. By running more simulations (the corresponding plots are not shown here) with smaller time steps and more Fourier modes, it was confirmed that the error can be made arbitrarily small.

The second of the two problems mentioned above is that the Ψ evolution equation, when expressed in the form shown in Table 3.1, can cause numerical instabilities, as it contributes significantly to the condition number of the time stepping matrices. The numerical errors in the magnetic field are what destabilizes the kinetic energy and causes it to explode, as shown in Figures 3.3 a and 3.4 a. Replacing the Ψ equation (2.39) by equation (2.45) prevents the kinetic energy from exploding without requiring the introduction of a hyperviscosity. This is shown in Figure 3.3 d, where the simulation continues to run normally after the end of the linear regime, although it does have a higher energy conservation error than when hyperviscosity is present.

Another interesting test would be to replace the ψ evolution equation in the standard tokamak model, as shown in Table 3.1, with the Ψ equation (2.39). This allows one to see how the Ψ equation (2.39) will behave in a situation where energy is conserved in the continuous limit. The $-dE/dt$ and physical energy loss rate for such a simulation are plotted in Figure 3.5 a. Here, the energy conservation

error begins to rise near the same point in time where the reduced alternate model without hyperviscosity, shown in Figure 3.3 a, would have crashed. In this case, however, instead of rapidly increasing like in the alternate model without hyperviscosity, the energy rapidly decays, and so this simulation can run for a longer period of time. Figure 3.5 b shows the negative rates of change for the integrated kinetic, magnetic and total energies in this simulation. One can see from this figure that the violation of energy conservation here is solely due to the buildup of numerical error in Ψ, and the kinetic energy is not involved in this numerical instability.

Finally, for both the reduced alternate and standard tokamak models, it was confirmed that the tearing mode growth rates are not affected by the choice of evolution equation for Ψ or ψ. Although equations (2.39) and (2.45) are equivalent from the analytical point of view, equation (2.45) is much more numerically stable, and thus more preferable.

To conclude this section, it should be noted that one can run the alternate reduced model with a finite pressure without affecting the energy conservation, as all of the error comes from the kinetic energy. However, simulations have shown that the reduced alternate model cannot accurately reproduce the tearing mode growth rates when the plasma β is not negligible. This is most likely because all of the pressure terms in equation (2.43) contain either $\nabla\rho$ or $\partial^{\parallel}p$, both of which are zero at $t = 0$, and so these terms are negligible in the linear regime.

3.2 Global momentum conservation error in the main model

In this section, the momentum conservation error will be compared between the main model with $v_{\parallel}$ and the main model without $v_{\parallel}$. As discussed in section 2.6.3, the momentum conservation error should be greater when $v_{\parallel}$ is present, which is confirmed by the simulations. One caveat that should be pointed out, however, is that section 2.6.3 considers local conservation of momentum, whereas the present section is concerned only with global momentum conservation. The simulations in

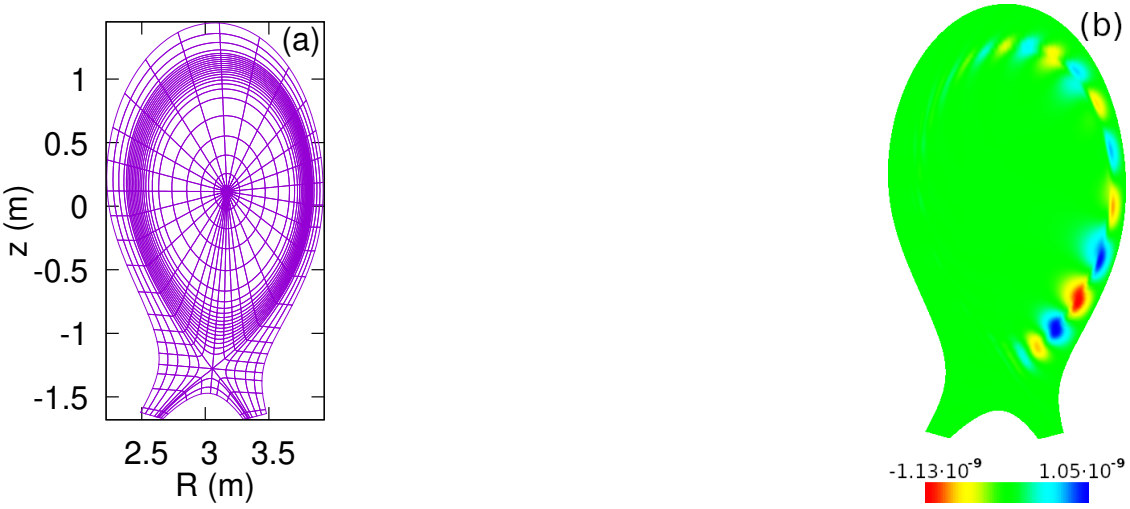

Figure 3.6: A flux surface aligned grid (resolution reduced for clarity) used for simulating the ballooning mode (a), and the sum of all $n > 0$ Fourier modes of $F_0\Psi$ (JOREK units) at 250 time steps, or $t = 641.1$ Alfvén times (b).

this section were carried out for ballooning modes in an X-point tokamak with an aspect ratio of 3; the cross section is shown in Figure 3.6. The following simulation parameters were used: Fourier modes $n = 0, ..., 6$ were included ($N_{\text{tor}} = 13$), $F_0 = 3\ \text{T} \cdot \text{m}$, a time step of 3 Alfvén times, a resistivity of $\eta = 3.8764 \cdot 10^{-6}\ \Omega \cdot \text{m}$ ($2 \cdot 10^{-6}$ JOREK units), and a viscosity of $\mu = 2.293 \cdot 10^{-7}\ \text{kg}/(\text{m} \cdot \text{s})$ ($\mu_\perp^t = 4 \cdot 10^{-6}$ JOREK units). When solving the Grad-Shafranov equation for initial conditions with the following profiles:

$$FF'(\psi_n) = \frac{1}{2}\left[1.6(1-\psi_n) - 0.43\cosh^{-2}\frac{\psi_n - 0.9}{0.07}\right]\left(1 - \tanh\frac{\psi_n - 1}{0.03}\right),$$

and $p(\psi_n) = \rho(\psi_n)T(\psi_n)$, with $T(\psi_n) = 0.015(1-0.66\psi_n)[1-\tanh((\psi_n-0.94)/0.08)]/2+3 \cdot 10^{-4}$ and $\rho(\psi_n) = [1 - \tanh((\psi_n - 0.94)/0.08)]/2 + 0.01$. In these expressions, FF' has units of $\text{T}^2 \cdot \text{m}$, T has units of $(10^{20} k_B \mu_0) \cdot \text{K}$ and ρ is in units of $3.346 \cdot 10^{-7}\text{kg/m}^3$. Finally, since the main model matches the JOREK standard tokamak model in the tokamak limit, the standard tokamak model was used to run the simulations presented here.

Consider the total linear momentum of the plasma in the Cartesian x- and y-directions, calculated by integrating ρv_x and ρv_y over the plasma volume. Here,

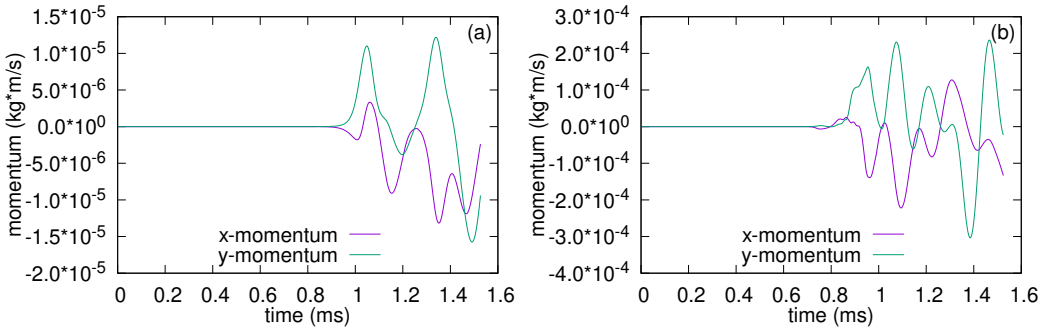

Figure 3.7: Total linear momentum of the plasma in the Cartesian x- and y-directions as a function of time in the simulation using the model with $v_{\parallel} = 0$ (a), and the simulation using model with $v_{\parallel} \neq 0$ (b).

the x-direction was chosen to be the cylindrical R-direction when $\phi = 0$, and the y-direction was chosen to be the cylindrical R-direction when $\phi = \pi/2$, with the Cartesian and cylindrical z-axes coinciding. Violation of momentum conservation was observed in the x- and y-directions. Momentum conservation error in the z-direction was solely due to numerical discretization, as global z-momentum is conserved in the continuous limit. This can be seen by setting $\Phi^* = \ln R$ in equation (2.46), and taking into account that $B_v = F_0/R$ in the tokamak limit.

Figure 3.7 shows the x- and y-components, P_x and P_y of the total plasma momentum for both with and without $v_{\parallel}$. In both cases, it was confirmed that dP_x/dt and dP_y/dt exceed the surface integral of the momentum flux across the boundary by several orders of magnitude. Thus, the momenta in Figure 3.7 cannot be explained by momentum exchange with the walls; these are nonphysical momenta that arise due to the inaccuracies discussed in section 2.6.3. Note that in Figure 3.7, after about 1 ms, the momenta no longer grow, but rather oscillate, with the amplitude staying around the same order of magnitude. These oscillations begin at about the same point in time when saturation is reached. As expected, the momentum conservation error in the case with $v_{\parallel} \neq 0$ is worse than in the case with $v_{\parallel} = 0$, as indicated by the nonphysical momentum being more than an order of magnitude greater in the former case than in the latter.

4 Stellarator simulations

In previous chapters, the stellarator models were either studied analytically, or tested in the tokamak limit. The present chapter reports the results of first of a kind fully three-dimensional stellarator simulations in JOREK using the reduced MHD model without parallel flow. All of the simulations presented in this chapter start from a set of simple stellarator equilibria that are based on the historic Wendelstein 7-A stellarator [35]. More complicated configurations, such as Wendelstein 7-X, can be studied using the present code version, but at increase computational effort, and so they are left for future work. The equilibria were calculated using the GVEC code [36].

As previously stated, the tokamak limit corresponds to setting $\chi = F_0\phi$ in the equations. For stellarators, it is necessary to be able to work with a general scalar potential χ. Fortunately, it is possible to represent an arbitrary χ analytically: since $\nabla\chi$ is a magnetic field, it must be divergence-free, so $\Delta\chi = 0$. One then needs to find a general solution to the Laplace equation in the toroidal coordinate system (R, z, ϕ), which was done by Dommaschk in Ref [37]. Dommaschk provides his solution as a sum over harmonics, where any particular solution is determined by the coefficients of these harmonics. In order to determine the coefficients for a particular equilibrium, one needs to first calculate the vacuum field on an (R, z, ϕ) grid, which is done here using the EXTENDER_P code [38].

Using the Dommaschk potential formulation for χ in conjunction with the non-axisymmetric flux surface aligned grids described in section 1.4 allows one to simulate stellarators relatively efficiently. The steps to run a stellarator simulation can then be summarized as follows:

1. Calculate an equilibrium for the stellarator in question using the GVEC code

2. Use the output of GVEC to calculate the contribution to the stellarator's magnetic field from the coils (i.e. the curl-free/vacuum field) with the EXTENDER_P code
3. Calculate the coefficients for the Dommaschk representation of the scalar potential from the output of EXTENDER_P using a utility developed as a part of this thesis project
4. Build a flux surface aligned grid from the geometry data in the GVEC solution using a utility written by R. Ramasamy, and import it into JOREK
5. Calculate the $\widetilde{j}$, Ψ and temperature variables from the GVEC solution
6. Using the results of the previous step as an initial condition, evolve the system in time using the stellarator reduced MHD equations in JOREK

This procedure will be elaborated on in the following sections.

4.1 Finding the Dommaschk representation of a scalar potential

Since χ is a solution of the Laplace equation in a torus, it can be represented as a summation over harmonics

$$\chi = F_0\phi + \sum_{m,l} \chi_{m,l}, \tag{4.1}$$

where $F_0\phi$ corresponds to a tokamak-like toroidal field, m is the toroidal mode number, l is the poloidal mode number, and each harmonic satisfies the Laplace equation individually: $\Delta\chi_{m,l} = 0$. Dommaschk gives a more explicit representation for χ [37]:

$$\begin{aligned}\widetilde{\chi} = \phi + \sum_{m,l} \Big[&(a_{m,l}\cos m\phi + b_{m,l}\sin m\phi) D_{m,l}(\widetilde{R},\widetilde{z}) \\ &+ (c_{m,l}\cos m\phi + d_{m,l}\sin m\phi) N_{m,l-1}(\widetilde{R},\widetilde{z}) \Big],\end{aligned} \tag{4.2}$$

where a tilde denotes normalization: $\chi = F_0\widetilde{\chi}$, $R = R_0\widetilde{R}$ and $z = R_0\widetilde{z}$; the normalization factor R_0 is the toroidally averaged radial position of the magnetic

axis of the vacuum field. The functions $D_{m,l}$ and $N_{m,l}$ are defined as:

$$\{D,N\}_{m,l}(\widetilde{R},\widetilde{z}) = \sum_{k=0}^{2k\leq l} \frac{\widetilde{z}^{l-2k}}{(l-2k)!} C_{m,k}^{\{D,N\}}(\widetilde{R}), \tag{4.3}$$

and

$$\begin{aligned} C_{m,l}^{D}(\widetilde{R}) = \sum_{k=0}^{l} [& -(\alpha_k(\alpha_{l-m-k}^{*}\ln\widetilde{R} + \gamma_{l-m-k}^{*} - \alpha_{l-m-k}) - \gamma_k\alpha_{l-m-k}^{*} + \alpha_k\beta_{l-k}^{*})\widetilde{R}^{2k+m} \\ & + \beta_k\alpha_{l-k}^{*}\widetilde{R}^{2k-m}], \\ C_{m,l}^{N}(\widetilde{R}) = \sum_{k=0}^{l} [& (\alpha_k(\alpha_{l-m-k}\ln\widetilde{R} + \gamma_{l-m-k}) - \gamma_k\alpha_{l-m-k} + \alpha_k\beta_{l-k})\widetilde{R}^{2k+m} \\ & - \beta_k\alpha_{l-k}\widetilde{R}^{2k-m}]. \end{aligned} \tag{4.4}$$

The coefficients α_n, β_n and γ_n are defined as

$$\begin{aligned} \alpha_n &= \frac{(-1)^n}{2^{2n+m}\Gamma(m+n+1)\Gamma(n+1)}, \qquad \alpha_n^{*} = (2n+m)\alpha_n, \qquad n \geq 0, \\ \beta_n &= \frac{\Gamma(m-n)}{2^{2n-m+1}\Gamma(n+1)}, \qquad \beta_n^{*} = (2n-m)\beta_n, \qquad n \geq 0 \text{ and } m > n, \\ \gamma_n &= \frac{\alpha_n}{2}\sum_{i=1}^{n}\left(\frac{1}{i} + \frac{1}{m+i}\right), \qquad \gamma_n^{*} = (2n+m)\gamma_n, \qquad n > 0. \end{aligned} \tag{4.5}$$

Although not written out explicitly, it can be seen that the coefficients also depend on m, the toroidal mode number of the D or N function that is being evaluated. If the conditions on n and/or m above are not satisfied, then the corresponding coefficient and its starred version are zero. Finally, the coefficients $a_{m,l}$, $b_{m,l}$, $c_{m,l}$ and $d_{m,l}$ in equation (4.2) are what determines a particular configuration and must be calculated from the EXTENDER_P output.

Note that, since the harmonics $\chi_{m,l}$ are given analytically, the property that $\Delta\chi_{m,l} = 0$ is satisfied exactly. This is an important advantage of using the Dommaschk representation for χ instead of the finite element representation (1.30), as it guarantees that the divergence-free condition on the magnetic field will be satisfied to machine precision. The second advantage is that χ and its derivatives are smooth.

EXTENDER_P provides the values of the three cylindrical components of the

vacuum magnetic field, which will be referred to as $\vec{B}_E$, on an (R, z, ϕ) grid. Setting $\nabla\chi = \vec{B}_E$ and considering the ϕ component, $B_{E,\phi} = \hat{\phi} \cdot \vec{B}_E = R^{-1}\partial\chi/\partial\phi$, one has:

$$\frac{R_0}{F_0} B_{E,\phi} = \widetilde{R}^{-1}\frac{\partial\widetilde{\chi}}{\partial\phi} = \widetilde{R}^{-1} + \widetilde{R}^{-1}\sum_{m,l} m\Big[(-a_{m,l}\sin m\phi + b_{m,l}\cos m\phi) D_{m,l}(\widetilde{R},\widetilde{z}) + (-c_{m,l}\sin m\phi + d_{m,l}\cos m\phi) N_{m,l-1}(\widetilde{R},\widetilde{z})\Big]. \tag{4.6}$$

Now, using the properties of the $D_{m,n}$ and $N_{m,n}$ functions given by equations (10) and (11) of Ref [37], equation (4.6) is evaluated at $\widetilde{R} = 1$:

$$\frac{R_0}{F_0} B_{E,\phi}\bigg|_{\widetilde{R}=1} = 1 + \sum_{m,l} m(-a_{m,l}\sin m\phi + b_{m,l}\cos m\phi)\frac{\widetilde{z}^l}{l!}. \tag{4.7}$$

If one also evaluates at $\widetilde{z} = 0$ and integrates over ϕ, F_0 can be calculated:

$$F_0 = \frac{R_0}{2\pi}\int_0^{2\pi} B_{E,\phi}|_{\widetilde{R}=1,\widetilde{z}=0}\, d\phi. \tag{4.8}$$

To calculate the coefficients $a_{m,l}$ and $b_{m,l}$, one must first multiply by either $\sin m\phi$ or $\cos m\phi$ and then use the orthogonality property of trigonometric functions:

$$\begin{aligned} -m\sum_l a_{m,l}\frac{\widetilde{z}^l}{l!} &= \frac{R_0}{F_0\pi}\int_0^{2\pi} B_{E,\phi}|_{\widetilde{R}=1}\sin m\phi\; d\phi, \\ m\sum_l b_{m,l}\frac{\widetilde{z}^l}{l!} &= \frac{R_0}{F_0\pi}\int_0^{2\pi} B_{E,\phi}|_{\widetilde{R}=1}\cos m\phi\; d\phi. \end{aligned} \tag{4.9}$$

The number of terms L in the summations over l in equations (4.9) that is necessary to accurately represent the magnetic field is usually less than the number of poloidal modes used in the GVEC equilibrium. In practice, it is best to scan through different values of L, starting with the number of poloidal modes and decreasing from there, while trying to minimize the error in $\nabla\chi$ as compared to $\vec{B}_E$. Note that using higher values of L than necessary can lead to higher errors away from the $\widetilde{R} = 1$ surface due to overfitting, as the integration in equations (4.11), (4.12), (4.15) and (4.16), which will be derived shortly, is only over the $\widetilde{R} = 1$ surface. Figure 4.1 shows the volume-averaged relative squared error of the Dommaschk potential representation as a function of the number L of poloidal modes kept in a Wendelstein 7-A equilibrium with $\beta = 2.3 \cdot 10^{-3}$ % (see section 4.3 for more details about this equilibrium).

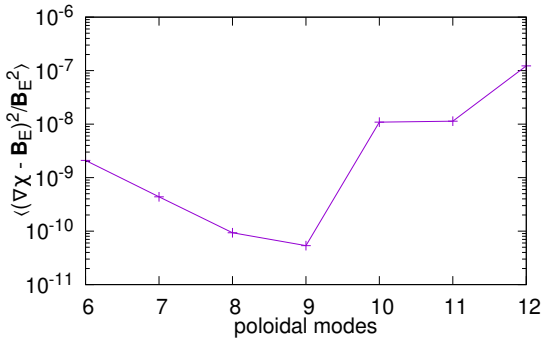

Figure 4.1: The volume-averaged squared relative error of the Dommaschk potential representation $\langle(\nabla\chi - \vec{B}_E)^2/B_E^2\rangle$ as a function of the number of poloidal modes L. The values shown in this plot were calculated using a Python implementation of Dommaschk potentials based on the one written by Paul Huslage for the BOUT++ code [39, 40].

One can convert equations (4.9) into two linear algebraic systems with triangular matrices by changing the variable to $z' = \widetilde{z}/Z$ and, after multiplying both equations by a Legendre polynomial $P_n(z')$, integrating from -1 to 1. Here, Z is determined as follows. In each poloidal plane at $\widetilde{R} = 1$, $\widetilde{z} \in [-\widetilde{z}_-(\phi), \widetilde{z}_+(\phi)]$, so $Z < \min_\phi\{\widetilde{z}_-(\phi), \widetilde{z}_+(\phi)\}$. The value of Z is chosen to be slightly smaller than the minimum to avoid using the components of $\vec{B}_E$ close to the boundary, where the output of EXTENDER_P can be less accurate. There is some freedom in choosing the specific value of Z, and it may take some trial and error to find the best value. The Legendre polynomials are orthogonal to monomials of lower order than the polynomial; this can be seen by expanding a monomial z^l in the Legendre polynomial basis:

$$z^l = \sum_n C_{l,n} P_n(z). \tag{4.10}$$

Clearly, the summation must terminate at $n = l$ since each new polynomial $P_n(z)$ contains a term of order n, which cannot be cancelled by any of the terms in the lower order polynomials. Thus, if $P_{l+1}(z)$ is included in the series, there would be a z^{l+1} term that does not get cancelled, a contradiction. Including $P_{l+2}(z)$ would cancel the z^{l+1} term, but would also introduce an uncancellable z^{l+2} term, and so on.

Using the orthogonality property discussed above, one has, starting with $n = L$ and descending to $n = 0$, the following linear algebraic system for $a_{m,l}$:

$$\begin{aligned}
-m\frac{a_{m,L}}{L!}Z^L\langle z^L, P_L(z)\rangle &= \frac{R_0}{F_0\pi}\int_0^{2\pi}\int_{-1}^{1} B_{E,\phi}|_{\widetilde{R}=1,\widetilde{z}=Zz'}\, P_L(z')\sin m\phi\; dz'\; d\phi,\\
-m\frac{a_{m,L}}{L!}Z^L\langle z^L, P_{L-1}(z)\rangle - m\frac{a_{m,L-1}}{(L-1)!}Z^{L-1}\langle z^{L-1}, P_{L-1}(z)\rangle &\\
= \frac{R_0}{F_0\pi}\int_0^{2\pi}\int_{-1}^{1} B_{E,\phi}|_{\widetilde{R}=1,\widetilde{z}=Zz'}\, P_{L-1}(z')\sin m\phi\; dz'\; d\phi,&\\
\vdots&\\
-m\sum_{n=0}^{L}\frac{a_{m,n}}{n!}Z^n\langle z^n, P_0(z)\rangle = \frac{R_0}{F_0\pi}\int_0^{2\pi}\int_{-1}^{1} B_{E,\phi}|_{\widetilde{R}=1,\widetilde{z}=Zz'}\, P_0(z')\sin m\phi\; dz'\; d\phi,&
\end{aligned} \tag{4.11}$$

where $\langle z^i, P_j(z)\rangle = \int_{-1}^{1} z^i P_j(z)dz$. Similarly, for the coefficients $b_{m,l}$, one has the following linear algebraic system:

$$\begin{aligned}
m\frac{b_{m,L}}{L!}Z^L\langle z^L, P_L(z)\rangle &= \frac{R_0}{F_0\pi}\int_0^{2\pi}\int_{-1}^{1} B_{E,\phi}|_{\widetilde{R}=1,\widetilde{z}=Zz'}\, P_L(z')\cos m\phi\; dz'\; d\phi,\\
m\frac{b_{m,L}}{L!}Z^L\langle z^L, P_{L-1}(z)\rangle + m\frac{b_{m,L-1}}{(L-1)!}Z^{L-1}\langle z^{L-1}, P_{L-1}(z)\rangle &\\
= \frac{R_0}{F_0\pi}\int_0^{2\pi}\int_{-1}^{1} B_{E,\phi}|_{\widetilde{R}=1,\widetilde{z}=Zz'}\, P_{L-1}(z')\cos m\phi\; dz'\; d\phi,&\\
\vdots&\\
m\sum_{n=0}^{L}\frac{b_{m,n}}{n!}Z^n\langle z^n, P_0(z)\rangle = \frac{R_0}{F_0\pi}\int_0^{2\pi}\int_{-1}^{1} B_{E,\phi}|_{\widetilde{R}=1,\widetilde{z}=Zz'}\, P_0(z')\cos m\phi\; dz'\; d\phi.&
\end{aligned} \tag{4.12}$$

As can be seen, both of these systems of equations have triangular matrices.

At this point, the equations for the coefficients $c_{m,l}$ and $d_{m,l}$ have yet to be determined. Consider now the R component of $\vec{B}_E$: $B_{E,R} = \widehat{R}\cdot\vec{B}_E = \partial\chi/\partial R$. One has:

$$\begin{aligned}
\frac{R_0}{F_0}B_{E,R} = \frac{\partial\widetilde{\chi}}{\partial\widetilde{R}} = \sum_{m,l}\Bigg[&(a_{m,l}\cos m\phi + b_{m,l}\sin m\phi)\frac{\partial D_{m,l}}{\partial\widetilde{R}}\\
&+ (c_{m,l}\cos m\phi + d_{m,l}\sin m\phi)\frac{\partial N_{m,l-1}}{\partial\widetilde{R}}\Bigg].
\end{aligned} \tag{4.13}$$

Again, evaluating at $\widetilde{R}=1$ and using the properties of the $D_{m,n}$ and $N_{m,n}$ functions given by equations (10) and (11) of Ref [37], one has:

$$\left.\frac{R_0}{F_0}B_{E,R}\right|_{\widetilde{R}=1}=\sum_{m,l}(c_{m,l}\cos m\phi+d_{m,l}\sin m\phi)\frac{\widetilde{z}^{l-1}}{(l-1)!}. \tag{4.14}$$

From here, it is straightforward to follow the same steps as for $a_{m,l}$ and $b_{m,l}$, obtaining the following linear algebraic systems for $c_{m,l}$:

$$\begin{aligned}
&\frac{c_{m,L}}{(L-1)!}Z^{L-1}\langle z^{L-1},P_{L-1}(z)\rangle=\frac{R_0}{F_0\pi}\int_0^{2\pi}\int_{-1}^{1}B_{E,R}|_{\widetilde{R}=1,\widetilde{z}=Zz'}\,P_{L-1}(z')\cos m\phi\;dz'\;d\phi,\\
&\frac{c_{m,L}}{(L-1)!}Z^{L-1}\langle z^{L-1},P_{L-2}(z)\rangle+\frac{c_{m,L-1}}{(L-2)!}Z^{L-2}\langle z^{L-2},P_{L-2}(z)\rangle\\
&\qquad\qquad=\frac{R_0}{F_0\pi}\int_0^{2\pi}\int_{-1}^{1}B_{E,R}|_{\widetilde{R}=1,\widetilde{z}=Zz'}\,P_{L-2}(z')\cos m\phi\;dz'\;d\phi,\\
&\qquad\qquad\vdots\\
&\sum_{n=0}^{L-1}\frac{c_{m,n+1}}{n!}Z^{n}\langle z^{n},P_0(z)\rangle=\frac{R_0}{F_0\pi}\int_0^{2\pi}\int_{-1}^{1}B_{E,R}|_{\widetilde{R}=1,\widetilde{z}=Zz'}\,P_0(z')\cos m\phi\;dz'\;d\phi,
\end{aligned} \tag{4.15}$$

and for $d_{m,l}$:

$$\begin{aligned}
&\frac{d_{m,L}}{(L-1)!}Z^{L-1}\langle z^{L-1},P_{L-1}(z)\rangle=\frac{R_0}{F_0\pi}\int_0^{2\pi}\int_{-1}^{1}B_{E,R}|_{\widetilde{R}=1,\widetilde{z}=Zz'}\,P_{L-1}(z')\sin m\phi\;dz'\;d\phi,\\
&\frac{d_{m,L}}{(L-1)!}Z^{L-1}\langle z^{L-1},P_{L-2}(z)\rangle+\frac{d_{m,L-2}}{(L-2)!}Z^{L-2}\langle z^{L-2},P_{L-2}(z)\rangle\\
&\qquad\qquad=\frac{R_0}{F_0\pi}\int_0^{2\pi}\int_{-1}^{1}B_{E,R}|_{\widetilde{R}=1,\widetilde{z}=Zz'}\,P_{L-2}(z')\sin m\phi\;dz'\;d\phi,\\
&\qquad\qquad\vdots\\
&\sum_{n=0}^{L-1}\frac{d_{m,n+1}}{n!}Z^{n}\langle z^{n},P_0(z)\rangle=\frac{R_0}{F_0\pi}\int_0^{2\pi}\int_{-1}^{1}B_{E,R}|_{\widetilde{R}=1,\widetilde{z}=Zz'}\,P_0(z')\sin m\phi\;dz'\;d\phi.
\end{aligned} \tag{4.16}$$

Note that there are only L equations in each system for the unknowns $c_{m,1},\ldots,c_{m,L}$ and $d_{m,1},\ldots,d_{m,L}$ because $N_{m,-1}$ is not defined, and so terms with $c_{m,0}$ and $d_{m,0}$ are not included in the sum (4.2).

The only coefficients for which a system of equations has not yet been obtained are $a_{0,l}$ (there are no $b_{0,l}$ coefficients since $\sin 0=0$). These coefficients cannot be

obtained from the system (4.11) since the matrices of this system are singular when $m = 0$. To get a solvable system, one must use the z component of $\vec{B}_E$:

$$\begin{aligned}\frac{R_0}{F_0}B_{E,z} = \frac{\partial\widetilde{\chi}}{\partial\widetilde{z}} = \sum_{m,l}\Bigg[&(a_{m,l}\cos m\phi + b_{m,l}\sin m\phi)\frac{\partial D_{m,l}}{\partial\widetilde{z}} \\ &+ (c_{m,l}\cos m\phi + d_{m,l}\sin m\phi)\frac{\partial N_{m,l-1}}{\partial\widetilde{z}}\Bigg].\end{aligned} \tag{4.17}$$

Evaluating at $\widetilde{R} = 1$ using the properties of the functions $D_{m,n}$ and $N_{m,n}$ gives:

$$\frac{R_0}{F_0}B_{E,z}\bigg|_{\widetilde{R}=1} = \sum_{m,l}(a_{m,l}\cos m\phi + b_{m,l}\sin m\phi)\frac{\widetilde{z}^{l-1}}{(l-1)!} \tag{4.18}$$

Integrating over ϕ leaves only the $m = 0$ term in the sum, as all others are harmonic:

$$\sum_l a_{0,l}\frac{\widetilde{z}^{l-1}}{(l-1)!} = \frac{R_0}{2F_0\pi}\int_0^{2\pi} B_{E,z}|_{\widetilde{R}=1}\,d\phi. \tag{4.19}$$

To finalize the derivation, multiply the equation by a Legendre polynomial $P_n(z')$ and integrate from -1 to 1. Starting from $n = L-1$ and descending to $n = 0$, the system of equations is

$$\begin{aligned}
&\frac{a_{0,L}}{(L-1)!}Z^{L-1}\langle z^{L-1}, P_{L-1}(z)\rangle = \frac{R_0}{2F_0\pi}\int_0^{2\pi}\int_{-1}^{1} B_{E,z}|_{\widetilde{R}=1,z=Zz'}\,P_{L-1}(z')dz'd\phi, \\
&\frac{a_{0,L}}{(L-1)!}Z^{L-1}\langle z^{L-1}, P_{L-2}(z)\rangle + \frac{a_{0,L-1}}{(L-2)!}Z^{L-2}\langle z^{L-2}, P_{L-2}(z)\rangle \\
&\qquad\qquad = \frac{R_0}{2F_0\pi}\int_0^{2\pi}\int_{-1}^{1} B_{E,z}|_{\widetilde{R}=1,z=Zz'}\,P_{L-2}(z')dz'd\phi, \\
&\qquad\qquad\qquad\vdots \\
&\sum_{n=0}^{L-1}\frac{a_{0,n+1}}{n!}Z^n\langle z^n, P_0(z)\rangle = \frac{R_0}{2F_0\pi}\int_0^{2\pi}\int_{-1}^{1} B_{E,z}|_{\widetilde{R}=1,z=Zz'}\,P_0(z')dz'd\phi.
\end{aligned} \tag{4.20}$$

Just as in the case of systems (4.15) and (4.16), there are only L equations for the unknowns $a_{0,1}, \ldots, a_{0,L}$. This is because $D_{0,0} = 1$, and so $a_{0,0}$ is an additive constant in the scalar potential, which has no effect on the vacuum magnetic field [37].

The linear algebraic systems of equations (4.11), (4.12), (4.15), (4.16) and (4.17) are solved in a Python script developed as a part of this thesis project, using the NumPy library [41]. The solution was then written out to a Fortran namelist file,

which can then be read by JOREK.

4.2 Determining initial conditions from the GVEC solution

As was mentioned in the previous chapter, although $\widetilde{j}$ and Ψ are related by $\widetilde{j} = \Delta^*\Psi$, where $\Delta^* = B_v^{-2}\nabla\cdot(B_v^2\nabla^\perp$, $\widetilde{j}$ is stored as a separate variable for numerical purposes. This ensures that $\widetilde{j}$ is G^1 continuous, as it is projected to the finite element basis by the definition equation. It makes sense to first calculate the initial condition for $\widetilde{j}$, $\widetilde{j}_0$ from the GVEC data, and then calculate Ψ_0 from $\widetilde{j}_0$ using

$$\Delta^*\Psi_0 = \widetilde{j}_0. \tag{4.21}$$

The equilibrium magnetic field provided by the GVEC solution will be referred to as $\vec{B}_{GVEC}$. Since GVEC works with full MHD, one needs to consider the full MHD ansatz when working with $\vec{B}_{GVEC}$:

$$\vec{B}_{GVEC} = \nabla\chi + \nabla\Psi_0\times\nabla\chi + \nabla\Omega_0\times\nabla\psi_v.$$

Taking the curl of the above equation and dotting it with $\nabla\chi$, one has, after some algebra:

$$j^\chi_{GVEC} = \nabla\chi\cdot\nabla\times\vec{B}_{GVEC} = -\nabla\cdot(B_v^2\nabla^\perp\Psi_0) + \nabla\cdot(B_v\partial^\parallel\Omega_0\nabla\psi_v).$$

Using the same ordering as when discussing force balance in section 2.7.2, where $B_v = O(1)$, $\Psi = O(\lambda)$, $\Omega = O(\lambda^2)$ and $\partial^\parallel = O(\lambda)$, with λ being the ordering parameter, it can be seen that the first term is $O(\lambda)$ and second term is $O(\lambda^3)$. Thus, the second term can be neglected, due to being two orders higher than the first term. This significantly simplifies the calculation, as now one can just set $\widetilde{j}_0 = -j^\chi_{GVEC}/B_v^2 = -\nabla\chi\cdot\nabla\times\vec{B}_{GVEC}/B_v^2$.

Having determined $\widetilde{j}_0$, it remains to solve the differential equation (4.21) for Ψ_0. First, however, one needs to determine the boundary condition on Ψ. When running a fixed boundary simulation, as done in this dissertation, it is usually assumed that the plasma is surrounded by a perfect conductor, so the magnetic field at the boundary does not have a normal component: $\vec{n}\cdot\vec{B} = 0$. In the reduced MHD model, this means that Ψ has to satisfy $\vec{n}\cdot(\nabla\Psi\times\nabla\chi) = -\vec{n}\cdot\nabla\chi$ at all times.

This is a nonhomogeneous linear differential equation which must be solved on the boundary of the torus; the solution to this differential equation then provides a nonhomogeneous Dirichlet boundary condition for equation (4.21). Note that the kernel of the differential operator in the boundary equation is quite large, consisting of all functions $f(\chi)$. Using a flux surface aligned coordinate system (ψ, θ, ϕ), where ψ is a flux surface label, θ is a poloidal angle and ϕ is a toroidal angle, the boundary equation becomes:

$$\frac{\partial \Psi}{\partial \theta}\frac{\partial \chi}{\partial \phi} - \frac{\partial \Psi}{\partial \phi}\frac{\partial \chi}{\partial \theta} = -J\nabla\psi \cdot \nabla\chi, \tag{4.22}$$

where $J = [\nabla\psi \cdot (\nabla\theta \times \nabla\phi)]^{-1}$ is the Jacobian. However, solving the equation in this form is numerically difficult because one cannot easily separate the kernel and remove it from the solution space. To do so, one must switch to a coordinate system where χ is one of the coordinates. It is best to switch out ϕ for χ, since a stellarator must have a nonvanishing toroidal component to its vacuum field (c.f. the $F_0\phi$ term in equation (4.1)), so $\partial\chi/\partial\phi$ is nonvanishing and the Jacobian of the new coordinates is nowhere singular. The boundary equation in (ψ, θ, χ) coordinates is

$$\frac{\partial \Psi}{\partial \theta} = -J'\nabla\psi \cdot \nabla\chi, \tag{4.23}$$

where $J' = [\nabla\psi \cdot (\nabla\theta \times \nabla\chi)]^{-1}$ is the new Jacobian. It is easy to solve this equation in JOREK. Due to the JOREK grid being flux surface aligned, the element local coordinates s and t (see section 1.4) can be related to the coordinates ψ and θ as $\psi = s$, $\theta = 2\pi(t + i_{\text{bnd\_elm}})/N_{\text{bnd\_elm}}$, where $i_{\text{bnd\_elm}}$ is the zero-based index of the current boundary element and $N_{\text{bnd\_elm}}$ is the total number of boundary elements. Finally, the χ coordinate is given by the Dommaschk representation (4.2). The solution space in which the solution to equation (4.23) is searched for can now be represented as:

$$\mathcal{V}_{sol} = \text{span}[\{\cos m\theta, \sin m\theta | m = 1, ..., m_{\text{pol}}\} \times \{1, \cos n\chi, \sin n\chi | n = 1, ..., n_{\text{tor}}\}]. \tag{4.24}$$

Excluding the $m = 0$ mode removes the kernel of the differential operator of equa-

tion (4.23) from $\mathcal{V}_{sol}$, and the equation can then be solved using the standard Fourier-Galerkin method. The solution obtained this way is then projected back onto the JOREK finite element basis and written to the boundary nodes. Finally, equation (4.21) is solved by splitting $\Psi_0 = \Psi_{0,i} + \Psi_b$, where Ψ_b is the solution to equation (4.23) and thus satisfies the nonhomogeneous Dirichlet boundary condition, while $\Psi_{0,i}$ is an unknown function which is zero at the boundary. The solution $\Psi_{0,i}$ is then found using the standard JOREK solver with homogeneous Dirichlet boundary conditions. When Ψ is evolved in time, the increments $\delta\Psi$ (see equation (1.32)) must also be zero at the boundary, so that the nonhomogeneous boundary condition continues to be satisfied.

The last step is determining an initial condition for temperature, which is almost trivial. The GVEC solution provides a pressure profile p_{GVEC}, which must simply be converted to JOREK units and divided by the initial density profile ρ_0. In all of the stellarator simulations presented in this chapter, the initial density is taken to be constant for simplicity, which corresponds to $\rho_0 = 1$ in JOREK units.

4.3 A consistency check for the stellarator model

After having derived and implemented the stellarator model, it remains to validate it for stellarators, showing that it does work. However, before proceeding to more complicated cases, a set of initial tests must be done using stable equilibria to demonstrate that the model is indeed consistent, the error due to neglecting of fourth-order terms in the force balance, which was discussed in section 2.7.2, is small, and no significant change is observed in the stable cases after simulating them for some time.

The consistency checks were done using four equilibria based on the historic Wendelstein 7-A stellarator [35] with different values of β. These equilibria were intended to be unstable to the (2,1) tearing mode, however, since Wendelstein 7-A had five field periods, the simulations can be done with five-fold periodicity,

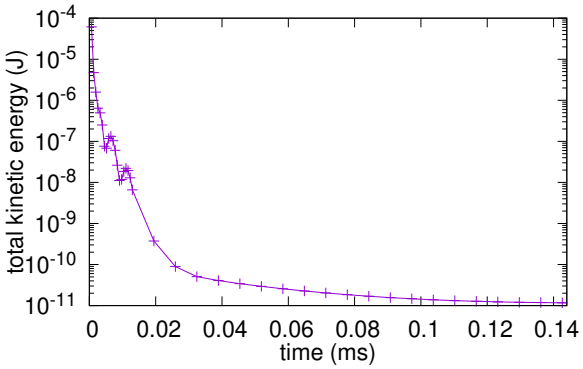

Figure 4.2: The total kinetic energy of the plasma in the $\beta = 0.022$ % case during the first 0.144 ms of the simulation (20 time steps of 1 and 20 time steps of 10 JOREK time units) showing the damping out of motion due to the neglect of fourth order terms in the force balance.

excluding the unstable $n = 1$ Fourier mode and its mode family. The equilibria were first calculated with VMEC/NEMEC [42], and then GVEC was used to refine them. Poloidal modes $m = 0, ..., 12$ and toroidal modes $n = 0, ..., 10$, which corresponds to $N_{\text{ctor}} = 21$ in JOREK, were used to calculate the equilibrium. Note that the toroidal modes are within one period; for the full torus, they correspond to $n = 0, 5, 10, ..., 50$. All of the equilibria have the same boundary: a rotating ellipse with a minor axis of 0.091 m and a major axis of 0.12 m; the major radius of the torus is 1.99 m. The normalized toroidal current profile was also the same for all equilibria:

$$I_n(\psi_{tn}) = 3\psi_{tn} - 3\psi_{tn}^2 + \psi_{tn}^3, \tag{4.25}$$

where ψ_{tn} is the toroidal flux normalized so that $\psi_{tn} = 0$ at the axis and $\psi_{tn} = 1$ at the boundary. $I_n(\psi_{tn})$, which represents the toroidal current enclosed by the flux surface ψ_{tn} is normalized by the total toroidal current, which was 17.5 kA in the cases considered, such that $I_n(1) = 1$. The pressures at the axis were 1 Pa, 100 Pa, 500 Pa and 1 kPa, which corresponds to β-values of $2.3 \cdot 10^{-5}$ %, $2.3 \cdot 10^{-3}$ %, 0.011 % and 0.022 %, respectively. The pressure profiles are given by

$$p(\psi_{tn}) = p_a - (p_a - p_b)\psi_{tn}, \tag{4.26}$$

where p is the pressure in pascals, p_a is the pressure at the axis and p_b is the pressure at the boundary. For the $\beta = 2.3 \cdot 10^{-5}$ % ($p_a = 1$ Pa) case, $p_b = 0.01$ Pa,

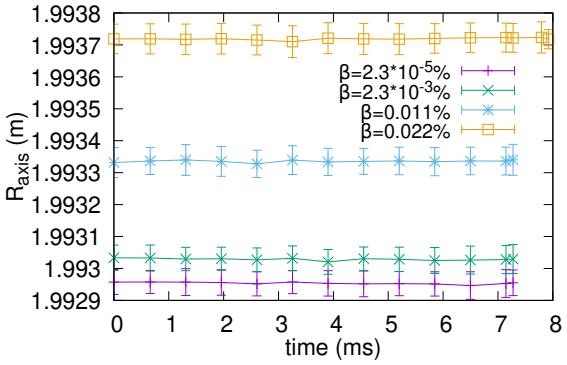

Figure 4.3: The R coordinate of the magnetic axis as a function of time for the four different β cases.

while for the other three cases, $p_b = 1$ Pa. When finding the initial conditions from the GVEC equilibrium, $N_{tor} = 9$ was used for the variables, which corresponds to Fourier modes $n = 0, ..., 4$ within one period, or $n = 0, 5, ..., 20$ within the full torus.

All of the simulations were run with a spatially constant resistivity $\eta = 1.938 \cdot 10^{-9}$ Ω·m and viscosity $\mu = 2.90 \cdot 10^{-9}$ kg/(m · s). In addition, a hyperviscosity of $2.90 \cdot 10^{-12}$ kg · m/s was also used. The radial resolution of the finite elements was 41, and the poloidal resolution was 48. The first part of the simulation was run using the implicit Euler time stepping scheme to damp out the small oscillations that were present due to the neglect of fourth order terms in the force balance (see Figure 4.2). This consisted of 20 time steps of length $6.484 \cdot 10^{-4}$ ms (1 in JOREK units), followed by 20 time steps of length $6.484 \cdot 10^{-3}$ ms (10 in JOREK units), followed by 10 time steps of length $6.484 \cdot 10^{-2}$ ms (100 in JOREK units). For the $\beta = 0.022\%$ case, but not for the others, this was followed by another 10 time steps of length $6.484 \cdot 10^{-2}$ ms. In the second part of the simulation, the Crank-Nicolson time stepping scheme was used, and all four cases were simulated for 6.484 ms (10000 in JOREK units). The $\beta = 2.3 \cdot 10^{-5}$ % and $\beta = 2.3 \cdot 10^{-3}$ % cases used time steps of length $6.484 \cdot 10^{-2}$ ms in the second part, however the $\beta = 0.011$ % and $\beta = 0.022$ % required shorter time steps ($3.242 \cdot 10^{-2}$ ms and $1.621 \cdot 10^{-2}$ ms, respectively) for numerical stability. The toroidal integration was done by summing over 40 poloidal planes spread evenly over one period.

As expected, no large scale motion was observed in any of the four simulations. This can be seen in Figure 4.3, where the R coordinate of the magnetic axis is plotted as a function of time for each of the four cases, along with the error bars. The axis was determined by making an initial guess for its (R, z) position in the $\phi = 0$ poloidal plane, and then tracing the field line at that position for ten toroidal turns, after which the error $E = 0.1\sqrt{(\max R_i - \min R_i)(\max z_i - \min z_i)}$, where $i = 1, ..., 10$, is calculated. If this error is smaller than the tolerance, which was set to $5 \cdot 10^{-5}$ m, then the axis is considered found: the axis position at $\phi = 0$ is $(R_c, z_c) = ((\max R_i + \min R_i)/2, (\max z_i + \min z_i)/2)$. If not, then the field line tracing is restarted at (R_c, z_c), and the process is repeated until the error is less than the tolerance.

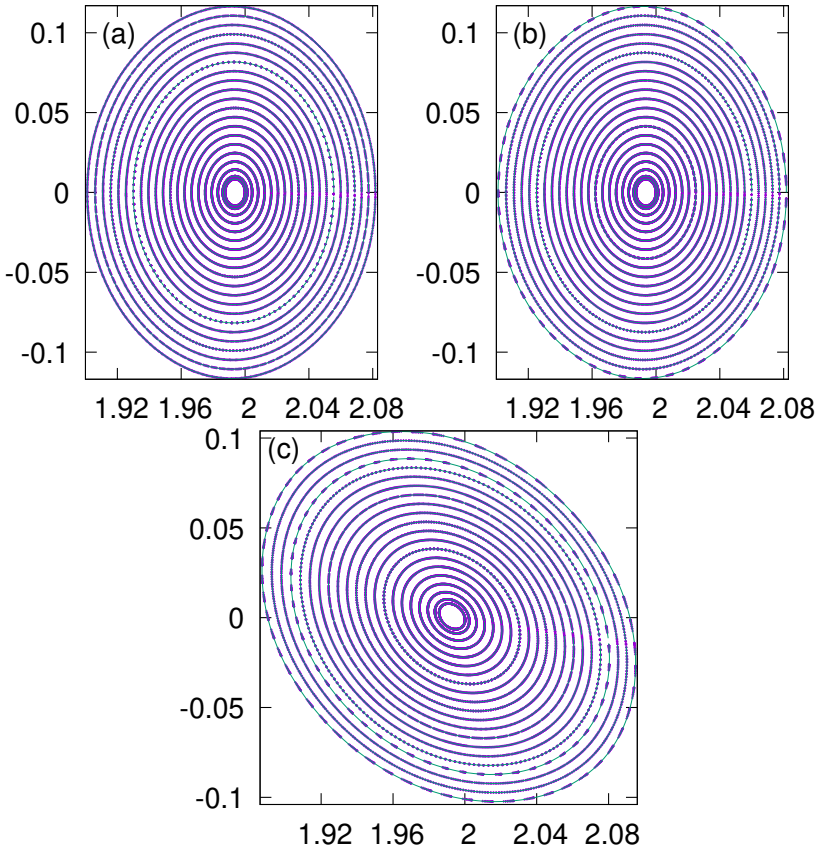

Figure 4.4: The Poincare plots for the $\beta = 0.022$ % case at $t = 0$ and $\phi = 0$ (a), at $\phi = 0$ after the simulation is over ($t = 7.275$ ms) (b), and at $t = 0$ and $\phi = 3\pi/10$ (3/4 of the way through one period) (c).

To demonstrate that there is no significant motion even away from the axis, the Poincare plots for the $\beta = 0.022$ % case are shown in Figure 4.4, both before and after the simulation, along with the flux surfaces of the GVEC equilibrium. As can be seen, the flux surfaces in JOREK coincide with the GVEC flux surfaces, so the error introduced by using the reduced MHD ansatz for the magnetic field has no noticeable effect on the flux surfaces. Moreover, the flux surfaces do not move during the simulation, preserving the stable equilibrium as expected.

4.4 Tearing modes: benchmarking against CASTOR3D

Having demonstrated that basic stellarator simulations can be run with the correct equilibrium force balance in the newly implemented model in JOREK, the next step is to simulate instabilities and benchmark them against known results. Tearing modes in the Wendelstein 7-A stellarator will be used for this purpose. Three cases at different values of β will be considered: $2.3 \cdot 10^{-5}$ %, $2.3 \cdot 10^{-4}$ % and $2.3 \cdot 10^{-3}$ %. The $\beta = 2.3 \cdot 10^{-5}$ % and $\beta = 2.3 \cdot 10^{-3}$ % are the same equilibria that were used in the previous section, with the $\beta = 2.3 \cdot 10^{-4}$ % being a new equilibrium with the same boundary and current profile as the other two and an intermediate value of β. In this new intermediate equilibrium, $p_a = 10$ Pa and $p_b = 0.1$ Pa. When finding the initial conditions from the GVEC equilibrium, $N_{tor} = 5$ was used for the variables, which corresponds to Fourier modes $n = 0, 1, 2$ in one period, or $n = 0, 5, 10$ in the full torus.

Just as before, the stellarator simulations were run with the implicit Euler time stepping scheme and five-fold periodicity to damp out oscillations. This consisted of 20 time steps of length $6.484 \cdot 10^{-4}$ ms, followed by 20 time steps of length $6.484 \cdot 10^{-3}$ ms, followed by 5 time steps of length $6.484 \cdot 10^{-2}$ ms. The resistivity was set to $\eta = 1.938 \cdot 10^{-6}$ Ω·m and the viscosity was zero. The hyperviscosity was $2.90 \cdot 10^{-15}$ kg $\cdot$ m/s for the $\beta = 2.3 \cdot 10^{-5}$ % and the $\beta = 2.3 \cdot 10^{-4}$ % cases and $7.25 \cdot 10^{-15}$ kg $\cdot$ m/s for the $\beta = 2.3 \cdot 10^{-3}$ % case. The finite element reso-

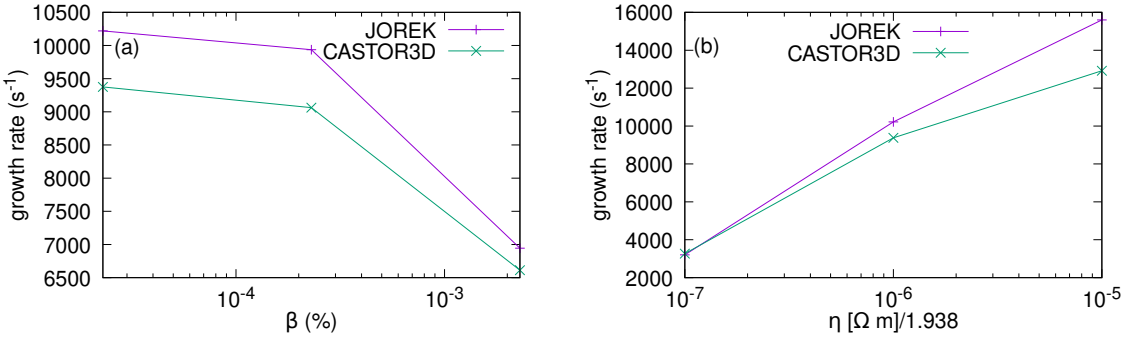

Figure 4.5: The JOREK and CASTOR3D growth rates at $\eta = 1.938 \cdot 10^{-6}$ Ω·m and differing betas (a), and at $\beta = 2.3 \cdot 10^{-5}$ % and differing resistivities (b).

lution was 41 radially and 48 poloidally, just as before. In the second part of the simulation, the domain was extended to the full torus, taking now into account the $n = 0, ..., 10$ Fourier modes, corresponding to $N_{tor} = 21$. The Crank-Nicolson scheme was used with time steps of length $1.621 \cdot 10^{-2}$ ms. The volume integration was done by summing over 40 poloidal planes spread evenly throughout the full torus. The number of Fourier modes, number of poloidal planes and the values of hyperviscosity, resolution and time step size were chosen after scanning over several values for each parameter and choosing the value at which the growth rate of the tearing mode converged. For the present purposes, convergence is considered to be achieved when halving the time step size or hyperviscosity, or doubling the resolution, number of modes or number of planes leads to a change in the growth rate of less than 1.5%. The convergence test was done for the $\beta = 2.3 \cdot 10^{-3}$ % and $\beta = 2.3 \cdot 10^{-5}$ % cases, resulting in all of the parameters converging to the same values, except for hyperviscosity, which converged to $7.25 \cdot 10^{-15}$ kg · m/s for the $\beta = 2.3 \cdot 10^{-3}$ % case and $2.90 \cdot 10^{-15}$ kg · m/s for the $\beta = 2.3 \cdot 10^{-5}$ % case. The $\beta = 2.3 \cdot 10^{-4}$ % case was then run using the lower value of hyperviscosity. Figure 4.5 a shows the values of the growth rates from JOREK alongside the values calculated in a linear MHD code called CASTOR3D [43, 44] by R. Ramasamy. The maximum error is 9.6%, and occurs at $\beta = 2.3 \cdot 10^{-4}$ %.

Two more simulations were done with the $\beta = 2.3 \cdot 10^{-5}$ % case, this time

using resistivities of $\eta = 1.938 \cdot 10^{-7}$ Ω·m and $\eta = 1.938 \cdot 10^{-5}$ Ω·m, while all of the other parameters were kept the same as before. For the $\eta = 1.938 \cdot 10^{-7}$ Ω·m case, a hyperresistivity of $9.691 \cdot 10^{-14}$ Ω·m^2 ($5 \cdot 10^{-14}$ in JOREK units) had to be introduced in order for the iterative solver to converge in a reasonable amount of time. However, it was first confirmed that introducing this amount of hyperresistivity in the $\eta = 1.938 \cdot 10^{-6}$ Ω·m case, which could be run with or without hyperresistivity, changes the growth rate by less than 1.5%. Figure 4.5 b shows the growth rates for the $\beta = 2.3 \cdot 10^{-5}$ % case at different values of resistivity alongside the growth rates calculated by CASTOR3D. The maximum error is 20.7%, occuring at $\eta = 1.938 \cdot 10^{-5}$ Ω·m. This is most likely due to the neglect of $v_{\parallel}$ by the model used in these simulations, as $v_{\parallel}$ can be large within the resistive layer, and the size of the resistive layer increases with resistivity. In general, the agreement on the growth rates for the (2,1) tearing mode looks convincing, with deviations on the order of 10% from CASTOR3D, which is a full MHD linear code.

4.5 Preliminary studies of ballooning modes

Further work will involve doing a similar benchmark with CASTOR3D for ballooning mode growth rates in Wendelstein 7-A. Some preliminary studies using equilibria with $\beta = 0.11\%$ and $\beta = 0.21\%$ (corresponding to axis pressures of 5 kPa and 10 kPa) have already been done at resistivities of $\eta = 1.938 \cdot 10^{-7}$ Ω·m and $\eta = 5.814 \cdot 10^{-7}$ Ω·m. These equilibria have the same toroidal current and pressure profiles as the equilibria in section 4.3, with p_b set to 1 Pa and 100 Pa, respectively. As before, the simulations were initially run with the implicit Euler scheme to damp out oscillations. For all cases except the $\beta = 0.21\%$, $\eta = 5.814 \cdot 10^{-7}$ Ω·m case, this first phase of the simulation consisted of 20 time steps of length $6.484 \cdot 10^{-4}$ ms, followed by 1 time step of length $6.484 \cdot 10^{-3}$ ms. For the $\beta = 0.21\%$, $\eta = 5.814 \cdot 10^{-7}$ Ω·m case, the first phase consisted simply of 30 time steps of length $6.484 \cdot 10^{-4}$ ms. Due to high computational expense, the toroidal

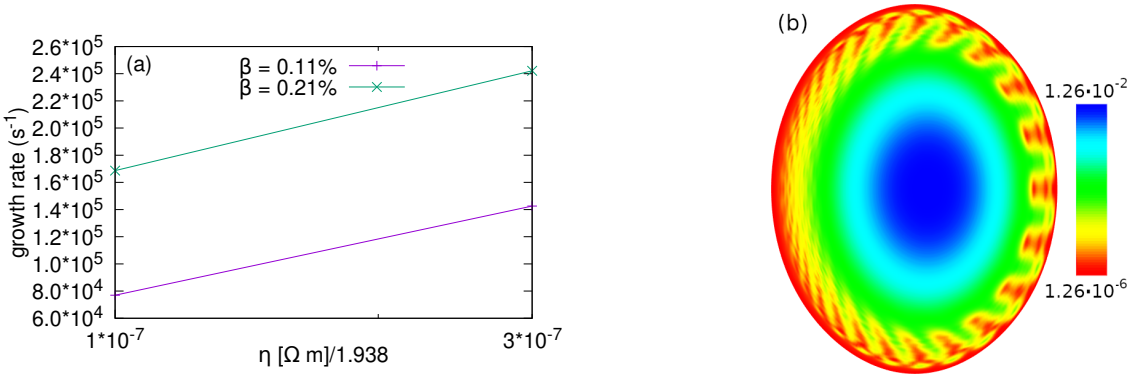

Figure 4.6: The ballooning mode growth rates at two different values of β and resistivity (a), and the temperature plot (JOREK units) in the $\beta = 0.21\%$, $\eta = 1.938 \cdot 10^{-7}$ Ω·m case at $t = 0.081$ ms on the $\phi = 0$ poloidal plane (b).

resolution of these preliminary simulations was limited to only five Fourier modes ($n = 0, ..., 2$). In the second part of the simulation, the Crank-Nicolson scheme was used, however both parts were run with a five-fold periodicity, since ballooning modes can be simulated with just one period. Holding the number of Fourier modes fixed at $N_{\text{tor}} = 5$, a convergence test was done for the $\beta = 0.21\%$ equilibrium while using a resistivity of $\eta = 1.938 \cdot 10^{-7}$ Ω·m. The growth rate converged at a finite element resolution of 61 radially and 72 poloidally, time step size of $6.484 \cdot 10^{-4}$ ms and a hyperviscosity of $7.25 \cdot 10^{-15}$ kg · m/s. The other three simulations were then run with these parameters. Figure 4.6 a shows the growth rates measured in the four cases, and 4.6 b shows the temperature in the $\beta = 0.21\%$, $\eta = 1.938 \cdot 10^{-7}$ Ω·m case on the $\phi = 0$ poloidal plane around the onset of saturation.

5 Conclusions and Future Work

The purpose of this work was to extend the JOREK nonlinear MHD code to stellarators. This requires first to generalize the reduced MHD model to be compatible with three-dimensional geometries. Such a model was derived and studied analytically in chapter 2 this dissertation. The model eliminates fast magnetosonic waves from the system, as a reduced MHD model should, and also guarantees that $\nabla \cdot \vec{B} = 0$, unlike several older reduced MHD models for stellarators. It was shown in section 2.6 that the model conserves energy, but introduces an error into momentum conservation. An alternate model, which does not guarantee energy conservation, but has a smaller momentum conservation error is also derived. It was also shown in section 2.7.2 that the main model introduces an error into equilibrium force balance, but the error is negligible. The energy and momentum conservation properties of the main and alternate models are then studied numerically in the tokamak limit in chapter 3. The momentum conservation error of the main model was shown to be small, and the energy conservation error of the alternate model is generally also small, unless one uses a less numerically stable version of the magnetic stream function evolution equation.

In order to guarantee $\nabla \cdot \vec{B} = 0$ to machine precision, an analytical representation of the vacuum magnetic field (i.e. the curl-free component), as derived by Dommaschk [37], was used. This representation is compatible with arbitrary vacuum fields in a toroidal device. Once implemented, the main model was tested on a set of $l = 2$ stellarator equilibria, based on the classic Wendelstein 7-A stellarator. The GVEC code was used to calculate the equilibria, which were then used as initial conditions for the JOREK runs. As demonstrated in section 4.3 that stable full MHD equilibria are preserved in the reduced model: the flux surfaces do not move

throughout the simulation, and closely match the flux surfaces calculated in GVEC. Further, tearing modes were simulated in section 4.4, and the linear growth rates measured in JOREK are in good agreement with the growth rates calculated by the CASTOR3D linear MHD code.

Future work involves further studies exploring more complicated machines, such as Wendelstein 7-X, and scenarios relevant to ongoing experiments. Of particular interest are the current-driven sawtooth-like crashes observed in Wendelstein 7-X [45]. Previous studies, which included both linear fully three-dimensional simulations with CASTOR3D [46] as well as nonlinear simulations in a simplified cylindrical geometry with the TM1 code [47], have found that the corresponding Wendelstein 7-X equilibria are unstable to single and double tearing modes, as well as resistive kink modes, and that the coupling of double tearing modes with kink modes produces the sawtooth-like crashes. While the family of reduced MHD models used in JOREK, including the models derived in chapter 2, cannot accurately reproduce kink modes at higher β [6], similar sawtooth-like crashes have also been simulated in TM1 at zero β [47]. Using JOREK will allow to simulate these modes nonlinearly in a fully three-dimensional geometry for the first time.

Bibliography

[1] Allen H. Boozer. Curl-free magnetic fields for stellarator optimization. *Physics of Plasmas*, 26(10):102504, 2019. doi:10.1063/1.5116721.

[2] Per Helander. Theory of plasma confinement in non-axisymmetric magnetic fields. *Reports on Progress in Physics*, 77(8):087001, 2014. doi:10.1088/0034-4885/77/8/087001.

[3] Jeffrey P Freidberg. *Ideal MHD*. Cambridge University Press, 2014. doi:10.1017/CBO9780511795046.

[4] GTA Huysmans and O Czarny. MHD stability in X-point geometry: simulation of ELMs. *Nuclear Fusion*, 47(7):659–666, 2007. doi:10.1088/0029-5515/47/7/016.

[5] Olivier Czarny and Guido Huysmans. Bézier surfaces and finite elements for MHD simulations. *Journal of Computational Physics*, 227(16):7423–7445, 2008. doi:10.1016/j.jcp.2008.04.001.

[6] M. Hoelzl, G.T.A. Huijsmans, S.J.P. Pamela, M. Bécoulet, E. Nardon, F.J. Artola, B. Nkonga, C.V. Atanasiu, V. Bandaru, A. Bhole, D. Bonfiglio, A. Cathey, O. Czarny, A. Dvornova, T. Fehér, A. Fil, E. Franck, S. Futatani, M. Gruca, H. Guillard, J.W. Haverkort, I. Holod, D. Hu, S.K. Kim, S.Q. Korving, L. Kos, I. Krebs, L. Kripner, G. Latu, F. Liu, P. Merkel, D. Meshcheriakov, V. Mitterauer, S. Mochalskyy, J.A. Morales, R. Nies, N. Nikulsin, F. Orain, J. Pratt, R. Ramasamy, P. Ramet, C. Reux, K. Särkimäki, N. Schwarz, P. Singh Verma, S.F. Smith, C. Sommariva, E. Strumberger, D.C. van Vugt, M. Verbeek, E. Westerhof, F. Wieschollek, and J. Zielinski. The JOREK non-linear extended MHD code and applications to large-scale instabilities and their control in magnetically confined fusion plasmas. *Nuclear Fusion*, 61(6):065001, 2021. doi:10.1088/1741-4326/abf99f.

[7] J Breslau, N Ferraro, and S Jardin. Some properties of the M3D-C^1 form of the three-dimensional magnetohydrodynamics equations. *Physics of Plasmas*, 16(9):092503, 2009. doi:10.1063/1.3224035.

[8] R Izzo, DA Monticello, J DeLucia, W Park, and CM Ryu. Reduced equations for finite beta tearing modes in tokamaks. *The Physics of fluids*, 28(3):903–911, 1985. doi:10.1063/1.865061.

[9] HR Strauss. Reduced MHD in nearly potential magnetic fields. *Journal of Plasma Physics*, 57(1):83–87, 1997. doi:10.1017/S0022377896005296.

[10] Omar Maj. A mathematical introduction to magnetohydrodynamics. `https://www-m16.ma.tum.de/foswiki/pub/M16/Allgemeines/MHD17/Omar_complete_v4.pdf`, 2017. Lecture notes.

[11] GTA Huysmans, Stanislas Pamela, Emiel Van Der Plas, and Pierre Ramet. Non-linear MHD simulations of edge localized modes (ELMs). *Plasma Physics and Controlled Fusion*, 51(12):124012, 2009. doi:10.1088/0741-3335/51/12/124012.

[12] SJP Pamela, GTA Huijsmans, T Eich, S Saarelma, I Lupelli, CF Maggi, C Giroud, IT Chapman, SF Smith, Lorenzo Frassinetti, Marina Becoulet, Matthias Hoelzl, F Orain, S. Futatani, and JET Contributors. Recent progress in the quantitative validation of JOREK simulations of ELMs in JET. *Nuclear Fusion*, 57(7):076006, 2017. doi:10.1088/1741-4326/aa6e2a.

[13] Emmanuel Franck, Matthias Hölzl, Alexander Lessig, and Eric Sonnendrücker. Energy conservation and numerical stability for the reduced MHD models of the non-linear JOREK code. *ESAIM: Mathematical Modelling and Numerical Analysis*, 49(5):1331–1365, 2015. doi:10.1051/m2an/2015014.

[14] DJ Southwood and MA Saunders. Curvature coupling of slow and Alfvén MHD waves in a magnetotail field configuration. *Planetary and space science*, 33(1):127–134, 1985. doi:10.1016/0032-0633(85)90149-7.

[15] Jeffrey P. Freidberg. *Plasma Physics and Fusion Energy*. Cambridge University Press, 2007. doi:10.1017/CBO9780511755705.

[16] R. Fitzpatrick. *Plasma Physics: An Introduction*. Taylor & Francis, 2014. ISBN 9781466594265.

[17] J. Wesson. *Tokamaks*. Oxford University Press, 2011. ISBN 9780199592234.

[18] SC Jardin, N Ferraro, J Breslau, and J Chen. Multiple timescale calculations of sawteeth and other global macroscopic dynamics of tokamak plasmas. *Computational Science & Discovery*, 5(1):014002, 2012. doi:10.1088/1749-4699/5/1/014002.

[19] Scott E Kruger, Chris C Hegna, and James D Callen. Generalized reduced magnetohydrodynamic equations. *Physics of Plasmas*, 5(12):4169–4182, 1998. doi:10.1063/1.873152.

[20] W Park, DA Monticello, RB White, and SC Jardin. Non-linear saturation of the internal kink mode. *Nuclear fusion*, 20(9):1181–1185, 1980. doi:10.1088/0029-5515/20/9/020.

[21] John M Greene and John L Johnson. Determination of hydromagnetic equilibria. *The Physics of Fluids*, 4(7):875–890, 1961. doi:10.1063/1.1706420.

[22] BB Kadomtsev and OP Pogutse. Nonlinear helical perturbations of a plasma in the tokamak. *Zh. Eksp. Teor. Fiz*, 65(5):575–589, 1973.

[23] HR Strauss. Nonlinear, three-dimensional magnetohydrodynamics of noncircular tokamaks. *The Physics of Fluids*, 19(1):134–140, 1976. doi:10.1063/1.861310.

[24] HR Strauss. Stellarator equations of motion. *Plasma Physics*, 22(7):733–745, 1980. doi:10.1088/0032-1028/22/7/010.

[25] Yao Zhou, N.M. Ferraro, S.C. Jardin, and H.R. Strauss. Approach to nonlinear magnetohydrodynamic simulations in stellarator geometry. *Nuclear Fusion*, 61 (8):086015, 2021. doi:10.1088/1741-4326/ac0b35.

[26] H.R Strauss, L.E Sugiyama, G.Y Fu, W Park, and J Breslau. Simulation of two fluid and energetic particle effects in stellarators. *Nuclear Fusion*, 44(9): 1008–1014, 2004. doi:10.1088/0029-5515/44/9/010.

[27] M. Sato, N. Nakajima, K.Y. Watanabe, and Y. Todo. Characteristics of MHD instabilities for high beta plasmas in inward shifted LHD configurations. *Nuclear Fusion*, 57(12):126023, 2017. doi:10.1088/1741-4326/aa8492.

[28] C. R. Sovinec, C. M. Guilbault, B. S. Cornille, and T. A. Bechtel. Development of MHD simulation capability for stellarators. 62nd Annual Meeting of the APS-DPP, 2020. URL `https://meetings.aps.org/Meeting/DPP20/Session/BO05.9`.

[29] Youcef Saad and Martin H Schultz. Gmres: A generalized minimal residual algorithm for solving nonsymmetric linear systems. *SIAM Journal on scientific and statistical computing*, 7(3):856–869, 1986.

[30] N. Nikulsin, M. Hoelzl, A. Zocco, K. Lackner, and S. Günter. A three-dimensional reduced MHD model consistent with full MHD. *Physics of Plasmas*, 26(10):102109, 2019. doi:10.1063/1.5122013.

[31] Nikita Nikulsin, Matthias Hoelzl, Alessandro Zocco, Karl Lackner, Sibylle Günter, and the JOREK Team. Testing of the new JOREK stellarator-capable model in the tokamak limit. *Journal of Plasma Physics*, 87(3):855870301, 2021. doi:10.1017/S0022377821000477.

[32] William D D'haeseleer, William NG Hitchon, James D Callen, and J Leon Shohet. *Flux coordinates and magnetic field structure: a guide to a fundamental tool of plasma theory*. Springer Science & Business Media, 2012.

[33] John Arthur Hudson. *The excitation and propagation of elastic waves*. CUP Archive, 1980.

[34] D Yu Klimushkin, PN Mager, and Karl-Heinz Glassmeier. Toroidal and poloidal Alfvén waves with arbitrary azimuthal wavenumbers in a finite pressure plasma in the Earth's magnetosphere. *Annales Geophysicae*, 22(1):267–287, 2004.

[35] W VII-A Team. Stabilization of the (2, 1) tearing mode and of the current disruption in the W VII–A stellarator. *Nuclear Fusion*, 20(9):1093–1100, 1980. doi:10.1088/0029-5515/20/9/008.

[36] F. Hindenlang, O. Maj, E. Strumberger, M. Rampp, and E. Sonnendrücker. GVEC: A newly developed 3D ideal MHD Galerkin Variational Equilibrium Code. Presentation given in 'Simons Collaboration on Hidden Symmetries and Fusion Energy', 2019. URL https://hiddensymmetries.princeton.edu/meetings/simons-hour-talks.

[37] W Dommaschk. Representations for vacuum potentials in stellarators. *Computer Physics Communications*, 40(2-3):203–218, 1986. doi:10.1016/0010-4655(86)90109-8.

[38] M Drevlak, D Monticello, and A Reiman. PIES free boundary stellarator equilibria with improved initial conditions. *Nuclear Fusion*, 45(7):731–740, 2005. doi:10.1088/0029-5515/45/7/022.

[39] B.D. Dudson, M.V. Umansky, X.Q. Xu, P.B. Snyder, and H.R. Wilson. BOUT++: A framework for parallel plasma fluid simulations. *Computer Physics Communications*, 180(9):1467–1480, 2009. ISSN 0010-4655. doi:https://doi.org/10.1016/j.cpc.2009.03.008.

[40] B. D. Dudson, J. Madsen, J. Omotani, P. Hill, L. Easy, and M. Løiten. Verification of BOUT++ by the method of manufactured solutions. *Physics of Plasmas*, 23(6):062303, 2016. doi:10.1063/1.4953429.

[41] Charles R. Harris, K. Jarrod Millman, Stéfan J. van der Walt, Ralf Gommers, Pauli Virtanen, David Cournapeau, Eric Wieser, Julian Taylor, Sebastian Berg, Nathaniel J. Smith, Robert Kern, Matti Picus, Stephan Hoyer, Marten H. van Kerkwijk, Matthew Brett, Allan Haldane, Jaime Fernández del Río, Mark Wiebe, Pearu Peterson, Pierre Gérard-Marchant, Kevin Sheppard, Tyler Reddy, Warren Weckesser, Hameer Abbasi, Christoph Gohlke, and Travis E. Oliphant. Array programming with NumPy. *Nature*, 585(7825):357–362, 2020. doi:10.1038/s41586-020-2649-2.

[42] E Strumberger and M Hölzl. User manual: Iterative computation of 3D ideal MHD equilibria and magnetic fields. IPP Report 5/113, 2005. URL http://hdl.handle.net/11858/00-001M-0000-0027-16AA-6.

[43] E. Strumberger and S. Günter. CASTOR3D: linear stability studies for 2D and 3D tokamak equilibria. *Nuclear Fusion*, 57(1):016032, 2016. doi:10.1088/0029-5515/57/1/016032.

[44] E. Strumberger and S. Günter. Linear stability studies for a quasi-axisymmetric stellarator configuration including effects of parallel viscosity, plasma flow, and resistive walls. *Nuclear Fusion*, 59(10):106008, 2019. doi:10.1088/1741-4326/ab314b.

[45] M. Zanini, H.P. Laqua, H. Thomsen, T. Stange, C. Brandt, H. Braune, K.J. Brunner, G. Fuchert, M. Hirsch, J. Knauer, U. Höfel, S. Marsen, E. Pasch, K. Rahbarnia, J. Schilling, Y. Turkin, R.C. Wolf, and A. Zocco and. ECCD-induced sawtooth crashes at W7-X. *Nuclear Fusion*, 60(10):106021, 2020. doi:10.1088/1741-4326/aba72b.

[46] E Strumberger, S Günter, and the Wendelstein 7-X Team. Linear, resistive stability studies for Wendelstein 7-X-type equilibria with external current drive. *Nuclear Fusion*, 60(10):106013, 2020.

[47] Q. Yu, E. Strumberger, V. Igochine, K. Lackner, H.P. Laqua, M. Zanini, H. Braune, M. Hirsch, U. Höfel, S. Marsen, T. Stange, R.C. Wolf, S. Günter, and the Wendelstein 7-X Team. Numerical modeling of the electron temperature crashes observed in Wendelstein 7-X stellarator experiments. *Nuclear Fusion*, 60(7):076024, 2020. doi:10.1088/1741-4326/ab9258.